



DTIC
SELECTED
JAN 03 1995
S B D

ELECTRO-HYDROSTATIC ACTUATOR
CONTROLLER DESIGN USING
QUANTITATIVE FEEDBACK THEORY

THESIS
Ki Ho Kang
Captain, USAF

AFIT/GE/ENG/94D-18

19941228 021

DEPARTMENT OF THE AIR FORCE
AIR UNIVERSITY
AIR FORCE INSTITUTE OF TECHNOLOGY

Wright-Patterson Air Force Base, Ohio

DISTRIBUTION STATEMENT A
Approved for public release
Distribution Unlimited

AFIT/GE/ENG/94D-18

ELECTRO-HYDROSTATIC ACTUATOR
CONTROLLER DESIGN USING
QUANTITATIVE FEEDBACK THEORY

THESIS
Ki Ho Kang
Captain, USAF

AFIT/GE/ENG/94D-18

DTIC QUALITY INSPECTED 2

Approved for public release; distribution unlimited

The views expressed in this thesis are those of the author and do not reflect the official policy or position of the Department of Defense or the U. S. Government.

Accession For	
NTIS GRA&I	<input checked="" type="checkbox"/>
DTIC TAB	<input type="checkbox"/>
Unannounced	<input type="checkbox"/>
Justification	
By	
Distribution/	
Availability Codes	
Dist	Avail and/or Special
1	

AFIT/GE/ENG/94D-18

ELECTRO-HYDROSTATIC ACTUATOR
CONTROLLER DESIGN USING
QUANTITATIVE FEEDBACK THEORY

THESIS

Presented to the Faculty of the School of Engineering
of the Air Force Institute of Technology
Air University
In Partial Fulfillment of the
Requirements for the Degree of
Master of Science (Electrical Engineering)

Ki Ho Kang, B.S.

Captain, USAF

December, 1994

Approved for public release; distribution unlimited

Preface

This design task would have been much more arduous without the QFT CAD package developed by Richard Sating. The compensator packages were designed using his QFT CAD package. His program greatly simplified the design process by reducing the manual computations to a minimum. My design efforts also relied heavily on the Matlab and Matlab Simulink environments. Much of the design preparations and simulations were performed using the Matlab and Matlab Simulink environments. Despite some numerical problems, the Matlab package offers great computational flexibility in solving problems.

I would like to thank my thesis committee for their guidance in my design effort. I would also like to thank Captains Chris Hansen, Steve Rasmussen, and Dennis Trosen of WL/FIG for their support in this research effort.

I would like to thank my parents and friends for the occasional break from the academics. Maybe now I can break the century mark in golf.

Ki Ho Kang

Table of Contents

	Page
Preface	ii
List of Figures	vi
List of Tables	x
Abstract	xi
I. Introduction	1-1
1.1 Background	1-1
1.2 Problem Definition	1-2
1.3 Literature Review	1-2
1.4 Approach	1-3
1.5 Simulation	1-5
1.6 Limitations	1-5
1.7 Overview of Thesis	1-7
II. Models	2-1
2.1 Motor	2-1
2.2 Pump and Fluid	2-1
2.3 Piston and Flight Control Surface	2-3
2.3.1 Piston and Flight Control Surface Fundamentals	2-3
2.3.2 Piston and Flight Control Surface Dynamics	2-3
2.4 Aerodynamic Loads	2-5
2.4.1 Hinge Moment	2-5
2.4.2 Short Period Approximation	2-7

	Page
III. QFT Controller and Prefilter Design	3-1
3.1 Block Model Manipulation	3-1
3.2 Block Model Verification	3-5
3.3 QFT Structure	3-7
3.4 Inner Loop Controller Design	3-7
3.4.1 Inner Loop Specifications	3-7
3.4.2 Set of Plants in the Inner Loop	3-9
3.4.3 Inner Loop Controller and Prefilter Design	3-15
3.4.4 Inner Loop Controller Validations and Simulations	3-16
3.5 Outer Loop Controller Design	3-18
3.5.1 Outer Loop Specifications	3-18
3.5.2 Set of Plants in the Outer Loop	3-19
3.5.3 Outer Loop Controller and Prefilter Design	3-20
3.5.4 Outer Loop Design Validations and Simulations	3-23
IV. Sensitivity Analysis	4-1
4.1 System Sensitivity	4-1
4.2 Time Domain Sensitivity Analysis	4-2
4.3 Frequency Domain Sensitivity Analysis	4-4
4.4 Sensor Noise Effects	4-5
4.4.1 Random Sensor Noise Error	4-10
4.4.2 Sensor Bias Error	4-14
V. Flight Control System Using the EHA model	5-1
5.1 Flight Control System - Pitch Channel	5-1
5.2 Simulations	5-3
5.2.1 Time Domain Simulations	5-3
5.2.2 Frequency Domain Simulations	5-5
5.3 Instability of the Conventional Actuator	5-8

	Page
VI. Consideration of Frequency Specifications in QFT	6-1
6.1 Introduction	6-1
6.2 Embedding the Frequency Constraints in Deriving the Tracking Models	6-1
6.3 The Prefilter Phase Constraints	6-2
VII. Conclusions and Recommendations	7-1
7.1 Conclusions	7-1
7.2 Recommendations	7-2
Appendix A. Device Fundamentals	A-1
A.1 Motor Fundamentals	A-1
A.2 Pump and Fluid Fundamentals	A-3
Appendix B. Plant Models	B-1
Appendix C. QFT CAD Batch Load Matlab M-File	C-1
C.1 Background	C-1
C.2 Listing of the M-file <i>qftcad</i>	C-2
C.3 Listing of the M-file <i>isreal</i>	C-5
Bibliography	BIB-1
Vita	VITA-1

List of Figures

Figure	Page
2.1. Motor Model	2-1
2.2. Simplified Actuator Control System - Not Drawn to Scale	2-3
2.3. Bare EHA Block Diagram	2-6
2.4. ICAO Air Density for Standard Atmosphere as a Function of Altitude	2-7
2.5. Comparison of Full and Short Period Approximation for the Longitudinal Equations of Motion	2-8
3.1. Physical Block Diagram	3-2
3.2. Block Manipulation - L_1 Transmissivity Computation	3-2
3.3. Block Manipulation - L_1	3-3
3.4. Block Manipulation - L_2 Computation	3-3
3.5. Block Manipulation - L_2	3-4
3.6. Block Manipulation - L_3 Computation	3-4
3.7. Open Loop Block Structure	3-5
3.8. Bare Actuator Time Domain Response of Figure 2.3	3-6
3.9. Bare Actuator Time Domain Response of Figure 3.7	3-6
3.10. Two Feedback Loops in QFT Two Degrees of Freedom Structure	3-7
3.11. A typical modern fighter flight envelope and the flight conditions considered for $\frac{\alpha(s)}{\delta_e(s)}$	3-11
3.12. Bode Plots of the Inner Loop Plants	3-13
3.13. Inner Loop Plant Templates	3-14
3.14. Nominal Plant Selection	3-14
3.15. Inner Loop Compensator Design - The loop transmission is steered through the trough, as required.	3-16
3.16. Inner Loop Stability Simulation Using the Inner Loop Compensator	3-17

Figure	Page
3.17. Inner Loop Time Domain Unit Step Input Response Simulation Using the Inner Loop Compensator. The design rise time goals are shown as the set of dashed lines.	3-17
3.18. Small Signal Frequency Specification	3-18
3.19. Disturbances in the QFT Feedback Structure	3-20
3.20. Outer Loop Plant Templates	3-21
3.21. Outer Loop Nominal Plant Selection	3-22
3.22. Outer Loop Bounds	3-22
3.23. Outer Loop Compensator Design	3-23
3.24. Outer Loop Prefilter Design	3-24
3.25. Outer Loop Stability Simulation	3-25
3.26. Outer Loop Disturbance Rejection Simulation	3-25
3.27. Outer Loop Tracking Simulation	3-26
3.28. Outer Loop Time Domain Unit Step Disturbance Response Simulation	3-27
3.29. Outer Loop Time Domain Unit Step Input Response Simulation	3-27
3.30. Close Up of the Outer Loop Time Domain Unit Step Input Response Simulation	3-28
3.31. Outer Loop Small-Signal Frequency Domain Sinusoidal Input Response Simulation	3-28
4.1. The Nominal Plant Time Domain Figures of Merit for Unit Step Input	4-2
4.2. The Frequency Response Plot of the Nominal Plant	4-5
4.3. Deviations from the Nominal Response due to Pump Displacement Parameter D_m Variations	4-8
4.4. Addition of LVDT Sensor Noise in QFT Feedback Structure	4-9
4.5. Unit Step Response with LVDT Signal to Noise Ratio of 100. (a) High Gain design response (b) QFT design response	4-11
4.6. Unit Step Response with LVDT Signal to Noise Ratio of 20. (a) High Gain design response (b) QFT design response	4-11
4.7. Unit Step Response with LVDT Signal to Noise Ratio of 10. (a) High Gain design response (b) QFT design response	4-12

Figure	Page
4.8. Unit Step Response with LVDT Signal to Noise Ratio of 4. (a) High Gain design response (b) QFT design response	4-12
4.9. Unit Step Response with LVDT Signal to Noise Ratio of 2. (a) High Gain design response (b) QFT design response	4-13
4.10. Unit Step Response with LVDT Signal to Noise Ratio of 1. (a) High Gain design response (b) QFT design response	4-13
4.11. Relative Comparison of Noise Error Function due to the Changes in Signal to Noise Ratio	4-14
4.12. Unit Step Response with Sensor Bias Error of $\pm 1\%$	4-15
4.13. Unit Step Response with Sensor Bias Error of $\pm 10\%$	4-16
5.1. A Pitch Control Flight Control System	5-2
5.2. Time Domain Simulation of the Pitch Control System with a Simple First-Order Actuator Model and Nominal Plant Parameters	5-3
5.3. Frequency Domain Simulation of the Pitch Control System with a Simple First-Order Actuator Model and Nominal Plant Parameters	5-4
5.4. The Open Loop Frequency Response - Gain Margin 7.6 dB and Phase Margin Angle 35°	5-4
5.5. Time Domain Simulations of the Pitch Control System at Mach 0.7 and 30,000 ft Altitude. The dotted, dashed, and solid lines correspond to the results from the first-order conventional, the fourth-order conventional, and the EHA models, respectively.	5-6
5.6. Time Domain Simulations of the Pitch Control System at Mach 0.78 and 50,000 ft Altitude. The dotted, dashed, and solid lines correspond to the results from the first-order conventional, the fourth-order conventional, and the EHA models, respectively.	5-6
5.7. Time Domain Simulations of the Pitch Control System at Mach 1.1 and 1,000 ft Altitude. The dotted, dashed, and solid lines correspond to the results from the first-order conventional, the fourth-order conventional, and the EHA models, respectively.	5-7

Figure	Page
5.8. Frequency Domain Simulations of the Pitch Control System at Mach 0.7 and 30,000 ft Altitude. The dash-dotted, dashed, and solid lines correspond to the results from the first-order conventional, the fourth-order conventional, and the EHA models, respectively.	5-8
5.9. Frequency Domain Simulations of the Pitch Control System at Mach 0.78 and 50,000 ft Altitude. The dash-dotted, dashed, and solid lines correspond to the results from the first-order conventional, the fourth-order conventional, and the EHA models, respectively.	5-9
5.10. Frequency Domain Simulations of the Pitch Control System at Mach 1.1 and 1,000 ft Altitude. The dash-dotted and solid lines correspond to the results from the first-order conventional and the EHA models, respectively.	5-9
5.11. The Inner Loop Root Locus with the Fourth-Order Conventional Actuator - Eq. (5.4)	5-11
5.12. The Inner Loop Root Locus with the Fourth-Order Conventional Actuator Near the Origin - Eq. (5.4)	5-11
5.13. The Inner Loop Root Locus with the EHA - Eq. (5.5)	5-12
5.14. The Inner Loop Root Locus with the EHA Near the Origin - Eq. (5.5)	5-12
6.1. Time Domain Responses of Simple First-Order Tracking Model (Solid Line) and Complex Tracking Model (Dashed Line)	6-3
6.2. Frequency Domain Responses of Simple First-Order Tracking Model (Solid Line) and Complex Tracking Model (Dashed Line)	6-3
6.3. A Prefilter Design that Satisfy the Magnitude Constraints but not Phase Constraints	6-5
6.4. A Prefilter Design that Satisfy the Magnitude and Phase Constraints	6-5
A.1. DC Motor Principle - Top View	A-1
A.2. Brushless DC Motor	A-2
A.3. Torque Ripples	A-3
A.4. Principle of Servovalve	A-4

List of Tables

Table	Page
3.1. Inner Loop Specification	3-9
3.2. Subsonic Envelope Flight Conditions	3-10
3.3. Supersonic Envelope Flight Conditions	3-11
3.4. The Inner Loop Plants	3-12
3.5. The Outer Loop Plants	3-21
4.1. Time Domain Parametric Sensitivity of QFT Design. The numbers enclosed in the parenthesis denote the change from the nominal response in percent.	4-3
4.2. Time Domain Parametric Sensitivity of High Gain Design. The numbers enclosed in the parenthesis denote the change from the nominal response in percent.	4-4
4.3. Frequency Domain Parameter Sensitivity - Attenuation. The numbers enclosed in the parenthesis denote the change from the nominal response in percent. No parenthesis within the block denotes zero deviation.	4-6
4.4. Frequency Domain Parameter Sensitivity - Phase Lag. The numbers enclosed in the parenthesis denote the change from the nominal response in percent. No parenthesis within the block denotes zero deviation.	4-7
4.5. Noise Error Function Relative to the Signal to Noise Ratio	4-14
5.1. The Pitch Flight Control System Figures Of Merit	5-5
B.1. Full Set of Inner Loop Plants	B-1
B.2. Reduced Set of Inner Loop Plants	B-2
B.3. Full Set of Outer Loop Plants	B-3
B.4. Reduced Set of Outer Loop Plants	B-4

Abstract

The Electro-Hydrostatic Actuator (EHA) technology offers a higher degree of combat survivability and easier maintainability of the aircraft flight control system, because all the components necessary to operate the actuator are collocated with the actuator. Quantitative Feedback Theory (QFT) is used to design a control system for the EHA. The impact of parameter variations, sensor noise, and flight conditions are explicitly considered in the design process. The solution utilizes a two loop QFT feedback structure. The inner loop structure stabilizes the motor's angular velocity and decreases the outer loop's uncertainty. The outer loop structure controls the RAM piston's position to track the input command. The resulting design is not only robust with respect to plant parameter variations, but is also insensitive to the effects of sensor noise. The actuator's phase lag is reduced by incorporating phase constraints in the QFT design paradigm. QFT is shown to be a viable tool in solving a real-world problem.

ELECTRO-HYDROSTATIC ACTUATOR CONTROLLER DESIGN USING QUANTITATIVE FEEDBACK THEORY

I. Introduction

1.1 Background

Conventional aircraft actuators receive hydraulic power from a centralized hydraulic system. Centralized hydraulic systems, with extensive hydraulic line networks spread throughout the aircraft, have proven difficult to maintain in the past [16]. A failure in the system may cause the whole system to shut down, rendering the aircraft uncontrollable. For example, consider a case in which shrapnel from an exploding missile has cut into the hydraulic line that connects the central pump to the aileron actuator. The aileron actuator will be rendered useless immediately. The subsequent loss of hydraulic fluid and pressure may cause the hydraulic system itself to fail, forcing the pilot of the uncontrollable aircraft to eject over what may be hostile territory. Hydraulic fuzes may prevent excessive hydraulic fluid loss if situated between the damaged line and the central pump; hence, they are only partially effective.

The Electro-Hydrostatic Actuator (EHA) technology offers a higher degree of combat survivability and easier maintainability of the aircraft flight control system. All components necessary to operate the actuators are collocated with the actuator, i.e., are built into each EHA [16]. Aircraft electrical power and control signals are still required. This substantially reduces the profile exposed to hostile fire. In other words, if one of the EHAs is damaged by hostile fire, the damage will be localized to that actuator only. Thus, the aircraft will remain controllable since other EHAs remain fully functional. Furthermore, since the EHA does not require long hydraulic lines, the required maintenance time and equipment can be reduced. Moreover, since the EHA does not require a cen-

tral hydraulic system, the current ground maintenance equipment for the central hydraulic system will no longer be required.

1.2 Problem Definition

A controller system for the EHA needs to be designed. WL/FIG specified the use of the Quantitative Feedback Theory (QFT) controls design method in order to establish a rigorous design procedure and ease the transition of the EHA from one aircraft platform to another. QFT is a robust controls design theory that emphasizes the use of output feedback to achieve the desired system performance despite structured plant uncertainty and disturbances [3]. The specified research objectives include:

1. Document representative mathematical models for the EHA, based on data provided by WL/FIGS.
2. Develop QFT type specifications based on the current EHA development requirements.
3. Perform sensitivity analyses on the EHA control systems. This should include sensitivity to variations in load, component efficiencies, physical plant parameters, and sensor noise.
4. Identify a reasonable set of plant variations for the EHA based on sensitivity analysis.
5. Design a robust control system that will control the EHA within the specifications in the presence of predicted variations.
6. Perform actuator and aircraft level linear simulations of the resulting control systems.
7. Analyze the simulation results for compliance with the specifications

1.3 Literature Review

The current EHA controller design was not based on rigorous design procedures. Using the non-linear actuator model, ad hoc trial and error design methods were used until the desired per-

formance was obtained. The resulting controller design deliberately saturated the inner loop by using a high forward gain [13]. Unfortunately, this saturated behavior may not be desirable in the small-signal region, due to its susceptibility to sensor noise. Furthermore, the controller design was based only on operation at the actuator level, without considering the aircraft and the flight control system. More specifically, the prototype EHA and controller were designed to meet the current F-18 aileron actuator specifications only. Plant variation under different operating conditions were also not considered. The sensitivities of the system performance to parameter variations or sensor noise had not been explored. Thus, if the EHAs were to be placed on another aircraft or other flight control surfaces on the F-18, the controller designer will face problems maintaining the commonality of the design process from one EHA controller to another.

In contrast, the QFT controller is designed from the start to meet certain performance specifications, known as figures of merit (FOM). QFT is based on rigorous mathematical reasoning. This affords the commonality from one EHA application to another to be maintained. The QFT design method yields a methodical design and thought process by ensuring that plant variations are considered in the design process up front. Furthermore, the QFT design ensures reduced sensitivity to sensor noise by limiting the control loop gain to a minimum level necessary to meet specifications.

1.4 Approach

A robust QFT control system is designed to obtain the desired response from the EHA. The term *robust* in control theory implies that a system under control remains stable throughout its operating envelope, rejects disturbances, and results in minimum degradation in the performance specifications. A unity gain feedback system, which uses the output feedback, assures that the output tracks the input values despite parametric uncertainties or disturbances. The unity gain system, however, cannot control the tracking response rate. The output of a unity gain feedback system with uncertain plant models can vary depending on the plant conditions. The output of a robust control feedback system with uncertain plant models won't vary much.

Plant uncertainties may be caused by manufacturing tolerances. For example, a component A is specified to be 10 ± 0.1 millimeters long. In a large production run, the length of component A may be anywhere between 9.9 to 10.1 millimeters. This tolerance range may be substantial enough to produce noticeable variations in the plant model. Plant uncertainties may also be caused by the environment, viz., the system's operating conditions. For example, aircraft models' parameters display large variations depending on altitude and airspeed. Since modern aircraft flight envelopes are quite large, the variations are quite substantial. Conventional control systems subdivide the flight envelope into numerous regions (40+ regions in case of the F-16), then implement a controller for each region using gain scheduling [8, 9]. Finally, the performance of various components decay over time, introducing an additional element of uncertainty.

The QFT design paradigm accounts for the plant variations in the design procedure. It is a linear design technique for designing a linear robust controller for linear or nonlinear control systems [3]. As long as all the QFT design requirements are met, the output responses are guaranteed to conform to the specification boundaries. The initial step in the design process is to establish the upper and lower performance tracking boundaries. The maximum allowable disturbance is used to determine the disturbance boundary. The phase margin angle, gain margin, or maximum peak value is used to establish the stability boundary. These combined boundaries establish the limitation of the system performance. The next step is to analyze the system to determine the parameters which will cause noticeable variations to the plant. The system, once modeled only as a single plant transfer function in other design methods, is now modeled more completely as a set of plant transfer functions. The variations now form a closed region in the Nichols magnitude and phase chart called the template; larger template sizes indicate a higher degree of plant uncertainty. Templates at different frequencies differ in size and shape.

The most important aspect of this research is to thoroughly analyze the bare actuator plant, in order to find the sources of plant variation. By examining the magnitude of the anticipated variations, a proper QFT template can be derived. The three largest sources of variations are the

fluctuations in aerodynamic load on the flight control surfaces, motor torque, and hydraulic pump fluid pressure.

Once the templates have been established for a significant set of frequencies, the controller design takes place in two stages. A compensator is used to control the motor angular velocity in the inner loop. This inner loop design aids the outer loop design by decreasing the outer loop template size and increasing the outer loop gain margin. A compensator and prefilter is used to control the piston RAM position in the outer loop. The outer loop design allows the actuator to track given commands.

1.5 Simulation

The design verifications are done through Simulink simulations. The design validations are performed on two levels: the actuator level and the complete flight control system level.

A typical flight control system may contain fourth-order or higher aircraft models. Adding a high-order actuator package (actuator, prefilter, and controller) model to the flight control system model may result in an unmanageably high-order flight control system. Computer simulations of any high-order models may suffer from numerical problems [9]. Hence, the actuator system model must be reduced to a lower order to achieve realistic simulation results.

The first phase of the test concentrates on the actuator performance. Linear simulations are used to test the controller in the small-signal operating region. The time domain simulation analysis will verify the rise time and tracking characteristics of the actuator. Frequency domain analysis will verify the attenuation and phase characteristics. The second phase of the test concentrates on the flight control system level, also in the small-signal region.

1.6 Limitations

The main thrust of the QFT controller design is to limit the scope of the problem to a small-signal linear operating region, and avoid any limit saturation. Non-linearity exists in many

different elements of the EHA. The flow rate Q is non-linear except for a very small operating region. The motor angular rate is also non-linear except for a small operating region. QFT, which is a linear control design method, is ideal for these small-signal problems. Indeed, the high gain ('Bang Bang') design may be the most efficient control system if only the large-signal operating region and high signal to noise ratio conditions are considered (SNR) [10]. The actuator can be commanded at the maximum slew rate, until the desired position is achieved. In the large-signal region, the commanded signal is so large that the sensor noise may play a minimal role, viz., $SNR \gg 1$. However, the same high gain design may suffer from the effects of sensor noise in the small-signal region where the signal to noise ratio is much lower [9]. Hence, a dual mode controller which operates with the high gain controller design in the large-signal domain and the QFT controller design in the small-signal domain is required to maximize the actuator performance and to minimize the effects of sensor noise.

A set of parameter values, provided by the EHA designers, is used for the design. The values used are the best available at the onset of this design, but may have changed since then. The values of the flight control surface inertia and damping parameters, J_L and B_L are for the F-18 aileron aerodynamic control surface only; even though this design project is using the actuator to control the F-16 stabilator. The stabilator's EHA presents a more interesting design problem since the stabilator is the most important flight control surface. The differences between the F-18 aileron and F-16 stabilator are the mass properties and surface areas. The stabilator is larger and heavier than the aileron. Thus, a more powerful actuator is needed to drive the stabilator than to drive the aileron. The EHA for the aileron currently being designed is rated around 13,000 lb_f , while an EHA rated at 34,000 lb_f is required for the F-16 stabilator [15]. But by using the mass properties of the F-18 aileron instead of the F-16 stabilator, a smaller stabilator which only requires 13,000 lb_f to control is simulated.

The purpose of this thesis is to obtain a realistic set of structured plant parameter variations. Unfortunately, parameter variability data was not available from the EHA contractor. Due to this

lack of data, straight $\pm 10\%$ variations from the nominal values are used during the QFT design procedures. This may not be the most desirable method, but it is the only option available at this time.

1.7 Overview of Thesis

In Chapter 2, a linear mathematical model of the EHA is derived. The models for individual EHA components; motor, pump, piston, flight control surface inertia, and hinge moment, are explained in detail.

In Chapter 3, the EHA model is rearranged to form the standard QFT feedback structures. The inner loop controller is designed to increase the outer loop robustness. The outer loop controller and prefilter are designed to enforce the tracking of commands. The resulting controller and prefilter design comply with the given set of specifications.

In Chapter 4, the sensitivities of the EHA and high gain control system, to parameter variations and sensor noise, are analyzed. The QFT design is compared against the high gain design for sensor noise and bias handling characteristics.

In Chapter 5, the EHA model used in a simple flight control system is compared against the same flight control system with the first-order and fourth-order conventional hydraulic actuator models.

In Chapter 6, two additional design steps to augment the current QFT design paradigm are proposed. These two steps are necessary in order to design a control system for some minimum-phase problems where the frequency specifications dominate the design constraints over the time domain specifications.

II. Models

2.1 Motor

Motors with the rotor moment of inertia J_m [$in * lb * sec^2$] and electro-mechanical damping B_m [$in * lb * sec$] (see Fig. 2.1), are subject to variations in the motor torque and its associated variations in the rotor speed ω_m . The torque due to the load counteracts the torque generated by the motor, resulting in reduced net torque. Perturbation may also be caused by variations of the load torque. This relationship is expressed as,

$$\tau_e(s) = \tau_{cmd}(s) - \tau_{load}(s) = J_m s \omega_m(s) + B_m \omega_m(s) \quad (2.1)$$

where τ_{load} is the load torque due to the differential pressure of the fluids. This results in

$$\frac{\omega_m(s)}{\tau_e(s)} = \frac{1}{J_m s + B_m} \quad (2.2)$$

Detailed discussions of motor fundamentals are given in Appendix A.

2.2 Pump and Fluid

Electric motors have a limited torque-to-mass ratio, due to the finite and limited magnetic flux density that can be generated [2]. High pressure hydraulic systems, with the system pressure

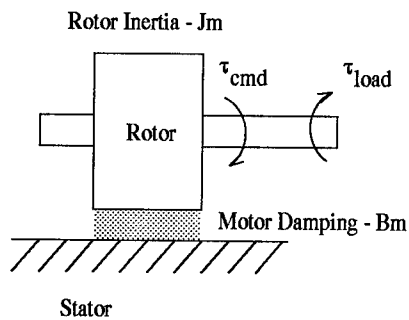


Figure 2.1 Motor Model

of 2000 to 5000 psi, can generate high forces resulting in higher torque-to-mass ratios than electric motors. Generally, high pressure hydraulic systems are stiffer against the load than electric motors. The EHA utilizes a DC motor to pump high pressure fluid into the piston chamber. The DC motor internal to the EHA converts the electrical power into mechanical power. It is the pump that converts this mechanical power into hydraulic power. The hydraulic power, acting against the piston, is converted to mechanical power capable of moving large flight control surfaces.

The flow rate generated by the pump is proportional to the motor rotation rate as in Eq. (2.3)

$$Q_m = \frac{D_m}{2\pi} \omega_m, \quad (2.3)$$

where D_m [in^3/rev] represents the pump displacement constant.

The flow rate of the hydraulic fluid is primarily dependent on two factors: change in chamber volume and change in pressure due to the compressibility effect of the fluid. The chamber volume changes as the piston moves through the chamber at speed \dot{X}_p . The flow rate due to the changes in chamber volume is then expressed as $\pm A\dot{X}_p$. Secondary fluid effects include the fluid compressibility, internal leakage flow, and external leakage flow. The EHA designers elected to represent the secondary effects of the fluid with a first-order transfer function.

$$\delta Q(s) = Q_m(s) - AsX_p = K_s sP(s) + C_t P(s) \quad (2.4)$$

This results in

$$\frac{P(s)}{\delta Q(s)} = \frac{1}{K_s s + C_t} \quad (2.5)$$

Detailed discussions of pump and fluid fundamentals are given in Appendix A.

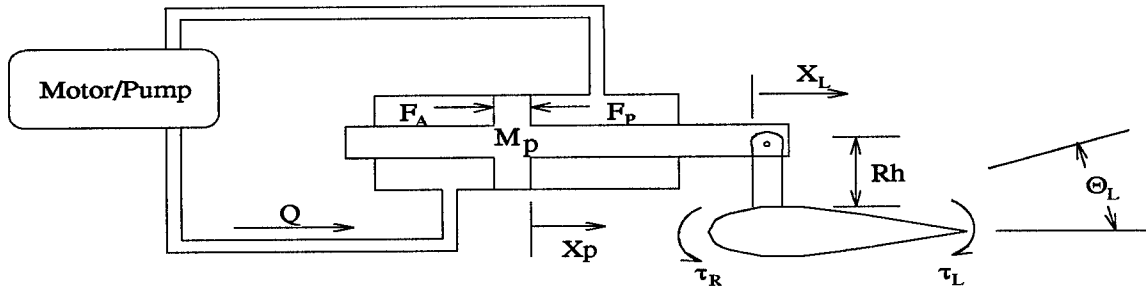


Figure 2.2 Simplified Actuator Control System - Not Drawn to Scale

2.3 Piston and Flight Control Surface

2.3.1 Piston and Flight Control Surface Fundamentals. The pressure developed by the pump and fluid acts on the piston surface (see Fig. 2.2), causing the RAM to extend or retract. This force then generates a torque through a hinge to deflect the control surface.

This torque has to overcome two load components: control surface inertia and aerodynamic loads. The control surface inertia is primarily due to the fact that the control surface has certain size and mass. The aerodynamic load only occurs in flight, when the air pressure over the control surface applies aerodynamic forces to it. The aerodynamic load is determined by three factors: the surface area of the flight control surface, aerodynamic loading which varies with altitude and airspeed, and the surface's relative angle to the wind. The surface angle to the wind depends on the angle of surface deflection and on the aircraft's angle of attack.

2.3.2 Piston and Flight Control Surface Dynamics.

Flexible Hinge Joint Model. The magnitude of F_A acting on the piston is equal to $\mathcal{P}A$, where \mathcal{P} is the differential pressure developed by the pump and fluid and A [in^2] is the surface area of the piston. Thus, the force created by the pump and fluid can be expressed as

$$F_A = \mathcal{P}A \quad (2.6)$$

The piston dynamics, with the piston mass M_p [$lb_f * sec^2/in$] and piston damping B_p [$lb_f * sec/in$], can be described by a second-order model in Eq. (2.7).

$$F_A - F_P = M_p s^2 X_p + B_p s X_p \quad (2.7)$$

The resulting torque acting on the flight control surface due to this force imbalance can be described by

$$\tau_R = \frac{K_h}{R_h} (X_p - X_L) \quad (2.8)$$

where K_h [$in * lb/rad$] is the hinge stiffness constant and R_h [in] is the hinge length. The stabilator inertia acts against the torque generated by the actuator, such that

$$\tau_R - \tau_L = J_L s^2 \Theta_L + B_L s \Theta_L \quad (2.9)$$

where τ_L is the torque created by the aerodynamic load and stabilator inertia. The variables J_L [$in * lb * sec^2$] and B_L [$in * lb * sec$] represent the mass properties of the flight control surface.

Stiff Hinge Joint Model. Equations (2.7 through 2.9) represent a rather complex model of the load dynamics. The complexity of the model can be reduced if the linkage between the actuator and flight control surface is considered as being rigid. This is a valid assumption, since the natural frequency of the hinge for a well designed system is much greater than the bandwidth frequency. The assumption of rigidity breaks down at high frequencies, but can safely be ignored for the controller design procedure since it is well above the bandwidth frequency.

The piston and load dynamics are still expressed as

$$F_A - F_P = M_p s^2 X_p + B_p s X_p \quad (2.10)$$

$$\tau_R - \tau_L = J_L s^2 \Theta_L + B_L s \Theta_L \quad (2.11)$$

Divide Eq. (2.11) by R_h to obtain

$$F_R - \frac{\tau_L}{R_h} = \frac{J_L s^2 \Theta_L + B_L s \Theta_L}{R_h} \quad (2.12)$$

Assuming rigidity of the hinge assembly, $F_R \approx F_P$. Hence, adding Eqs. (2.10) and (2.12) results in,

$$F_A - \frac{\tau_L}{R_h} = M_p s^2 X_p + B_p s X_p + \frac{J_L s^2 \Theta_L + B_L s \Theta_L}{R_h} \quad (2.13)$$

where τ_L is defined as

$$\tau_L = (Load_{aero}) \Theta_L \quad (2.14)$$

Since rigidity implies that $X_p = X_L$ and $\Theta_L = \frac{X_p}{R_h}$, Eq. (2.13) is further reduced to

$$F_e = F_A - \frac{\tau_L}{R_h} = (M_p + \frac{J_L}{R_h^2}) s^2 X_p + (B_p + \frac{B_L}{R_h^2}) s X_p \quad (2.15)$$

or expressed in a transfer function form as

$$\frac{X_p(s)}{F_e(s)} = \frac{1}{s[(M_p + \frac{J_L}{R_h^2})s + (B_p + \frac{B_L}{R_h^2})]} \quad (2.16)$$

Equation (2.16) represents a simpler model of the load dynamics. A complete model of the bare EHA, without any of the control structure, is shown in Fig. 2.3 using the individual model segments derived in this chapter.

2.4 Aerodynamic Loads

2.4.1 Hinge Moment. The term aerodynamic loads mentioned in Section 2.3 describes the amount of torque resistant against the piston motion. A load generated by the flow of air above and below the flight control surface applies a torque on the hinge assembly, which in turn adds

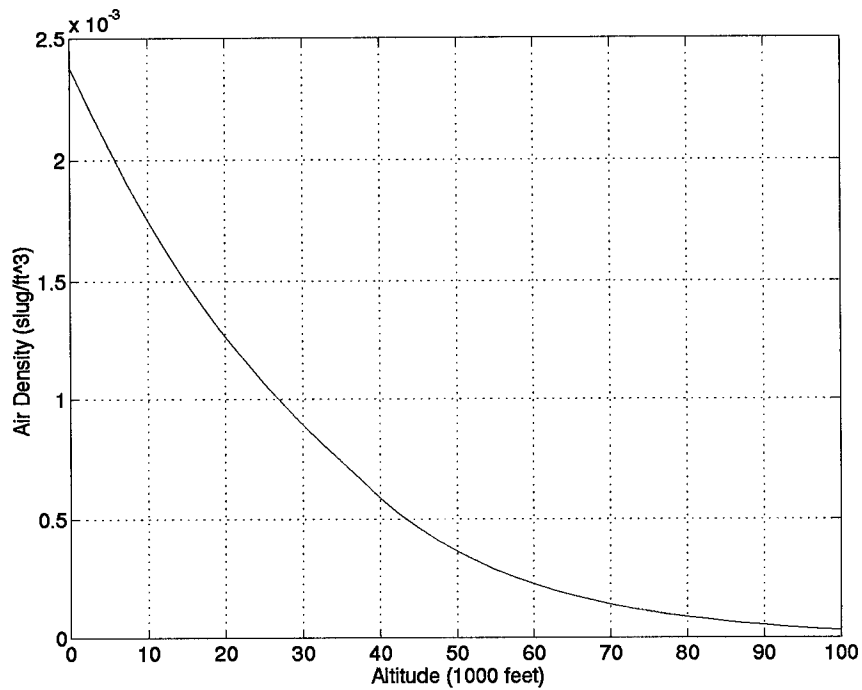


Figure 2.4 ICAO Air Density for Standard Atmosphere as a Function of Altitude

2.4.2 *Short Period Approximation.* The full longitudinal channel equations of motion can be modelled with a four state matrix as shown in Eq. (2.20).

$$\begin{bmatrix} \dot{\theta} \\ \dot{u} \\ \dot{\alpha} \\ \dot{q} \end{bmatrix} = \begin{bmatrix} 0.0 & 0.0 & 0.0 & 1.0 \\ x\theta & xu & x\alpha & xq \\ z\theta & zu & z\alpha & zq \\ m\theta & mu & m\alpha & mq \end{bmatrix} \begin{bmatrix} \theta \\ u \\ \alpha \\ q \end{bmatrix} + \begin{bmatrix} 0 & 0 \\ x_{\delta e} & x_{\delta f} \\ z_{\delta e} & z_{\delta f} \\ m_{\delta e} & m_{\delta f} \end{bmatrix} \begin{bmatrix} \delta_{elevator} \\ \delta_{flap} \end{bmatrix} \quad (2.20)$$

However, if the forward speed is assumed constant (i.e., $u \approx 0$), a short period approximation can then be extracted from Eq. (2.20). The X force equation is neglected since it does not significantly contribute to the short period oscillation [1]. Thus, the short period approximation of

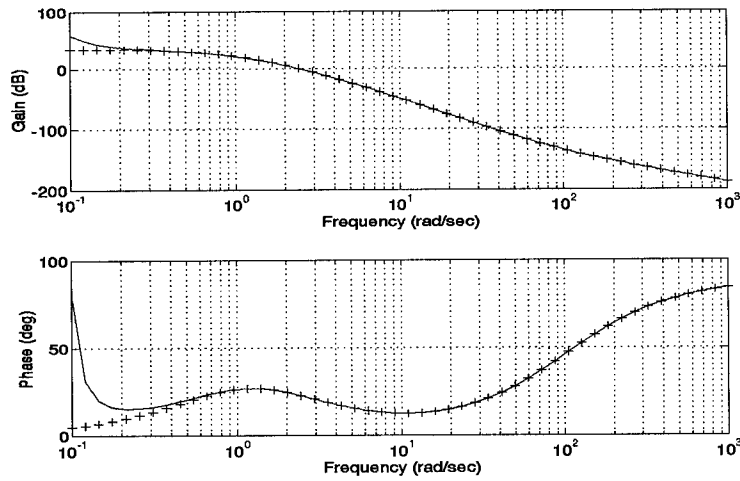


Figure 2.5 Comparison of Full and Short Period Approximation for the Longitudinal Equations of Motion

the longitudinal channel is written as,

$$\begin{bmatrix} \dot{\alpha} \\ \dot{q} \end{bmatrix} = \begin{bmatrix} z\alpha & zq \\ m\alpha & mq \end{bmatrix} \begin{bmatrix} \alpha \\ q \end{bmatrix} + \begin{bmatrix} z_{\delta e} & z_{\delta f} \\ m_{\delta e} & m_{\delta f} \end{bmatrix} \begin{bmatrix} \delta_{elevator} \\ \delta_{flap} \end{bmatrix} \quad (2.21)$$

This yields a second-order minimum-phase transfer function of the form:

$$\frac{\alpha(s)}{\delta(s)} = \frac{-K(s+a)}{(s+b)(s+c)} \quad (2.22)$$

For the frequency of interest, the short period approximation closely resembles the full state model. As seen in Fig 2.5, the phase and attenuation characteristics are closely matched at high frequency. The solid lines represent the full state model frequency response and '+' lines represent the short period model frequency response. The approximation, as seen in the figure, is not valid for frequencies below 0.5 rad/sec due to the effects from the slow phugoid mode.

III. QFT Controller and Prefilter Design

3.1 Block Model Manipulation

In order to proceed with a QFT design, the block model as shown in Fig. 2.3 and reproduced in Fig. 3.1, must first be rearranged to a set of state space models or transfer functions. The detailed block diagram must be simplified before a control structure can be added. Before proceeding with the reduction process, the transfer function blocks are re-labeled using the standard terms per following set of equations. Forward transfer function blocks are labeled as G_i , gain blocks are labeled as K_i , and the feedback transfer function block is labeled as H .

$$G_1(s) = \frac{1}{J_m s + B_m} = \frac{N_{G1}}{D_{G1}} \quad (3.1)$$

$$G_2(s) = \frac{1}{K_s s + C_t} = \frac{N_{G2}}{D_{G2}} \quad (3.2)$$

$$G_3(s) = \frac{1}{(M_p + \frac{J_L}{R_h^2})s + (B_p + \frac{B_L}{R_h^2})} = \frac{N_{G3}}{D_{G3}} \quad (3.3)$$

$$G_4(s) = \frac{1}{s} = \frac{N_{G4}}{D_{G4}} \quad (3.4)$$

$$H(s) = \bar{q} S_t R_h (C h_\alpha \frac{\alpha(s)}{\delta(s)} + C h_\delta \delta) = \frac{N_H}{D_H} \quad (3.5)$$

$$K_1 = \frac{D_m}{2\pi} \quad (3.6)$$

$$K_2 = A \quad (3.7)$$

$$K_3 = \frac{1}{R_h} \quad (3.8)$$

The intent of the reduction process is to manipulate the block model to form the standard inner and outer QFT loop structures. The inner loop is used to control the angular rate of the motor, while the outer loop is used to control the RAM position. Therefore, the first goal of the reduction process is to isolate the motor angular velocity, ω_m .

The first two block manipulation steps create the $L_1 = \frac{sX_p}{F_A}$ block shown in Fig. 3.2. The L_1 block isolates the RAM piston velocity feedback by mathematically decoupling it from the load dynamics. The L_1 block is the combined dynamics from the piston, load, and aerodynamic

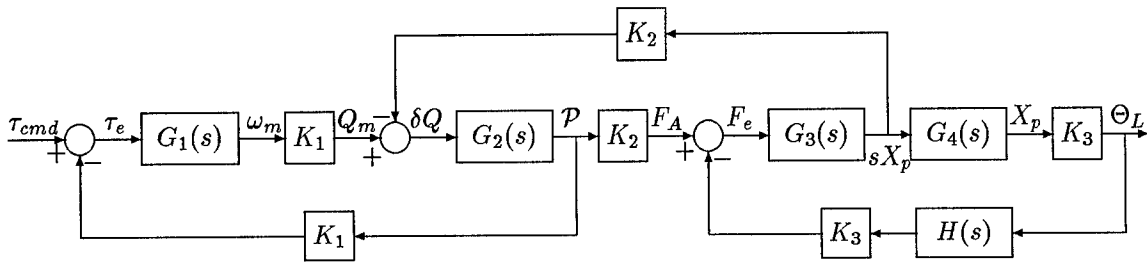


Figure 3.1 Physical Block Diagram

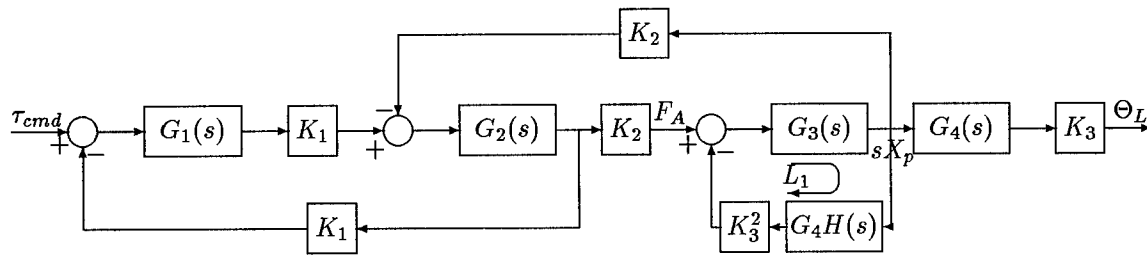


Figure 3.2 Block Manipulation - L_1 Transmissivity Computation

feedback. The resulting $L_1(s)$ transfer function is

$$\begin{aligned}
 L_1(s) &= \frac{\frac{N_{G3}}{D_{G3}}}{\frac{D_{G4}D_{G3}D_H + K_3^2 N_{G4}N_{G3}N_H}{D_{G4}D_{G3}D_H}} \\
 &= \frac{N_{G3}D_{G4}D_H}{D_{G4}D_{G3}D_H + K_3^2 N_{G4}N_{G3}N_H} = \frac{N_{L1}}{D_{L1}}
 \end{aligned} \tag{3.9}$$

The next two block manipulation steps shown in Figs. 3.4 and 3.5, create the $L_2 = \frac{sX_p}{Q_m}$ block. The L_2 block collapses the velocity feedback to the flow rate, Q_m . The L_2 block models the combined dynamics entailing the fluid, pump, piston, load, and the aerodynamic feedback.

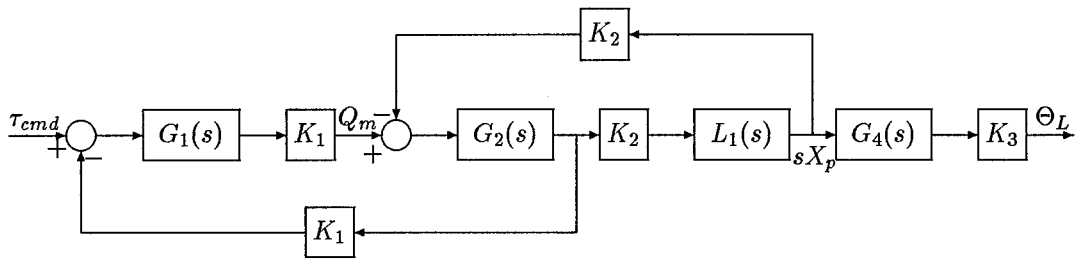


Figure 3.3 Block Manipulation - L_1

$$\begin{aligned}
 L_2(s) &= \frac{\frac{K_2 N_{G_2} N_{L_1}}{D_{G_2} D_{L_1}}}{\frac{D_{G_2} D_{L_1} + K_2^2 N_{G_2} N_{L_1}}{D_{G_2} D_{L_1}}} \\
 &= \frac{K_2 N_{G_2} N_{L_1}}{D_{G_2} D_{L_1} + K_2^2 N_{G_2} N_{L_1}} = \frac{N_{L_2}}{D_{L_2}}
 \end{aligned}
 \tag{3.10}$$

The next two block manipulation steps create the L_3 block. The L_3 block represents the inner loop QFT plant model. The L_3 block contains all the dynamics from the fluid, pump, piston, load, and aerodynamic feedback. Thus using a standard set of block manipulation rules, Fig. 2.3 is reduced to Fig. 3.7.

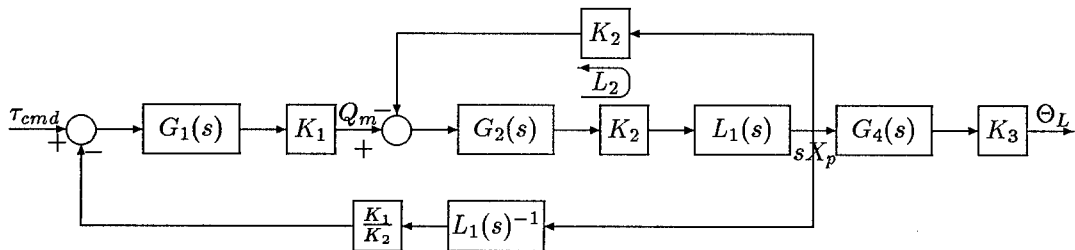


Figure 3.4 Block Manipulation - L_2 Computation

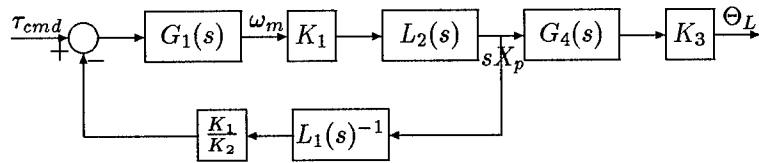


Figure 3.5 Block Manipulation - L_2

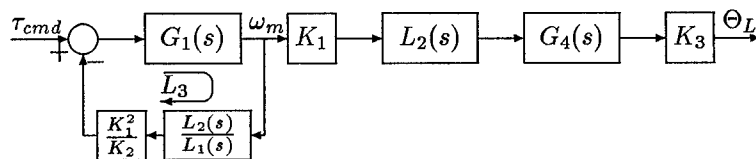


Figure 3.6 Block Manipulation - L_3 Computation

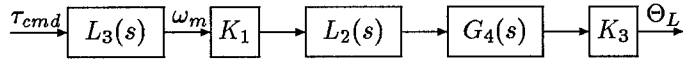


Figure 3.7 Open Loop Block Structure

$$\begin{aligned}
 L_3(s) &= \frac{\frac{N_{G1}}{D_{G1}}}{\frac{K_2 D_{G1} D_{L2} N_{L1} + K_1^2 N_{L2} D_{L1} N_{G1}}{K_2 D_{L2} N_{L1} D_{G1}}} \\
 &= \frac{K_2 N_{G1} N_{L1} D_{L2}}{K_2 N_{L1} D_{G1} D_{L2} + K_1^2 N_{L2} D_{L1} N_{G1}} = \frac{N_{L3}}{D_{L3}}
 \end{aligned} \tag{3.11}$$

3.2 Block Model Verification

The modeling reduction process is validated using time domain simulations of the bare plant model and the transfer functions computed by the block reduction process, respectively. Figures 2.3 and 3.7 are each simulated by use of Simulink blocks in order to verify the accuracy of Fig. 3.7. Figures 3.8 and 3.9 represent the results of this simulation. Comparing these two figures verifies the accuracy of block diagram manipulations. Furthermore, transfer functions computed using the Matlab function *linmod* and computed by use of

$$G(s) = \frac{K_1 K_3 N_{L3} N_{L2}}{D_{L3} D_{L2} D_{G4}} \tag{3.12}$$

are identical. Both methods yield identical transfer functions, when the minimum realization pole-zero cancellation method is applied to reduce the model order of the transfer function computed using Eq. (3.12).

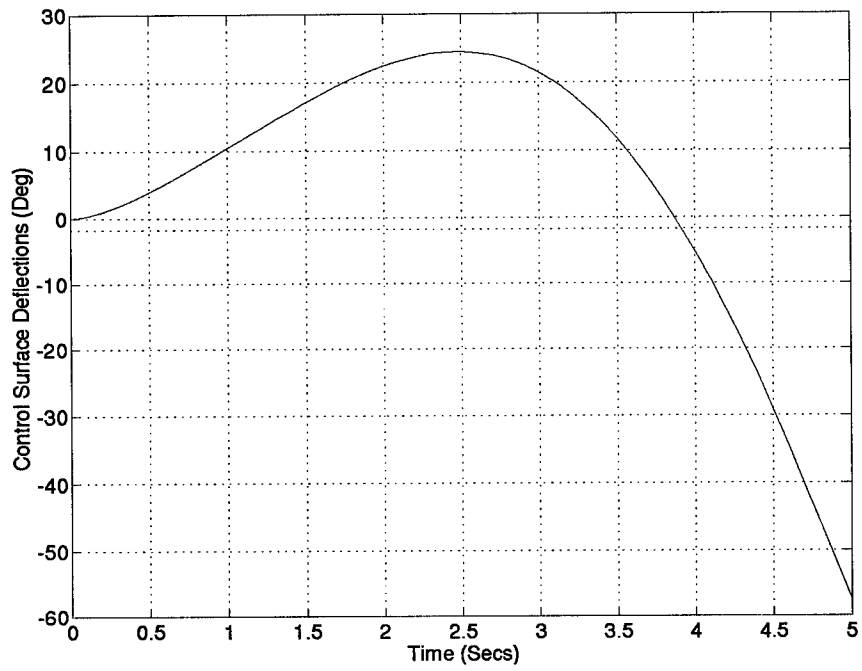


Figure 3.8 Bare Actuator Time Domain Response of Figure 2.3

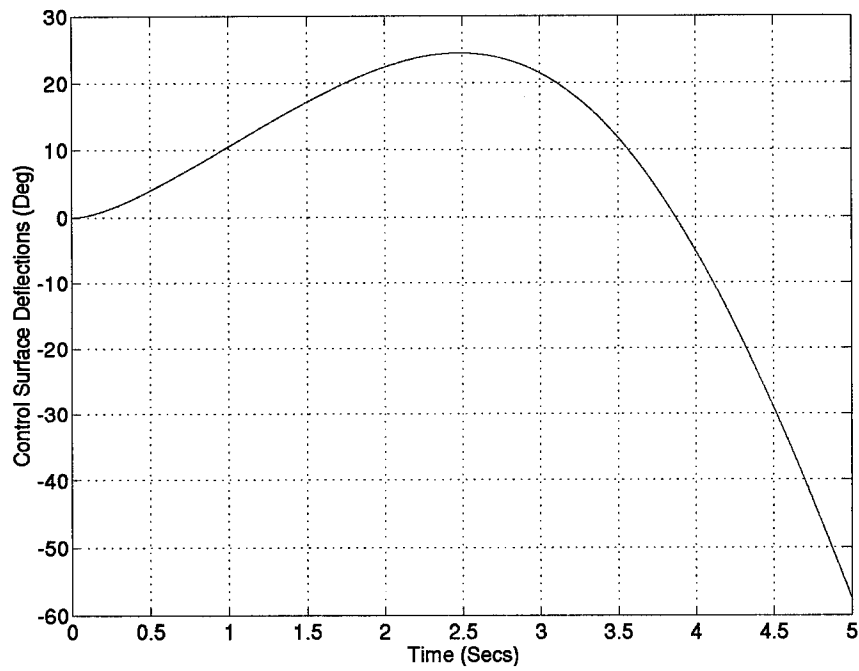


Figure 3.9 Bare Actuator Time Domain Response of Figure 3.7

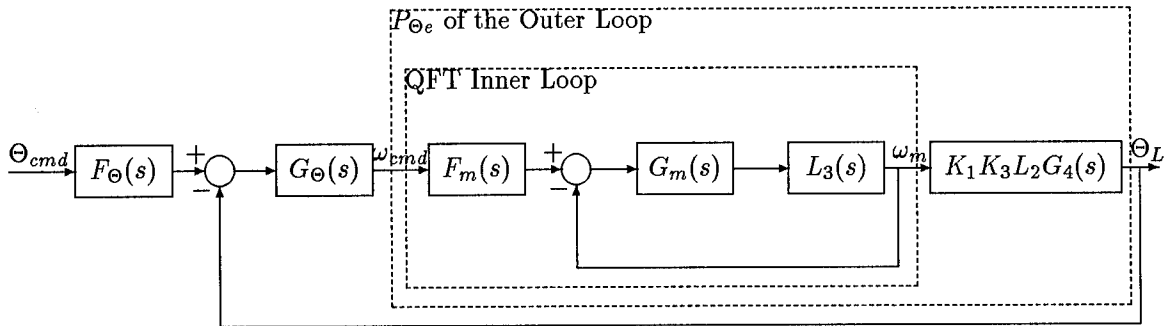


Figure 3.10 Two Feedback Loops in QFT Two Degrees of Freedom Structure

3.3 QFT Structure

Inner and outer feedback loops are used to control the bare actuator plant, resulting in the structure shown in Fig. 3.10. The inner loop controls the angular rate of the motor while the outer loop controls the surface deflection. Since tracking in the inner loop is not important, for its function is to reduce the uncertainty level of the outer loop, the inner loop prefilter can be set to unity. The tracking performance enforcement is relegated to the outer loop's prefilter F_{Θ} .

3.4 Inner Loop Controller Design

3.4.1 Inner Loop Specifications. The purpose of the inner loop design is to facilitate the design of a robust outer loop, without the problems associated with excessive gains. This inner loop robustness effectively shrinks the region of uncertainty (i.e., the template size) of the outer loop, while also increasing the outer loop gain margin. Even though the existing EHA controller design used state feedback for the inner loop, only a simple high forward gain element was used to drive the inner loop into saturation. The linear inner loop design using the QFT technique attempts to reduce the gain required to achieve the inner loop control. The EHA specifications are not given in a manner easily usable in designing controllers. For this design problem the inner loop specifications, or desired figures of merit, are derived based on conventional aircraft actuator

models.

The inner loop controls the angular rate of the electric motor. The direction of the motor rotation determines the flow direction of the hydraulic fluid, and ultimately the piston direction. It is important for the motor to be able to quickly build up to the commanded speed and then reverse direction, if necessary. However, since the outer loop tracks the commanded input, the inner loop does not necessarily have to track a given command with a particular set of figures of merit. Hence, the fast rise time is the primary concern, while arbitrary settling time and peak overshoot are acceptable. The inner loop should be robustly stable; thus, the inner loop must have a conservative phase margin angle.

The inner loop specifications consist of lower bound rise time (t_{rl}), upper bound rise time (t_{ru}), and phase margin angle. The rise time t_r denotes the time for the output response, on its initial rise, to change from 10 to 90 percent of the steady state value [3]. The phase margin angle is set conservatively at 45° . Disturbance rejection is considered only in the outer loop design.

The inner loop tracking bounds are determined by estimating the minimum desired rise time relative to the outer loop rise time. The outer loop nominal rise time is that of a standard first-order actuator's transfer function, $\frac{20}{s+20}$, about 0.11 seconds. It is then desired that the inner loop rise time be much faster, about ten times faster. The separation between the lower and upper tracking bounds, δ_r , must increase as the frequency increases. Hence, the lower bound B_L model must be of higher order than that of the upper bound B_U model. These requirements result in two tracking models; the upper tracking bound model, shown in Eq. (3.13), and the lower tracking bound model, shown in Eq. (3.14). The resulting rise times are shown in Table 3.1.

$$T_{ru}(s) = \frac{130}{s + 130} \quad (3.13)$$

$$T_{rl}(s) = \frac{6400}{(s + 80)(s + 80)} \quad (3.14)$$

Specification	Value Used
t_{ru}	0.016 sec
t_{ri}	0.041 sec
γ	45°

Table 3.1 Inner Loop Specification

3.4.2 Set of Plants in the Inner Loop. The set of plants in the inner loop is given in Appendix B. They are derived by varying all physical parameters by $\pm 10\%$ from the nominal values. These plants are all type 0. A wide range of aerodynamic load conditions are examined to see which set of flight conditions cause the largest variations (i.e., largest templates). Figure 3.11 shows the flight conditions considered. Outline of the flight conditions defines the flight envelope of typical modern fighters. Both subsonic and supersonic points, listed in Tables 3.2 and 3.3, at altitudes from 1000 to 50,000 ft are tested to determine the maximum template width. Two flight conditions help to determine the perimeter of the plant templates. The aircraft flying at the altitude of 1000 ft and speed of Mach 1.1 (e.g., point ac41) had one of the highest \bar{q} , while the aircraft flying at the altitude of 50,000 ft and speed of Mach 0.78 had one of the lowest \bar{q} (e.g., point ac28). While the dynamic pressure parameter \bar{q} plays the most significant role in enlarging the template size, the aircraft damping and natural frequencies for given altitude and airspeed also play a significant role. Even though the flight condition ac41 does not have the highest \bar{q} , it is located at an extreme edge of the envelope with extreme damping and natural frequency.

Using the reduction steps defined in Section 3.1, a set of 62 plants are identified for further study. Since the flight conditions ac28 and ac41 result in the largest template size, the EHA parameters are varied to enlarge the templates described by the flight conditions. Hence, the plant templates are formed from one set of 31 plants due to EHA parameter variations at the flight condition ac28 and one set of 31 plants due to EHA parameter variations at the flight condition ac41. When the templates with all the points are examined, it turns out that eight points per flight condition define the template perimeter. As can be seen in Fig. 3.14, the predominant source of the uncertainties (i.e., template size) is the flight condition. The template points 1 through 8

Points	Mach No.	Altitude (feet)	Airspeed (ft/sec)
ac1	0.24	1000	258.96
ac2	0.40	1000	443.75
ac3	0.60	1000	667.39
ac4	0.70	1000	778.89
ac5	0.90	1000	1001.64
ac6	0.26	5000	276.80
ac7	0.28	10000	292.04
ac8	0.30	10000	315.20
ac9	0.50	10000	537.50
ac10	0.70	10000	754.02
ac11	0.90	10000	969.88
ac12	0.31	15000	317.75
ac13	0.34	20000	341.34
ac14	0.40	20000	408.21
ac15	0.50	20000	515.65
ac16	0.70	20000	725.12
ac17	0.90	20000	933.28
ac18	0.38	25000	374.09
ac19	0.42	30000	404.25
ac20	0.50	30000	490.01
ac21	0.70	30000	694.41
ac22	0.90	30000	895.00
ac23	0.47	35000	442.36
ac24	0.53	40000	496.41
ac25	0.70	40000	672.50
ac26	0.90	40000	869.94
ac27	0.70	45000	667.97
ac28	0.78	50000	744.60
ac29	0.90	50000	866.96
ac30	0.30	1000	331.09
ac31	0.32	5000	351.50
ac32	0.36	10000	380.50
ac33	0.39	15000	412.23
ac34	0.44	20000	448.51
ac35	0.49	25000	488.89
ac36	0.54	30000	534.96
ac37	0.61	35000	588.11
ac38	0.69	40000	658.46
ac39	0.77	45000	743.57
ac40	0.87	50000	839.77

Table 3.2 Subsonic Envelope Flight Conditions

Points	Mach No.	Altitude (feet)	Airspeed (ft/sec)
ac41	1.10	1000	1224.24
ac42	1.20	5000	1316.87
ac43	1.40	10000	1508.72
ac44	1.50	20000	1555.68
ac45	1.60	30000	1591.69
ac46	1.60	40000	1548.14
ac47	1.10	50000	1061.72
ac48	1.35	50000	1304.13
ac49	1.60	50000	1546.38

Table 3.3 Supersonic Envelope Flight Conditions

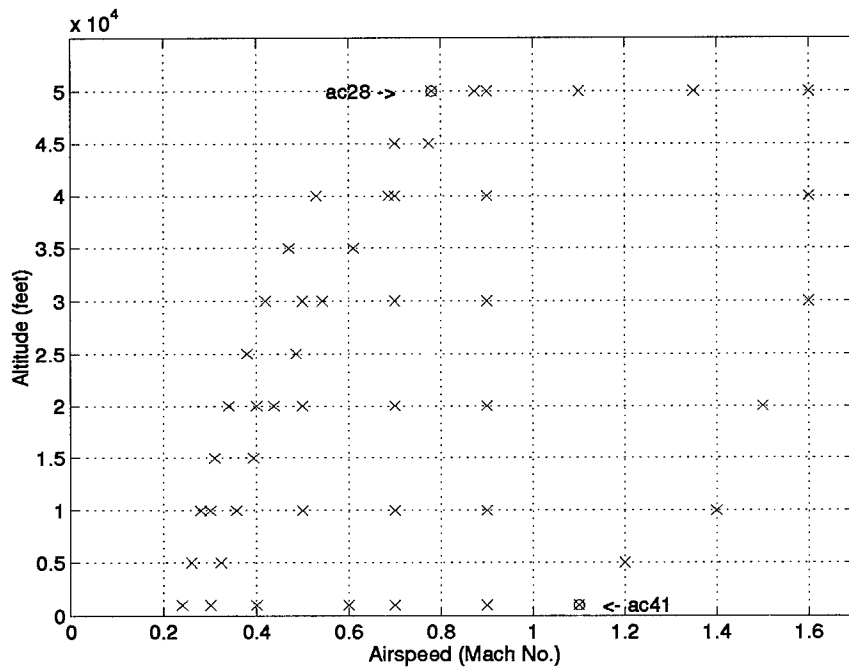


Figure 3.11 A typical modern fighter flight envelope and the flight conditions considered for $\frac{\alpha(s)}{\delta_c(s)}$

Aero Point	Plant No	Sources of Variation
ac28	1	Nominal
	2	Jm Increased by 10% from nominal
	3	Jm Decreased by 10% from nominal
	4	Dm Decreased by 10% from nominal
	5	Jm, Bm, and Dm Increased by 10% from nominal
	6	Jm, Bm, and Dm Decreased by 10% from nominal
	7	All EHA parameters Decreased by 10% from nominal
	8	All EHA parameters Increased by 10% from nominal
ac41	9	Nominal
	10	Jm Increased by 10% from nominal
	11	Jm Decreased by 10% from nominal
	12	Dm Decreased by 10% from nominal
	13	Jm, Bm, and Dm Increased by 10% from nominal
	14	Jm, Bm, and Dm Decreased by 10% from nominal
	15	All EHA parameters Decreased by 10% from nominal
	16	All EHA parameters Increased by 10% from nominal

Table 3.4 The Inner Loop Plants

are from ac28 while the template points 9 through 16 are from ac41. The largest template is at 5 rad/sec with about 22 degrees in width and 6 dB in height. All other points not forming the perimeter are then eliminated. As can be seen in Table 3.4, most of the uncertainties caused by the EHA parameter variations are due to the motor and pump variables. Hence; it is concluded that the inner loop design is dominated by the motor and the pump. This is confirmed in Chapter 4, where the pump displacement parameter is shown to cause the largest variations.

Even using the short period approximations, numerical problems exist at low frequencies. For example, the Bode plots of some plants start at 0 degree phase while others start at -360 degree phase. These two phase angles are the same. Since the short period approximation is not valid for frequencies below 0.5 rad/sec as shown in Fig. 2.5, the lower frequency limit of the bandwidth is established as 0.5 rad/sec. The upper frequency limit of the bandwidth is established as the point where the plant magnitude plot crosses -12 dB, approximately 2000 rad/sec. Hence, the poles and zeros faster than 2000 rad/sec are cancelled. The steady state gain is maintained while removing unwanted roots. Furthermore, sets of zeros and poles in close proximity are removed.

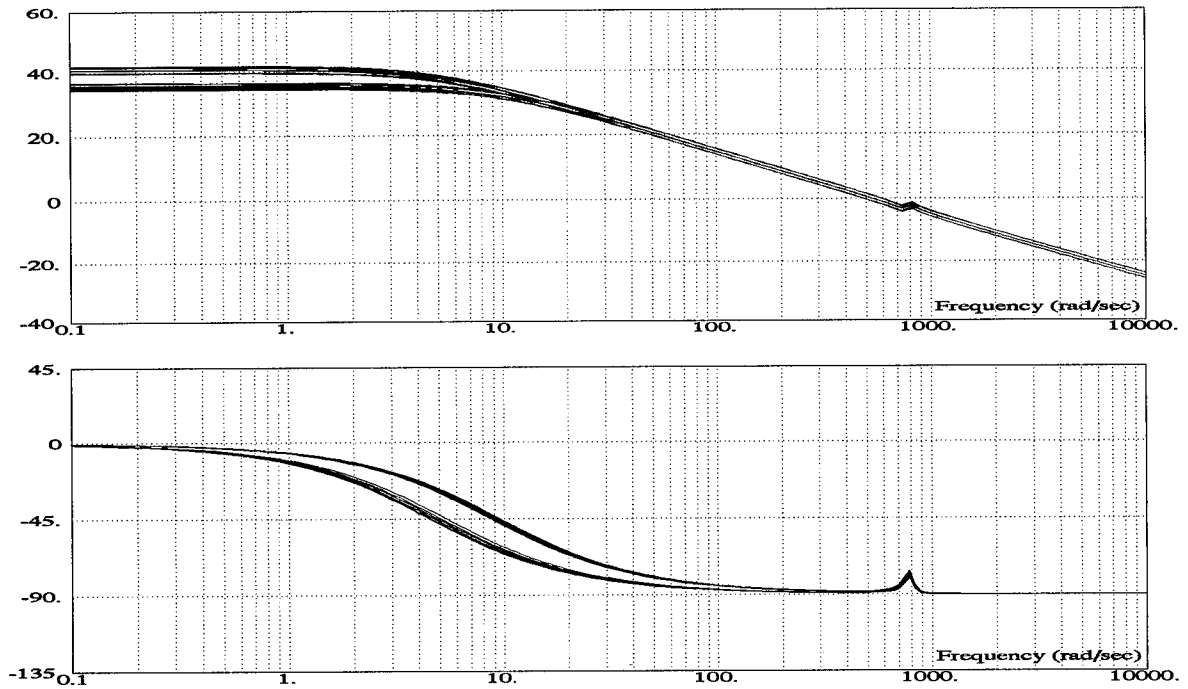


Figure 3.12 Bode Plots of the Inner Loop Plants

The coefficients of such terms in the time domain are small; hence, the effect to the system response is minor [3]. The poles and zeros are removed using the Matlab *ssdelete* function, which removes the corresponding states instead of direct pole zero cancellation. The full and reduced inner loop sets of plants are listed in Appendix B. The reduced sets of plants are used to simplify the design process; however, the full models are used for the simulations.

The Bode plot of the inner loop plants shows several distinguishing features. First, there are two distinctive bands. The upper band belongs to the flight condition ac28 and the lower band belongs to the flight condition ac41. Again, the effect of the aerodynamic load can clearly be seen to dominate the plant uncertainties. The uncertainties caused by the EHA parameter variations can be seen within the individual bands. All plants behave like a first-order system; the slope of the log magnitude is about -20 dB/dec while the phase shifts from 0 to -90 degrees, as expected. There is a set of lobes at about 800 rad/sec, caused by a pair of complex poles and zeros.

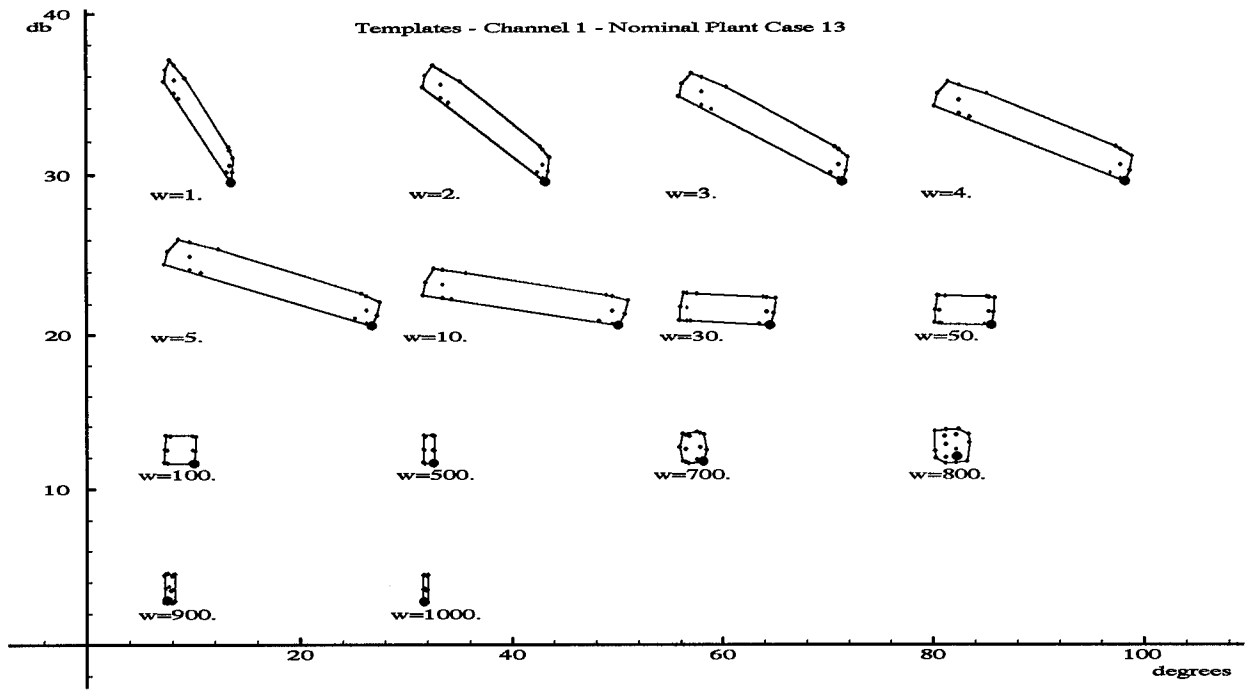


Figure 3.13 Inner Loop Plant Templates

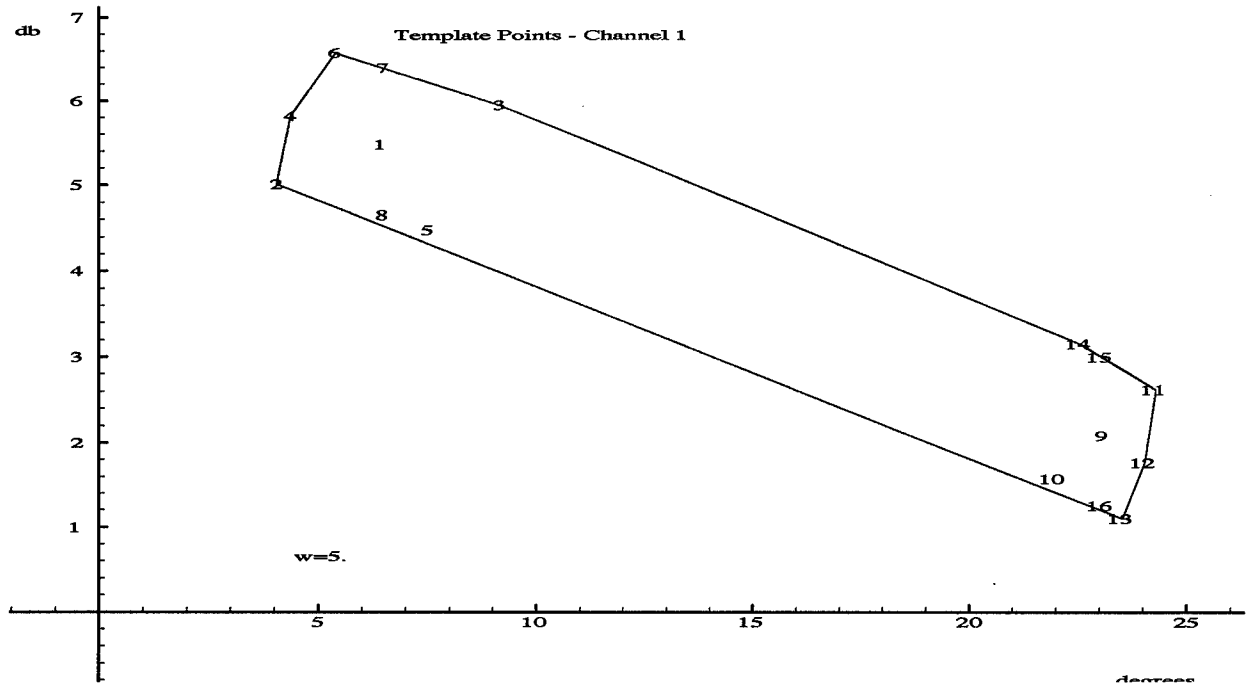


Figure 3.14 Nominal Plant Selection

3.4.3 Inner Loop Controller and Prefilter Design. Additional considerations are addressed in designing the inner loop controller. First, the inner loop compensator should be of low order in order to maintain the lowest order of the compensated system. The complex pair of poles typically used at high frequency in QFT designs to reduce the system bandwidth are not used in order to keep the system order to a minimum. A unity forward gain is sufficient to satisfy the inner loop optimal bounds, but it also requires the outer loop gain to be high. Through several design iterations, a gain of 10 is used which reduces the required outer loop gain to a desired level.

A pole at the origin is introduced to create a type 1 system, to ensure tracking of a step input. This pole also allows the nominal loop to fall between the crevices of the optimal bounds, as can be seen in Fig. 3.15. By utilizing the available plant phase information, a gain reduction of approximately 20 dB is achieved. This shows the power of the QFT design technique. If only the magnitude information is used, then the maximum DC values would form the optimal bounds. In this case, that would mean that the nominal plant transmission at 1 rad/sec must be situated at or above 74 dB. By utilizing the phase information, the nominal plant transmission at 1 rad/sec can be situated as low as 48 dB. This equates to a gain reduction of about 20. A zero is added at 15 rad/sec to bring the nominal transmission around the stability bounds. A pole at 1500 rad/sec is used to bring the nominal loop transmission back towards -180 degrees.

As mentioned previously, the inner loop prefilter is not used since tracking is not the primary purpose of the inner loop. Thus, the inner loop compensator and prefilter transfer functions are, respectively:

$$G_m(s) = \frac{1000(s + 15)}{s(s + 1500)} \quad (3.15)$$

$$F_m(s) = 1 \quad (3.16)$$

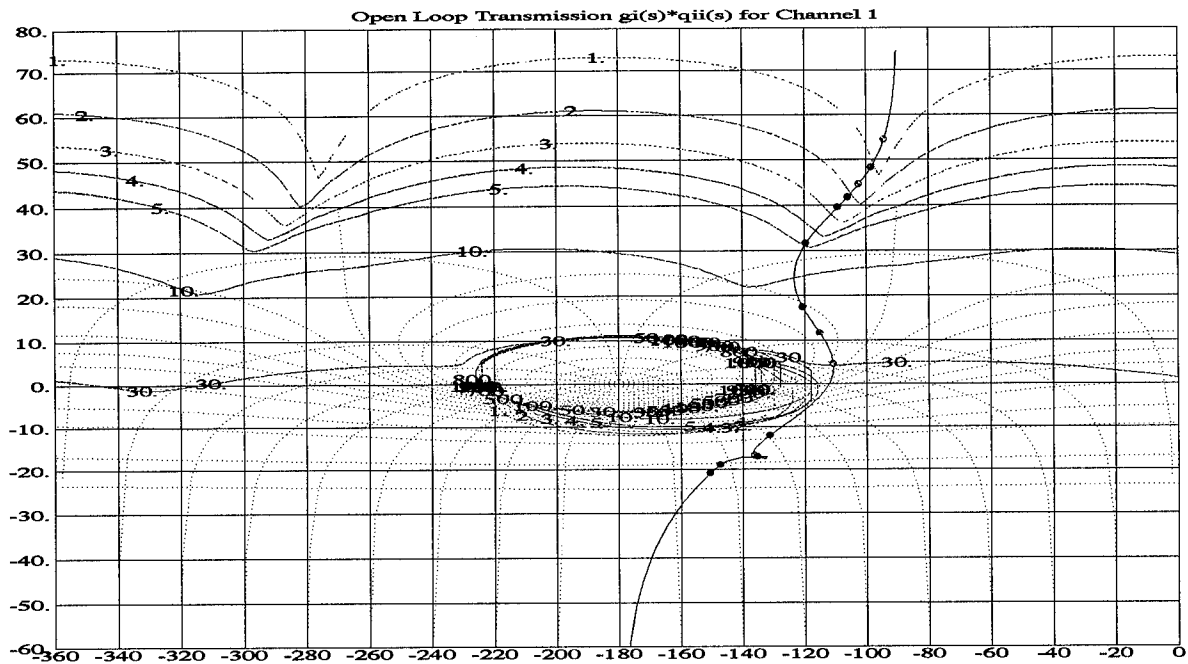


Figure 3.15 Inner Loop Compensator Design - The loop transmission is steered through the trough, as required.

3.4.4 *Inner Loop Controller Validations and Simulations.* The validation features of the QFT CAD package are used to ensure that the system with the inner loop compensator is stable. As can be seen in Fig. 3.16, all inner loop plants keep to the outside of the stability boundaries; hence, the compensator keeps all plants within the stable region of operation.

Even though the numerical problems during the design stage necessitated the model order reductions, some fidelity of the actuator model dynamics is lost in the process. To maintain the full fidelity, the full order models are used in the simulations. The design goals are shown as the set of dashed lines in Fig. 3.17. As can be seen, all plants are stable and they quickly settle (in about 0.08 sec) to the steady state value. The upper bound violations are deemed acceptable, since the system operates faster and not slower than the desired rise time. If not exceeding the upper bound is the primary concern, a prefilter could have kept the plant responses within the lower and upper bounds. However, this would have increased the order of the outer loop transfer functions.

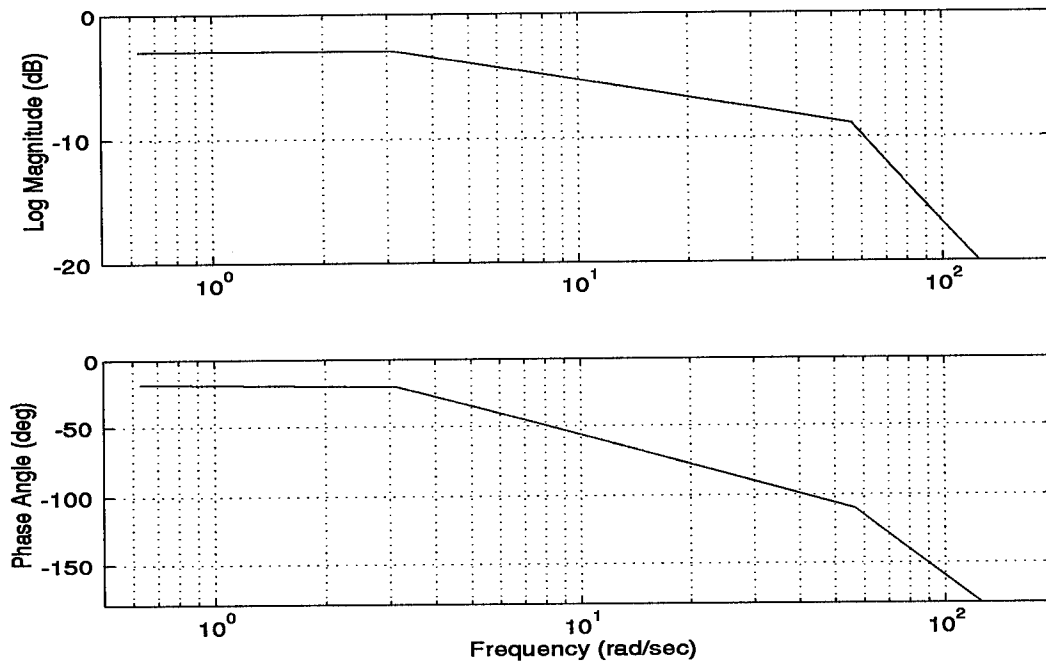


Figure 3.18 Small Signal Frequency Specification

3.5 Outer Loop Controller Design

3.5.1 Outer Loop Specifications. The purpose of the outer loop design is to enforce tracking of the given stabilator commands. The time domain specifications were not made clear in the EHA specifications. The only time domain specification was for the EHA to be able to obtain a slew rate of 6.7 in/sec under no load condition [16]. This data alone can not be used to establish the lower and upper tracking bounds. Another point of reference is required to establish the tracking bounds. However, the EHA specification clearly states the frequency specifications. The frequency specification is shown in Fig. 3.18, where the solid lines specify the minimum allowable values [16]. In order to meet the frequency specifications, the tracking bounds are chosen such that their phase characteristics are within specifications.

A common representation of aircraft actuator models is of fourth-order with the dominant pole located at about -20 [7]. This point of reference is used to build the upper and lower tracking bounds. Initially, the upper tracking bound model is formed from a simple first-order system with

the pole at -25, while the lower tracking bound is formed from a second-order system with the poles at -10 and -20. These bounds are adequate in meeting the time domain specifications. However, the bounds are not adequate in meeting the frequency specifications. By adding additional poles and zeros far out in the left plane and moving the dominant pole around, the frequency specification can be met without excessively impacting the time domain behavior of the upper tracking bound. The consideration of the frequency specifications is discussed in detail in Chapter 6. The resulting tracking bounds are defined by the following equations:

$$T_{ru}(s) = \frac{270(s+50)(s+400)}{(s+45)(s+60)(s+2000)} \quad (3.17)$$

$$T_{rl}(s) = \frac{200}{(s+10)(s+20)} \quad (3.18)$$

There are two possible sources of disturbances, internal and external, as shown in Fig. 3.19. The internal disturbance is caused by the cross-coupling effects between the states. The external disturbance is caused by external unmodelled forces. It is reasonable to conclude that the actuator is quite stiff from the load end; hence, the external disturbance can be ignored (i.e., $d_2(t) = 0$). The EHA should provide adequate internal disturbance (i.e., $d_1(t) = u_{-1}(t)$) rejection by attenuating the disturbance input by -20 dB or more. A pole is added to the disturbance model ensuring improvements in high frequency rejection characteristics. The final form of the disturbance rejection model is shown in Eq. (3.19).

$$T_D(s) = \frac{5}{s+50} \quad (3.19)$$

3.5.2 Set of Plants in the Outer Loop. As in the inner loop design, the flight conditions that define the perimeter of the plant templates are ac28 and ac41, at the opposite end of the envelope. As can be seen in Figs. 3.20 and 3.21, the outer loop templates are quite small (see Section 3.4). Only 10 points are needed to define the perimeter of the templates. Again, the motor and

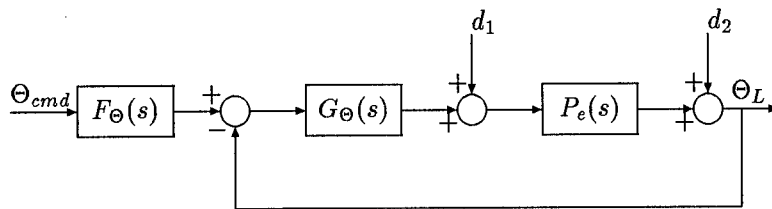


Figure 3.19 Disturbances in the QFT Feedback Structure

pump parameters are the major sources of plant variations. Since the short period approximation is not valid for frequencies below 0.5 rad/sec as shown in Fig. 2.5, the lower frequency limit of the bandwidth is established as 0.5 rad/sec. The upper frequency limit of the bandwidth is established as 200 rad/sec, ten times the aircraft bandwidth. Hence, the poles and zeros faster than 200 rad/sec are eliminated. The steady state gain is maintained while removing unwanted roots. Due to the finite numerical accuracies of computers, an outer loop pole varies in the range of -0.001 to -0.004. To eliminate this adverse effect of numerical computation methods, the outer loop pole well below the bandwidth frequency is set as a pole at the origin. The reduced sets of plants are used to simplify the design process; however, the full models are used for the simulations. All outer loop plants, listed in full and reduced forms in Appendix B, are minimum-phase.

3.5.3 Outer Loop Controller and Prefilter Design. A DC gain of 60 is required to bring the nominal open loop transmission above the respective optimal bounds shown in Fig. 3.22. A pole at 8.5 rad/sec and zero at 14.5 rad/sec are added to meet the optimal and stability bounds. A pair of complex poles are added at $-200 \pm j200$ to swing the transmission line across the -180 degree phase line. Figure 3.23 shows that the nominal loop transmission satisfies all the required bounds. The resulting compensator transfer function is shown in Eq. (3.20).

Aero Point	Plant No	Sources of Variation
ac28	1	Dm Increased by 10% from nominal
	2	Jm, Bm, and Dm Increased by 10% from nominal
	3	Jm, Bm, and Dm Decreased by 10% from nominal
	4	All EHA parameters Decreased by 10% from nominal
	5	All EHA parameters Increased by 10% from nominal
ac41	6	Jm, Bm, and Dm Increased by 10% from nominal
	7	Jm, Bm, and Dm Decreased by 10% from nominal
	8	Dm Increased by 10% from nominal
	9	All EHA parameters Decreased by 10% from nominal
	10	All EHA parameters Increased by 10% from nominal

Table 3.5 The Outer Loop Plants

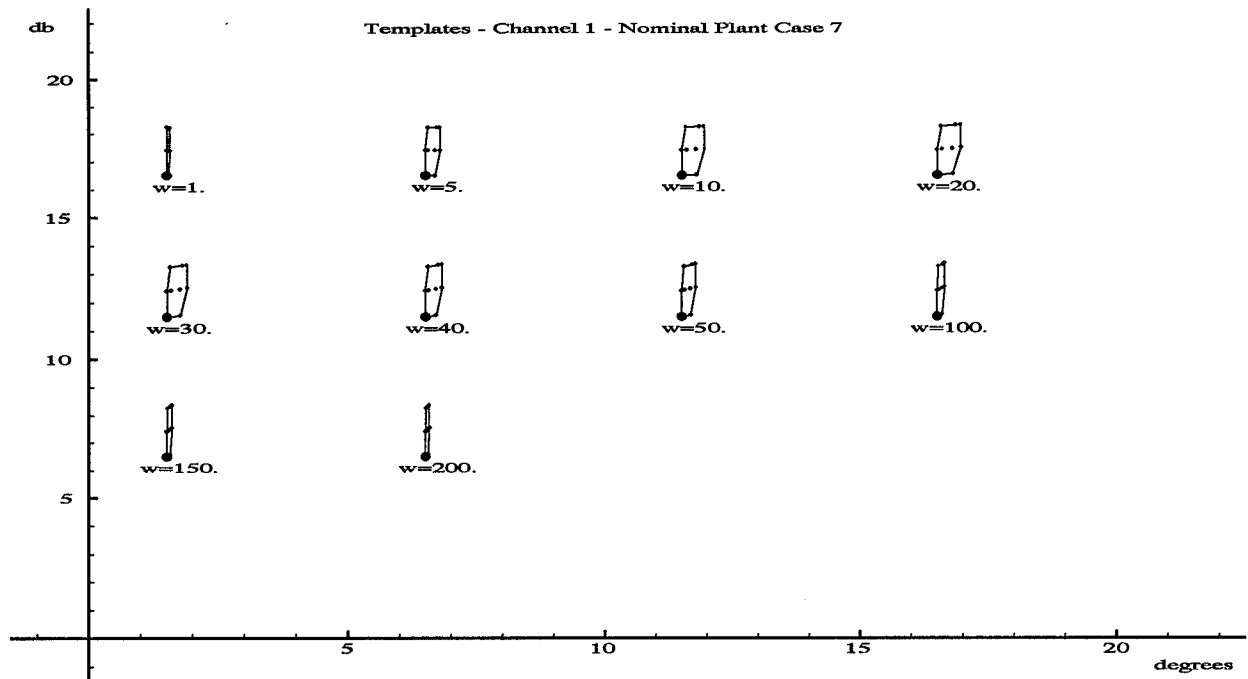


Figure 3.20 Outer Loop Plant Templates

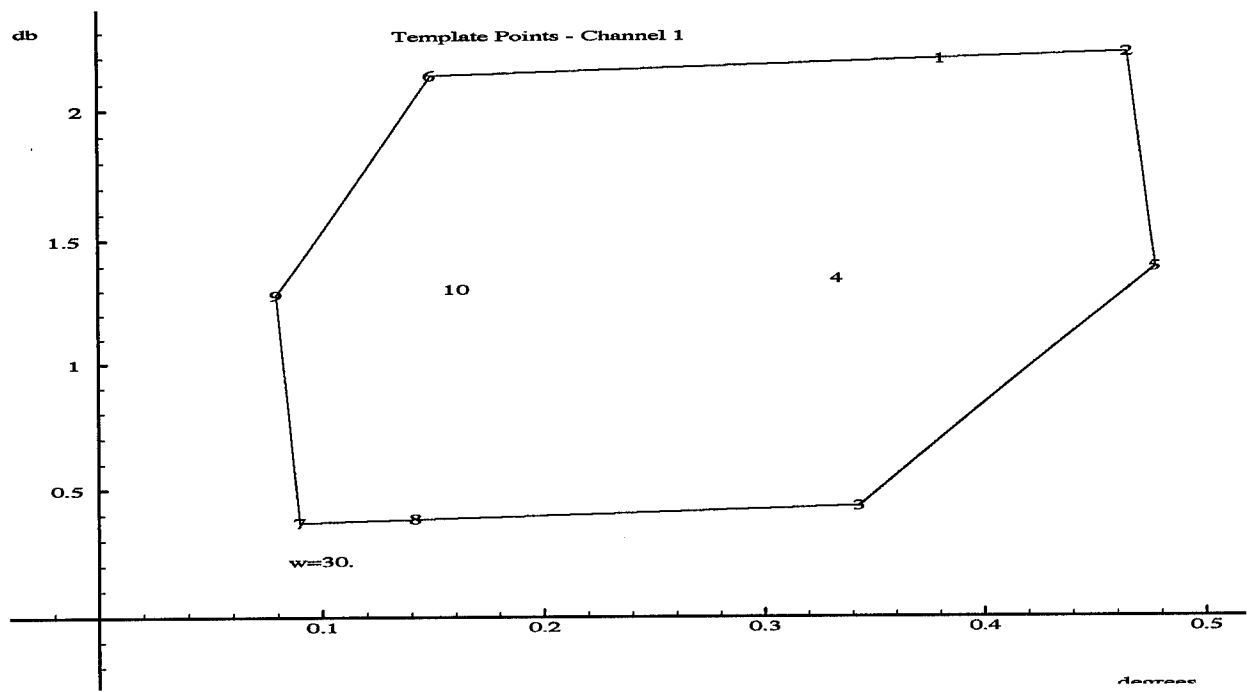


Figure 3.21 Outer Loop Nominal Plant Selection

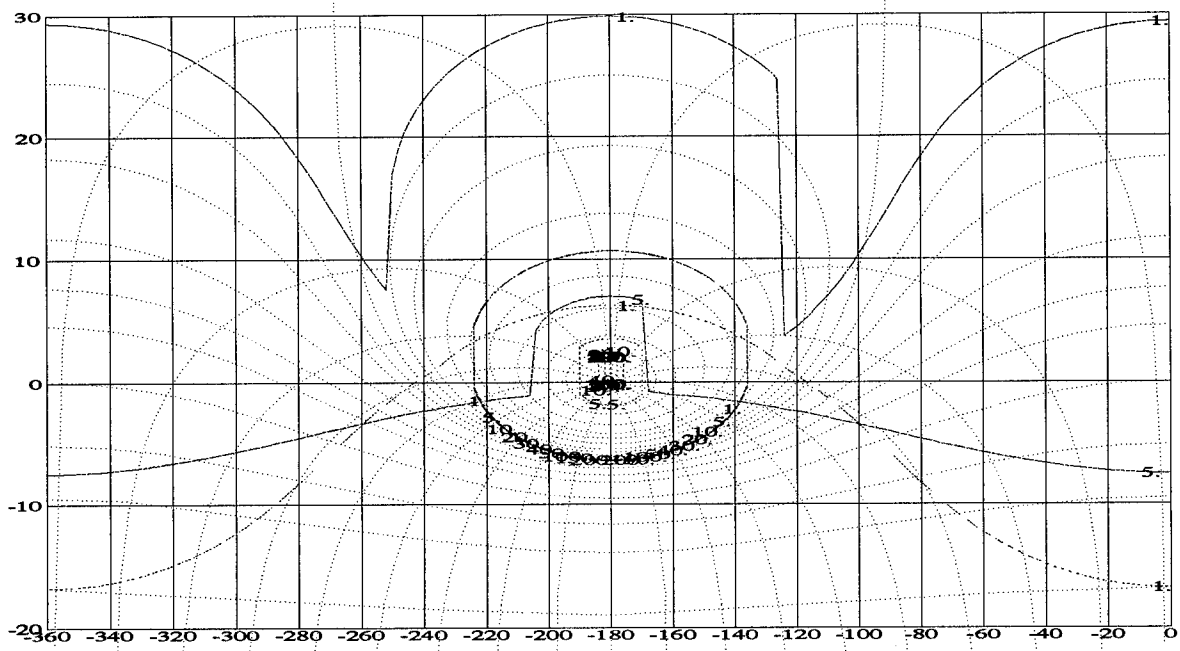


Figure 3.22 Outer Loop Bounds

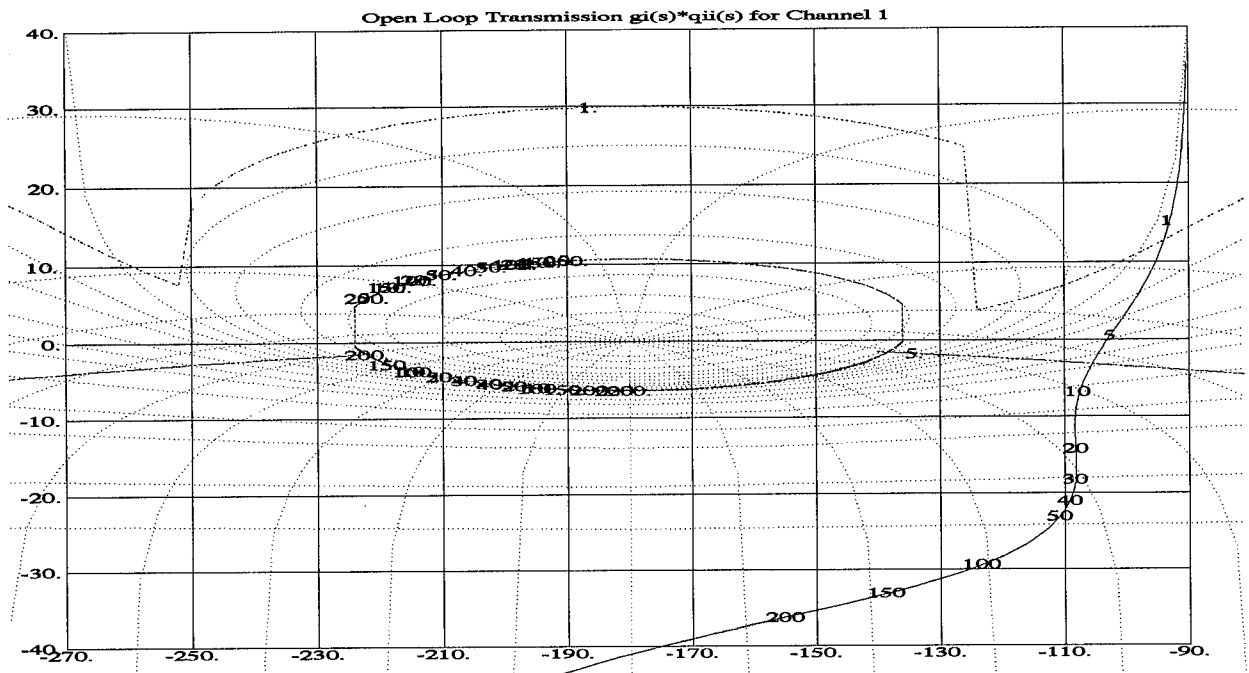


Figure 3.23 Outer Loop Compensator Design

$$G_{\Theta}(s) = \frac{2.813793 * 10^6 (s + 14.5)}{(s + 8.5)(s^2 + 400s + 80000)} \quad (3.20)$$

The prefilter must not attenuate the given input signal; hence, the DC gain of the prefilter must equal to 1 [3]. A prefilter with third order zeros over third order poles is required to satisfy the bounds. A zero and two poles at high frequency are required to satisfy the frequency specifications, magnitude as well as phase. The resulting prefilter transfer function is shown in Eq. (3.21). Since the existing QFT prefilter design procedure emphasizes only the magnitude and not phase, several iterations are required to meet both the magnitude and phase specifications. This notion is discussed further in detail in Chapter 6.

$$F_{\Theta}(s) = \frac{(s + 3.6)(s + 8)(s + 4444.4)}{(s + 3.2)(s + 200)(s + 200)} \quad (3.21)$$

3.5.4 Outer Loop Design Validations and Simulations. Figures 3.25 to 3.27 show the results of the QFT CAD simulations of the outer loop compensator and prefilter design. As shown

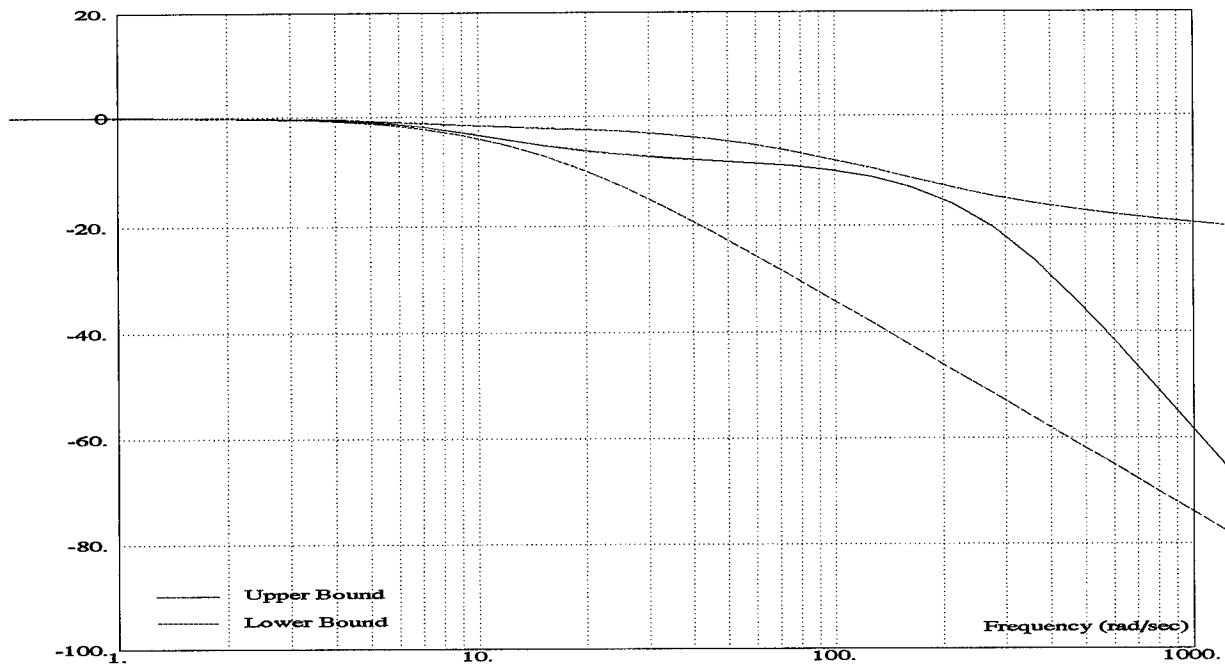


Figure 3.24 Outer Loop Prefilter Design

in Fig. 3.25, all plants stay clear of the U-contour; hence, the stability of all plants are guaranteed. As shown in Fig. 3.26, the disturbance signals are rejected at about -35 dB attenuation levels, well in excess of the -20 dB attenuation specification. The higher frequency disturbance signals are attenuated even more. As shown in Fig. 3.27, all plants stay between the upper and lower tracking bounds.

The time and frequency responses are simulated using the Matlab Simulink block models, not the reduced order transfer functions. Figures 3.28 to 3.31 show the system response in both the time and frequency domains. As expected, Fig. 3.28 shows that the disturbance input is rejected at levels well below the specification. Figures 3.29 and 3.30 show the time domain response of the system to a unit step input. The system shows a slight oscillation, primarily due to the pair of complex poles near the origin from the aircraft short period models. However, the rise and settling times are quite fast. All plants settle to the 98% of the final value within 0.3 seconds. The oscillations and violation of the bounds are deemed acceptable, since the magnitude of the

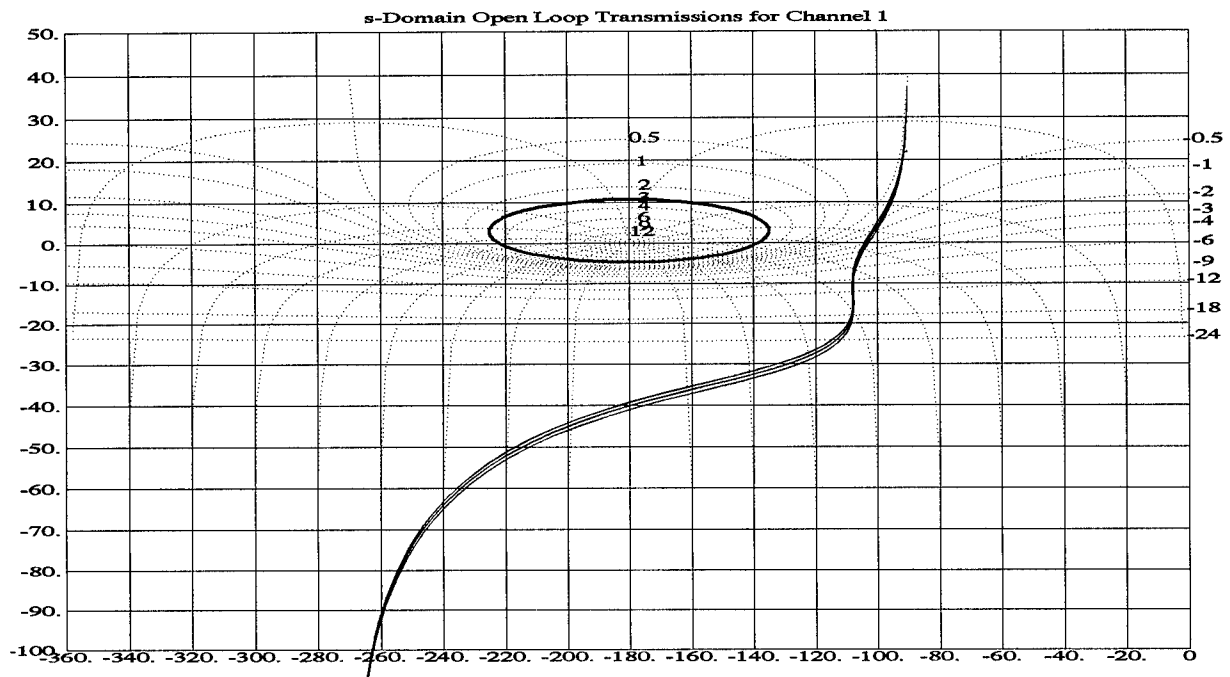


Figure 3.25 Outer Loop Stability Simulation

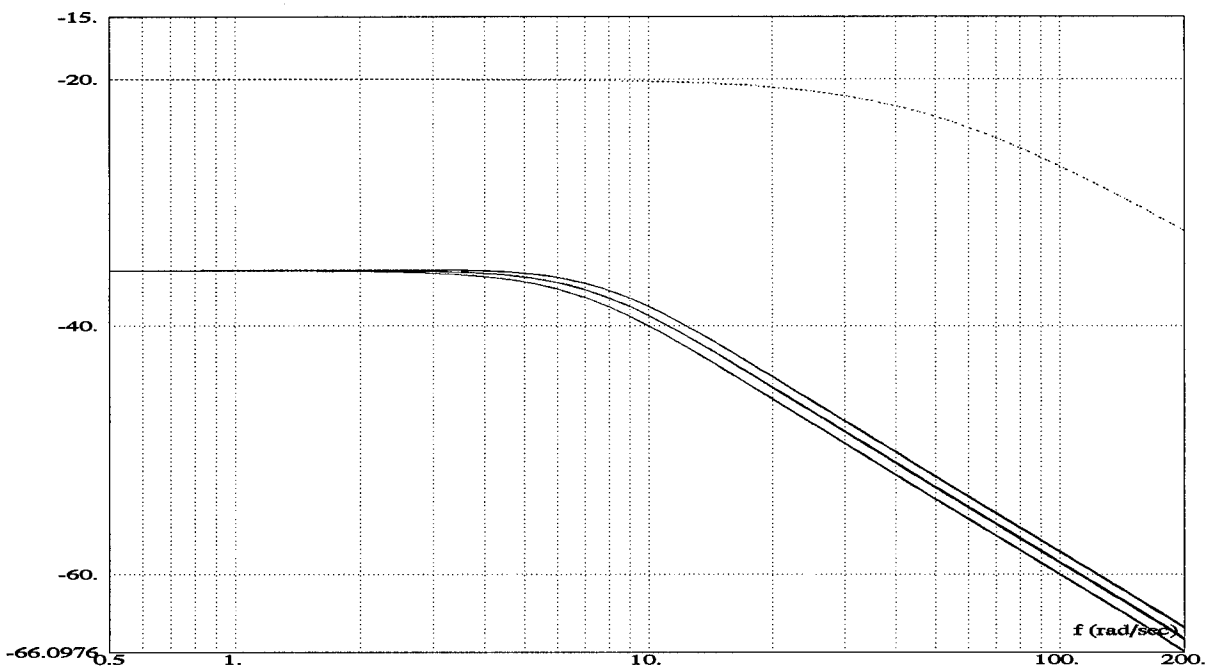


Figure 3.26 Outer Loop Disturbance Rejection Simulation

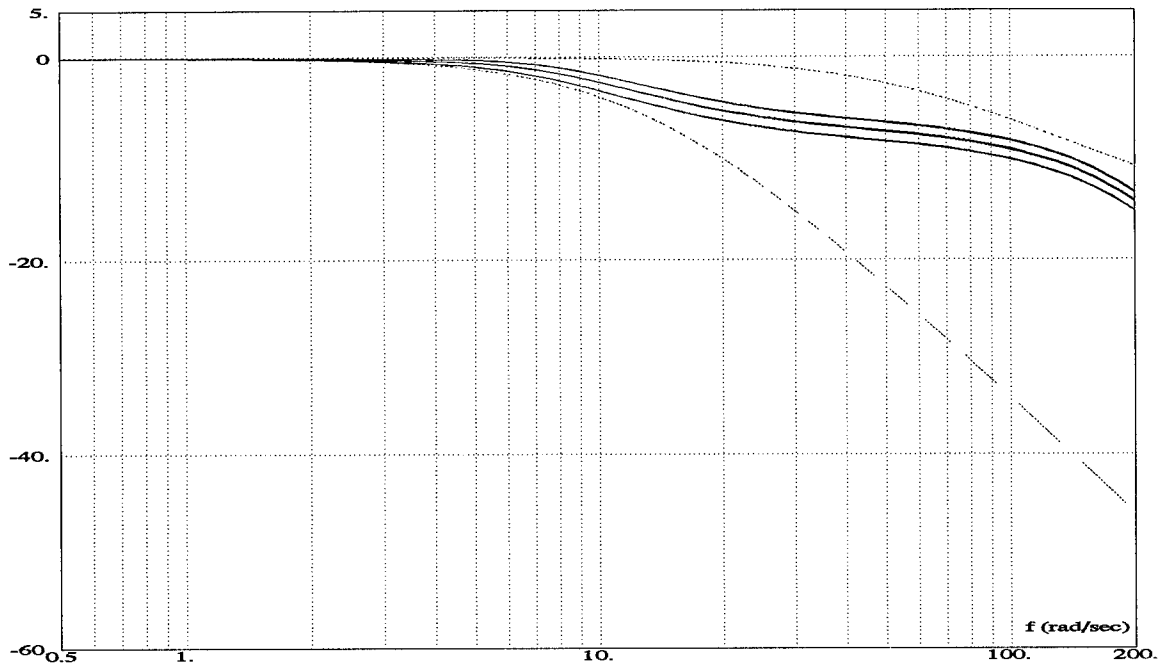


Figure 3.27 Outer Loop Tracking Simulation

violations are relatively small.

The small-signal frequency responses are obtained by commanding the individual plants with a sinusoid input having a magnitude of 0.5% of the maximum piston travel and frequencies varying from 0.5 rad/sec to 200 rad/sec. The peaks of both the reference and the output signals are first detected, then the attenuation and phase between the peaks are computed. By repeating the process over a predefined set of frequencies, a set of 'Bode plot' data is derived. The dashed lines in both the magnitude and phase plots are the minimum values allowed in the EHA specifications. As can be seen in Fig. 3.31, all plants stay well above the minimum boundaries.

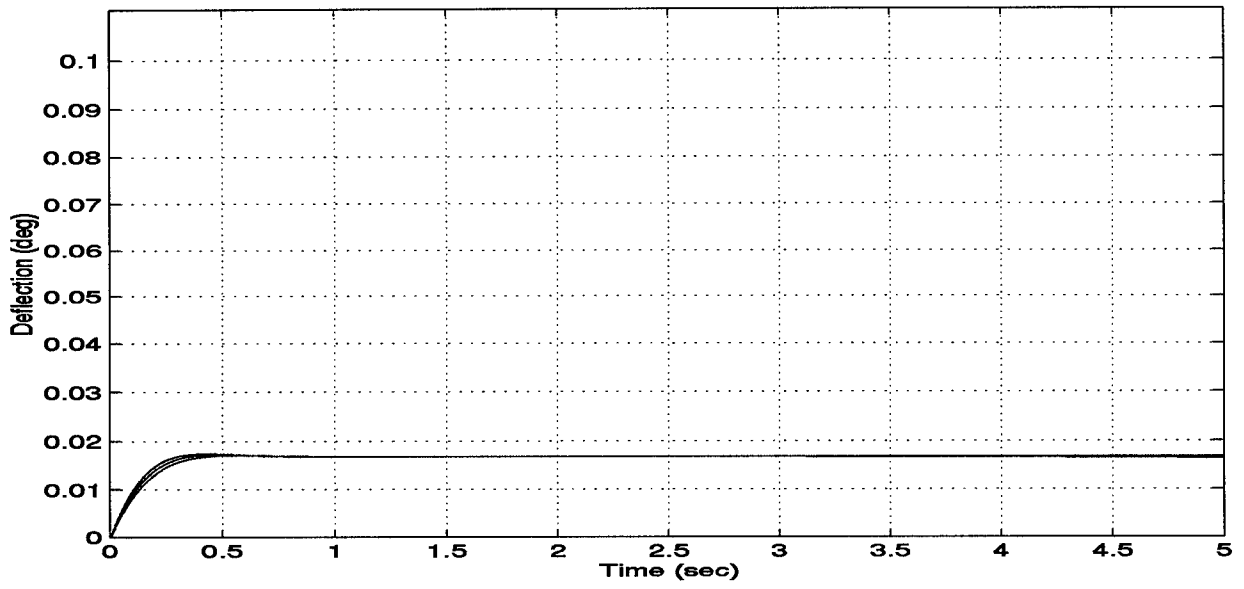


Figure 3.28 Outer Loop Time Domain Unit Step Disturbance Response Simulation

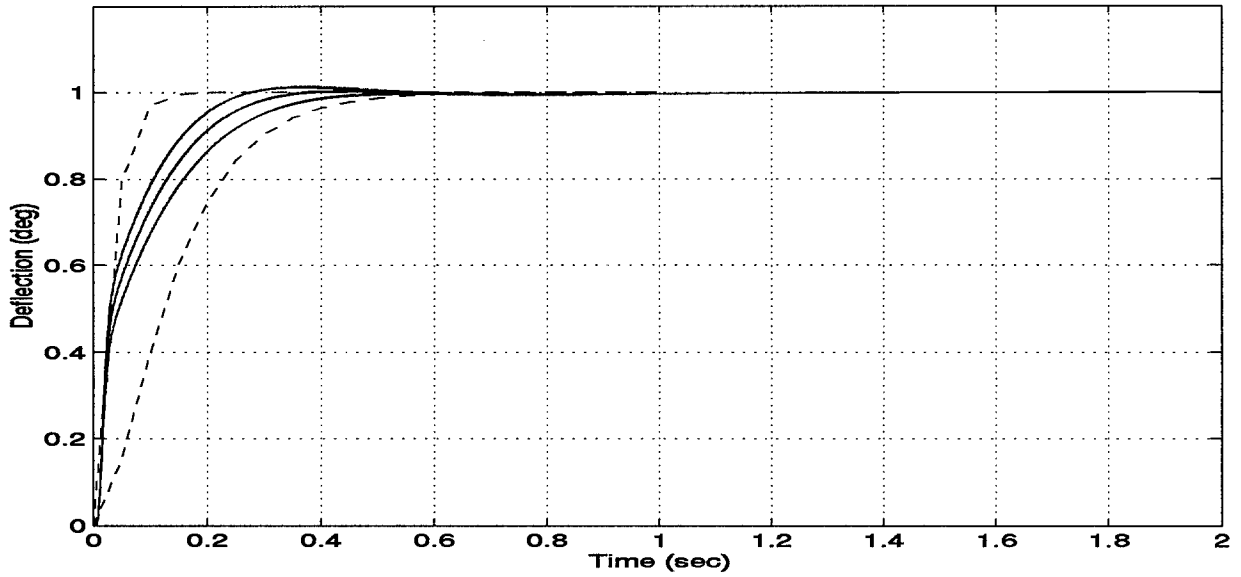


Figure 3.29 Outer Loop Time Domain Unit Step Input Response Simulation

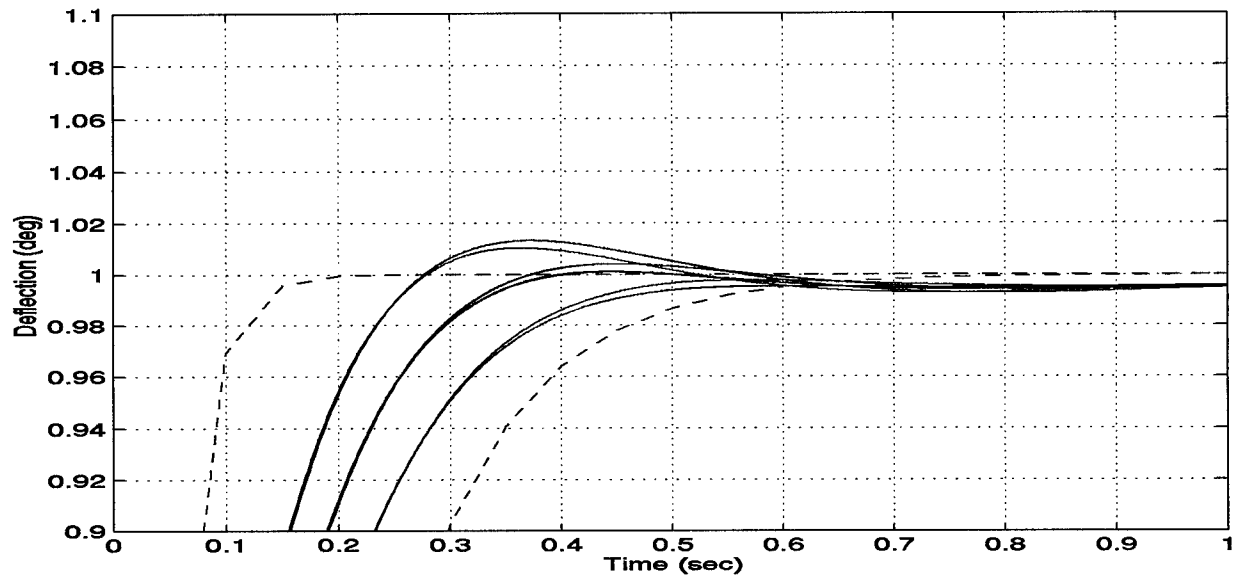


Figure 3.30 Close Up of the Outer Loop Time Domain Unit Step Input Response Simulation

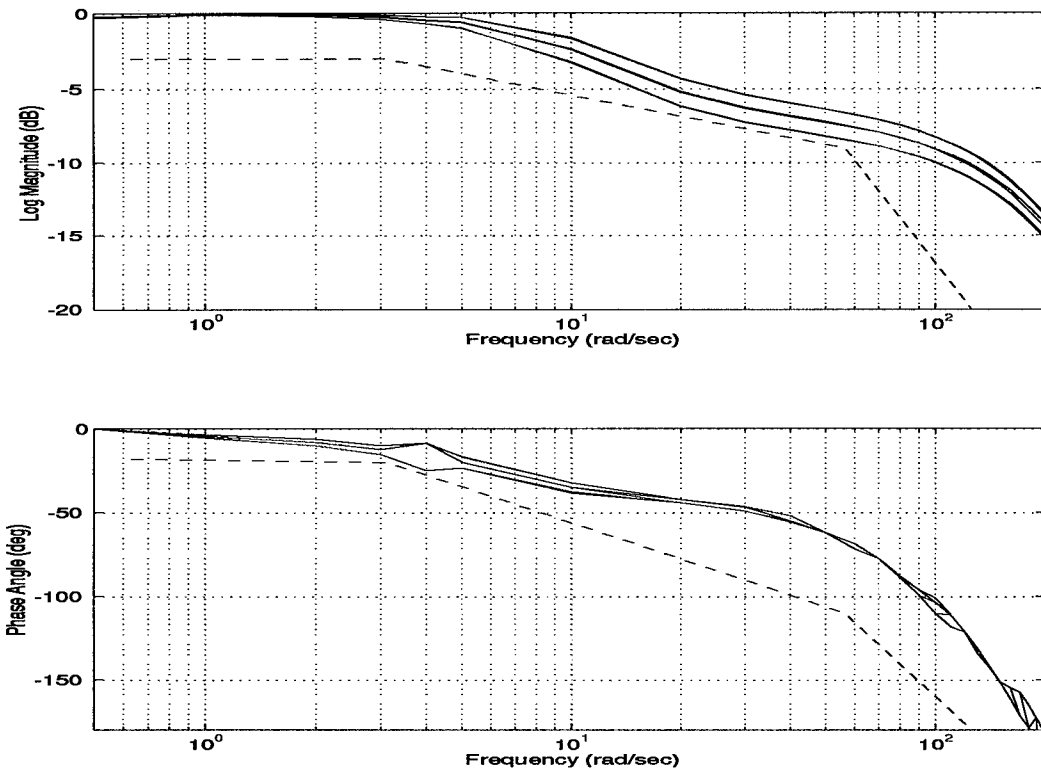


Figure 3.31 Outer Loop Small-Signal Frequency Domain Sinusoidal Input Response Simulation

IV. Sensitivity Analysis

4.1 System Sensitivity

The sensitivity function, a measure of the output variations due to parameter variations, is defined by

$$S_{\delta}^M = \frac{\delta}{M} \left(\frac{dM}{d\delta} \right) \quad (4.1)$$

i.e., the sensitivity function yields the ratio of the incremental amount of output change to the incremental parameter change [3]. To study the sensitivity of the QFT design, the sensitivity functions, of the QFT controller versus a reference controller created using standard design methods, are compared. A basic feedback control system with two nested unity gain loops (i.e., the controllers and prefilters set to unity) is also considered. However, this control system proved to be too slow, with the settling time of twenty seconds or more making the relative comparison difficult. Thus, this model would not provide any useful comparison. The high gain EHA controller normally operates in the saturation region; hence, the linear model is not a reasonable predictor of its actual performance. The linear simulation results are skewed and overly optimistic. Hence, the sensitivity comparison between the linear model of the existing EHA controller design versus the QFT controller is not a strictly valid one. But certain aspects of the high gain design that are common to linear and non-linear operations can be compared. This chapter consists of three sections: sensitivity analysis in the time domain, sensitivity analysis in the frequency domain, and sensitivity to sensor noise.

There are two ways of computing the sensitivity of a system: analytically or numerically. The sensitivity function is computed analytically by symbolically computing the partial derivatives of the actuator transfer function and substituting the nominal values in for the coefficients. Due to the complex nature of the actuator control system, this is a very difficult task to accomplish analytically. A symbolic programming language can be used to obtain the transfer function of the actuator system. The symbolic expressions of the bare actuator transfer function is too complex to even consider extracting useful information from it. The addition of the two control loops

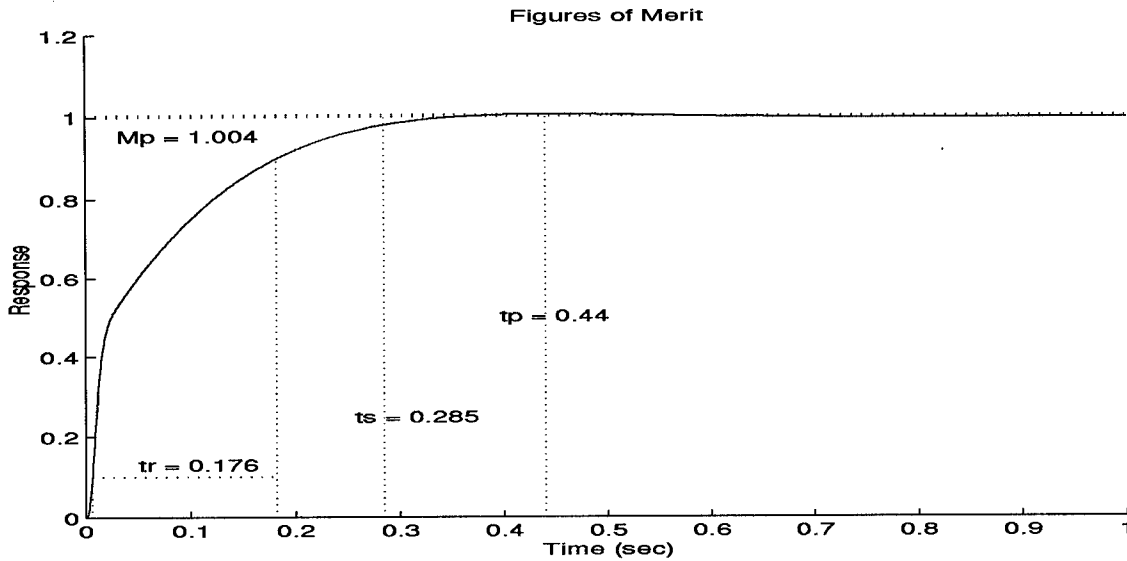


Figure 4.1 The Nominal Plant Time Domain Figures of Merit for Unit Step Input

would further complicate the problem. The system sensitivity can be computed numerically by first varying the individual parameters, then comparing the output against the nominal response. The nominal plant, used as a reference point of comparison, represents the mean flight condition (i.e., ac21 - Mach 0.78 and 30,000 ft altitude) with nominal EHA parameters.

4.2 Time Domain Sensitivity Analysis

For the time domain sensitivity analysis, four responses to unit step input are compared. The rise time t_r denotes the time for the output response, on its initial rise, to change from 10 to 90 percent of the steady state value. The peak time t_p denotes the time for the output response to reach the maximum value. The settling time t_s denotes the time which the output response settles within $\pm 2\%$ of the final value [3]. The graphical representation of these four parameters is shown in Fig. 4.1.

As Table 4.1 shows, changes in the pump displacement parameter D_m for the QFT design cause the most variation to the output figures of merit. The numbers enclosed in the parenthesis denote the change from the nominal response in percent. A ten percent change in D_m causes twenty

Plant	tr (sec)	tp (sec)	ts (sec)
Nominal	0.176	0.440	0.285
-10% J_m	0.177 (0.57%)	0.441 (0.23%)	0.285 (0.00%)
+10% J_m	0.178 (1.14%)	0.440 (0.00%)	0.284 (-0.35%)
-10% B_m	0.179 (1.70%)	0.446 (1.36%)	0.290 (1.75%)
+10% B_m	0.176 (0.00%)	0.440 (0.00%)	0.284 (-0.35%)
-10% D_m	0.218 (23.86%)	0.561 (27.50%)	0.363 (27.37%)
+10% D_m	0.144 (-18.18%)	0.364 (-17.27%)	0.226 (-20.70%)
-10% K_s	0.176 (0.00%)	0.440 (0.00%)	0.285 (0.00%)
+10% K_s	0.176 (0.00%)	0.440 (0.00%)	0.285 (0.00%)
-10% C_t	0.179 (1.70%)	0.445 (1.14%)	0.290 (1.75%)
+10% C_t	0.179 (1.70%)	0.445 (1.14%)	0.290 (1.75%)
-10% M_p	0.179 (1.70%)	0.446 (1.36%)	0.290 (1.75%)
+10% M_p	0.177 (0.57%)	0.441 (0.23%)	0.285 (0.00%)
-10% B_p	0.177 (0.57%)	0.441 (0.23%)	0.285 (0.00%)
+10% B_p	0.176 (0.00%)	0.440 (0.00%)	0.285 (0.00%)
-10% J_l	0.178 (1.14%)	0.445 (1.14%)	0.289 (1.40%)
+10% J_l	0.179 (1.70%)	0.446 (1.36%)	0.290 (1.75%)
-10% B_l	0.175 (-0.57%)	0.435 (-1.14%)	0.280 (-1.75%)
+10% B_l	0.179 (1.70%)	0.445 (1.14%)	0.290 (1.75%)
$+\bar{q}$	0.177 (0.57%)	0.441 (0.23%)	0.285 (0.00%)
$-\bar{q}$	0.177 (0.57%)	0.438 (-0.45%)	0.283 (-0.70%)

Table 4.1 Time Domain Parametric Sensitivity of QFT Design. The numbers enclosed in the parenthesis denote the change from the nominal response in percent.

percent or more changes to the system figures of merit. All other parameters cause negligible change to the system's figures of merit. Hence, it can be concluded that the actuator system, including the control structure, is most sensitive to the variations of the pump displacement parameter in the time domain. The performance of the actuator with the QFT controller is quite insensitive to variations in all other parameters.

As Table 4.2 shows, the high gain actuator control system is also robust, more so than the QFT design for the most part. The nominal plant figures of merit are about half of the QFT design. The changes in figures of merit due to the pump displacement parameter variations are about half of the QFT design. Both the robustness and better figures of merit are as expected in a high gain design. The QFT design achieves robustness through the use of minimum gain. Gains above this minimum value will only make the system more susceptible to sensor noise than

Plant	tr (sec)	tp (sec)	ts (sec)
Nominal	0.086	0.445	0.154
-10% D_m	0.095 (10.47%)	0.490 (10.11%)	0.172 (11.69%)
+10% D_m	0.077 (-10.47%)	0.407 (-8.54%)	0.140 (-9.09%)
$+\bar{q}$	0.086 (0.00%)	0.481 (8.09%)	0.153 (-0.65%)
$-\bar{q}$	0.085 (-1.16%)	0.931 (109.21%)	0.150 (-2.60%)

Table 4.2 Time Domain Parametric Sensitivity of High Gain Design. The numbers enclosed in the parenthesis denote the change from the nominal response in percent.

is absolutely necessary to meet a given set of specifications [9]. The shortfall of a high gain design is its sensitivity to sensor noise. The high gain design exhibits more deviations when handling the aerodynamic load variations. This may primarily be due to the fact that the aerodynamic load is explicitly considered in this QFT design process while it was ignored in the high gain design. Thus the QFT design better accommodates the unavoidable aerodynamic load variations.

4.3 Frequency Domain Sensitivity Analysis

For the frequency domain sensitivity analysis, two responses are compared. The attenuation, given in decibels, is the logarithmic difference between the magnitude of the input signal versus the output response. The phase lag, given in degrees, is the amount of phase the output response lags the input signal. Obviously, the attenuation and phase lag are frequency dependent quantities. Figure 4.2 shows the frequency domain behavior of the nominal plant within the system bandwidth.

Tables 4.3 and 4.4 are the frequency domain responses due to actuator control system's parametric variations. Table 4.3 shows the attenuation response, while Table 4.4 shows the phase response. The numbers enclosed in the parenthesis denote the change from the nominal response in percent. As Tables 4.3 and 4.4 show, the changes in the pump displacement parameter D_m for the QFT design cause the most variation to the output attenuation and phase lag. All other parameters cause negligible change to the output frequency responses. Hence, it can be concluded that the actuator system, including the control structure, is most sensitive to the variations of the pump displacement parameter in the frequency domain as well. In the frequency range interest of

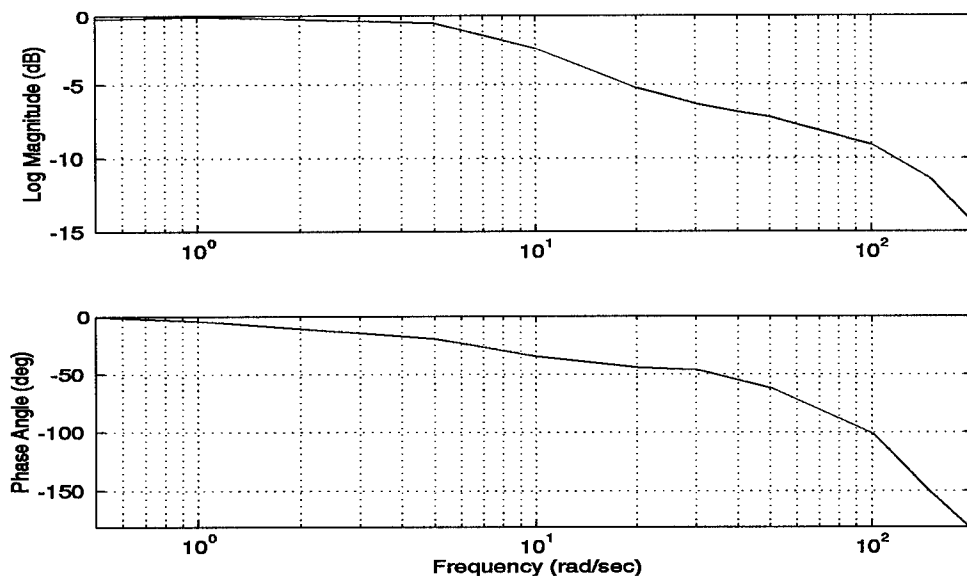


Figure 4.2 The Frequency Response Plot of the Nominal Plant

1 to 10 rad/sec, the variations in the aerodynamic loads cause noticeable changes. The primary cause of the low frequency variations may be due to the fact that the airframe's poles are relatively slow, in the bandwidth of 1 to 20 rad/sec. The aircraft poles play a role in the actuator low frequency dynamics. The actuator with the QFT controller is quite insensitive to variations in all other parameters.

Figure 4.3 shows the actuator sensitivity to the variations in the pump displacement parameter. The frequency responses due to a +10% change are shown as dotted lines, while the responses due to a -10% parameter change are shown as dashed lines. The solid lines are the nominal plant responses. Figures 4.3(a) and 4.3(b) are the attenuation and phase responses, respectively. Figures 4.3(c) and 4.3(d) are the attenuation and phase deviations, respectively, from the nominal response in percent.

4.4 Sensor Noise Effects

Most feedback control systems require sensors to feed back desired observable states. Two observable states, the pump motor's angular rate and the piston position, are used for the synthesis

Frequency (rad/sec)	1	5	10	20	30	50	100	150	200
Nominal	-0.05	-0.54	-2.40	-5.21	-6.29	-7.23	-9.08	-11.41	-14.36
-10 J_m	-0.05	-0.54 (0.4)	-2.41 (0.6)	-5.24 (0.6)	-6.32 (0.5)	-7.26 (0.5)	-9.06 (-0.2)	-11.37 (-0.4)	-14.19 (-1.1)
+10 J_m	-0.05	-0.53 (-0.4)	-2.38 (-0.6)	-5.18 (-0.6)	-6.25 (-0.6)	-7.20 (-0.4)	-9.09 (0.1)	-11.49 (0.7)	-14.51 (1.0)
-10 B_m	-0.05 (0.1)	-0.54 (0.2)	-2.40	-5.20 (-0.1)	-6.28 (-0.1)	-7.22 (-0.1)	-9.07 (-0.1)	-11.41 (-0.1)	-14.35
+10 B_m	-0.05 (-0.1)	-0.54 (-0.2)	-2.40	-5.21 (0.1)	-6.29 (0.1)	-7.24 (0.1)	-9.08 (0.1)	-11.42 (0.1)	-14.36
-10 D_m	-0.07 (33.7)	-0.93 (74.0)	-3.24 (35.2)	-6.15 (18.2)	-7.23 (15.0)	-8.17 (13.0)	-10.00 (10.1)	-12.34 (8.1)	-15.27 (6.4)
+10 D_m	-0.04 (-23.8)	-0.23 (-57.3)	-1.66 (-30.7)	-4.35 (-16.4)	-5.43 (-13.6)	-6.38 (-11.7)	-8.24 (-9.2)	-10.58 (-7.3)	-13.54 (-5.7)
-10 K_s	-0.05 (-0.1)	-0.54 (0.1)	-2.40	-5.21	-6.29	-7.23 (0.1)	-9.09 (0.2)	-11.45 (0.3)	-14.42 (0.5)
+10 K_s	-0.05 (0.1)	-0.54 (-0.1)	-2.40	-5.21	-6.29	-7.22 (-0.1)	-9.06 (-0.2)	-11.39 (-0.2)	-14.30 (-0.4)
-10 C_t	-0.05 (-0.4)	-0.54 (-0.1)	-2.40	-5.21	-6.29	-7.23	-9.08	-11.41	-14.36
+10 C_t	-0.05 (0.4)	-0.54 (0.1)	-2.40	-5.21	-6.29	-7.23	-9.08	-11.41	-14.36
-10 M_p	-0.05	-0.54	-2.40	-5.21	-6.29	-7.23	-9.08	-11.41	-14.36
+10 M_p	-0.05	-0.54	-2.40	-5.21	-6.29	-7.23	-9.08	-11.41	-14.36
-10 B_p	-0.05	-0.54	-2.40	-5.21	-6.29	-7.23	-9.08	-11.41	-14.35
+10 B_p	-0.05	-0.54	-2.40	-5.21	-6.29	-7.23	-9.08	-11.41	-14.36
-10 J_l	-0.05	-0.54	-2.40	-5.21	-6.29	-7.23 (0.1)	-9.09 (0.2)	-11.44 (0.3)	-14.42 (0.4)
+10 J_l	-0.05	-0.54	-2.40	-5.21	-6.28	-7.22 (-0.1)	-9.06 (-0.2)	-11.39 (-0.3)	-14.30 (-0.4)
-10 B_l	-0.05 (0.1)	-0.54 (0.1)	-2.40	-5.21	-6.28	-7.23	-9.07	-11.41	-14.35
+10 B_l	-0.05 (-0.1)	-0.54 (-0.1)	-2.40	-5.21	-6.29	-7.23	-9.08	-11.42	-14.36
high \bar{q}	-0.05 (-4.3)	-0.54	-2.40	-5.21	-6.29	-7.23	-9.06 (-0.2)	-11.42	-14.37 (0.1)
low \bar{q}	-0.05 (6.1)	-0.57 (6.5)	-2.33 (-2.9)	-5.18 (-0.5)	-6.27 (-0.3)	-7.22 (-0.2)	-9.07 (-0.1)	-11.40 (-0.1)	-14.35 (-0.1)

Table 4.3 Frequency Domain Parameter Sensitivity - Attenuation. The numbers enclosed in the parenthesis denote the change from the nominal response in percent. No parenthesis within the block denotes zero deviation.

Frequency (rad/sec)	1	5	10	20	30	50	100	150	200
Nominal	-4.1	-19.7	-34.8	-44.0	-46.5	-62.1	-100.8	-151.3	-183.3
-10 J_m	-4.1	-19.7	-34.8	-42.2 (-4.2)	-46.5	-62.1	-100.8	-151.3	-183.3
+10 J_m	-4.1	-19.7	-34.8	-44.0	-49.2 (5.9)	-62.1	-110.0 (9.1)	-151.3	-195.0 (6.3)
-10 B_m	-4.1	-19.7	-34.8	-44.0	-46.5	-62.1	-100.8	-151.3	-183.3
+10 B_m	-4.1	-19.7	-34.8	-44.0	-49.2 (5.9)	-62.1	-100.8	-151.3	-183.3
-10 D_m	-5.1 (24.4)	-23.4 (18.6)	-38.5 (10.5)	-44.0	-49.2 (5.9)	-62.1	-100.8	-151.3	-183.3
+10 D_m	-3.3 (-20.0)	-16.5 (-16.3)	-32.1 (-7.9)	-42.2 (-4.2)	-46.5	-62.1	-100.8	-151.3	-183.3
-10 K_s	-4.1	-19.7	-34.8	-44.0	-46.5	-62.1	-100.8	-151.3	-183.3
+10 K_s	-4.1	-19.7	-34.8	-44.0	-49.2 (5.9)	-62.1	-100.8	-151.3	-183.3
-10 C_t	-4.1	-19.7	-34.8	-44.0	-46.5	-62.1	-100.8	-151.3	-183.3
+10 C_t	-4.1	-19.7	-34.8	-44.0	-49.2 (5.9)	-62.1	-100.8	-151.3	-183.3
-10 M_p	-4.1	-19.7	-34.8	-44.0	-46.5	-62.1	-100.8	-151.3	-183.3
+10 M_p	-4.1	-19.7	-34.8	-44.0	-46.5	-62.1	-100.8	-151.3	-183.3
-10 B_p	-4.1	-19.7	-34.8	-44.0	-46.5	-62.1	-100.8	-151.3	-183.3
+10 B_p	-4.1	-19.7	-34.8	-44.0	-49.2 (5.9)	-62.1	-100.8	-151.3	-183.3
-10 J_l	-4.1	-19.7	-34.8	-44.0	-46.5	-62.1	-100.8	-151.3	-183.3
+10 J_l	-4.1	-19.7	-34.8	-44.0	-49.2 (5.9)	-62.1	-100.8	-151.3	-183.3
-10 B_l	-4.1	-19.7	-34.8	-44.0	-46.5	-62.1	-100.8	-151.3	-183.3
+10 B_l	-4.1	-19.7	-34.8	-44.0	-49.2 (5.9)	-62.1	-100.8	-151.3	-183.3
high \bar{q}	-4.1	-19.7	-34.8	-44.0	-46.5	-62.1	-103.3 (2.5)	-151.3	-183.3
low \bar{q}	-4.2 (2.2)	-19.7	-34.8	-44.0	-49.2 (5.9)	-62.1	-100.8	-151.3	-183.3

Table 4.4 Frequency Domain Parameter Sensitivity - Phase Lag. The numbers enclosed in the parenthesis denote the change from the nominal response in percent. No parenthesis within the block denotes zero deviation.

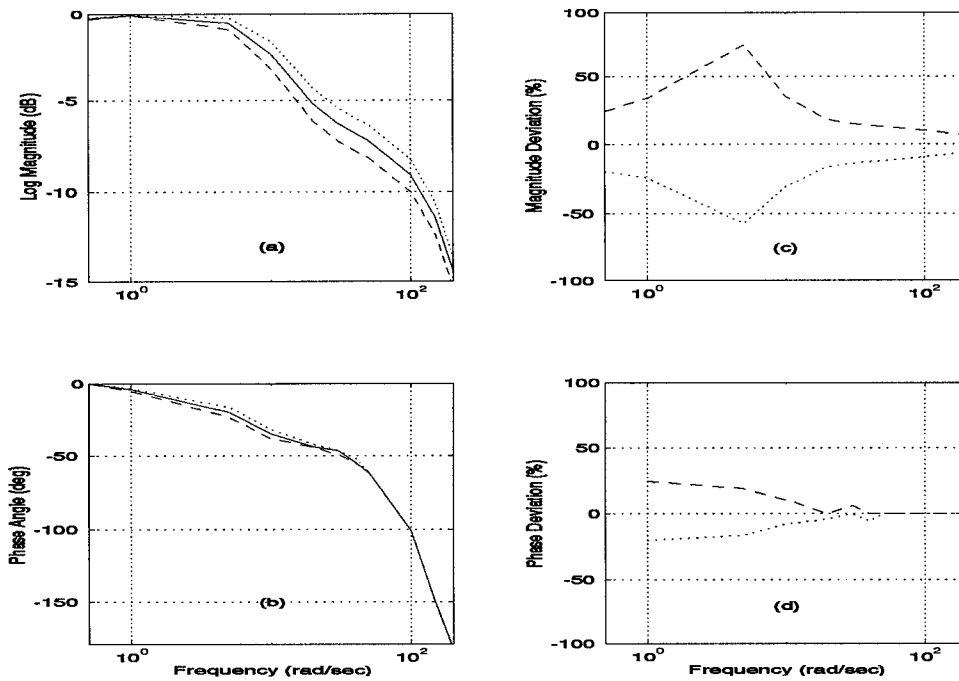


Figure 4.3 Deviations from the Nominal Response due to Pump Displacement Parameter D_m Variations

of feedback controls. Tachometers are typically used to sense the rotational velocities, while Linear Variable Differential Transformers (LVDT), usually embedded inside the actuator piston chamber, are used to sense the piston RAM movement [2]. There are two basic types of errors that are dealt with in this thesis: random and bias. With random errors, the signals can take on any values within a band of finite size from the nominal values, with no particular patterns. With sensor bias errors, the signals are offset from the nominal values by a constant amount. The sensor errors can either be introduced gradually over the lifetime of the sensor (i.e., wear and tear) or introduced abruptly due to component failures. The degree of bias errors or random noise determines the width of the error band.

All sensors introduce some degree of inaccuracy. More accurate sensors cost more and the relationship between cost and accuracy is exponential. Design engineers must decide on the amount of inaccuracy that can be tolerated in the design. Sensors can then be chosen to meet both the accuracy and cost requirements. Designers can either increase the sensor's specification, which will

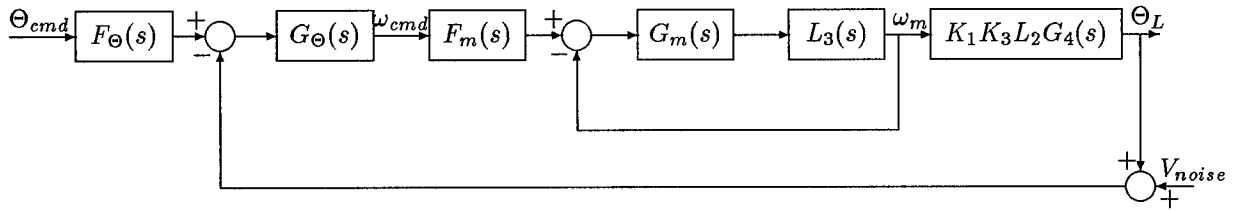


Figure 4.4 Addition of LVDT Sensor Noise in QFT Feedback Structure

increase cost, or design the system in such a way that the system can function with lower quality or degraded sensors, without causing excessive noise at the output. If the system, including the compensator, is more resistant to sensor noise, then the system can function effectively despite sensor accuracy degradation caused over time.

Now, it is a well known fact that a high system gain tends to amplify the effects of sensor noise; hence, the most effective countermeasure to sensor noise is to decrease the control system's loop gain as much as possible, while still meeting specifications, e.g., tracking and disturbance rejection [9]. QFT is an ideal design method to economically accomplish this gain reduction. As explained in Chapter 3, the troughs in the composite bounds on the Nichols chart allow for substantial gain reductions.

The sensor noise is introduced in the feedback path where the signal is measured, as shown in Fig. 4.4. This is substantially different than introducing the sensor noise on the output. If the noise source is added to the output, inside the feedback path (i.e., d_2), the noise would behave more like an external disturbance shown in Fig. 3.19. The noise sensor can then directly change the output, a phenomenon that is physically impossible. The proper placement of the sensor noise in the feedback structure is in the feedback path. This would then only add noise to the measured signal, not directly to the output.

4.4.1 *Random Sensor Noise Error.* The advantages of the QFT design can easily be seen in Figs. 4.5 through 4.11, which simulate the effects of LVDT sensor noise (random error) in the QFT structure as shown in Fig. 4.4. The maximum error toleration level of typical aircraft quality actuator RAM LVDTs is about one percent [14]. For example, if the RAM is commanded to a positive one inch travel, the sensor detects values ranging from 1.01 or 0.99 inches. This uncertain feedback quantity can then cause chattering, or noise, on the output as the feedback control system tries to zero out the error. Unit step responses with 1% sensor uncertainties of both the high forward gain and QFT designs are shown in Fig. 4.5. For Figs. 4.5 through 4.10, the figures (a) are the high forward gain design responses, while the figures (b) are the QFT design responses. The zero-noise responses for the respective designs are shown as dashed lines in all the figures. As can be seen from the figures, the QFT design substantially outperforms the high gain design. The effect of noise is almost negligible in the QFT design, while noise effects are quite visible in the high gain design.

The differences are even more startling as the signal to noise ratio is decreased from 100 to 1. Even with the sensor noise level equal to that of the commanded input, the QFT design nominally tracks the unit step command. But with the high gain design, the output is fairly chaotic, with the output amplified to about six times the commanded signal.

The quantitative comparison is just as startling. A noise error function shown in Eq. (4.2) is used to compare the simulation models. The noise error function measures the deviation of the non-zero noise response from the nominal (i.e., zero noise) response. The absolute value function is used instead of a quadratic function to reduce the relative scaling of the resulting error function values. If a quadratic function is used instead, the relative difference would be in the order of 400 times rather than 20 times.

$$E = \int_0^1 \text{abs}(y_{\text{nominal}}(t) - y_{\text{noise}}(t))dt \quad (4.2)$$

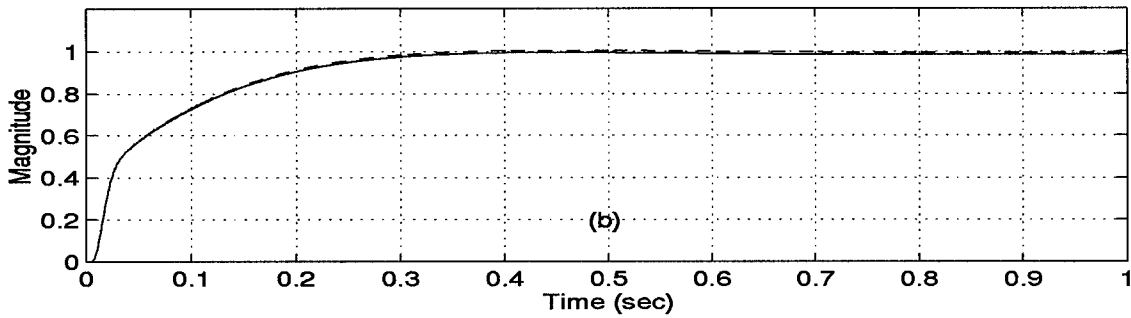
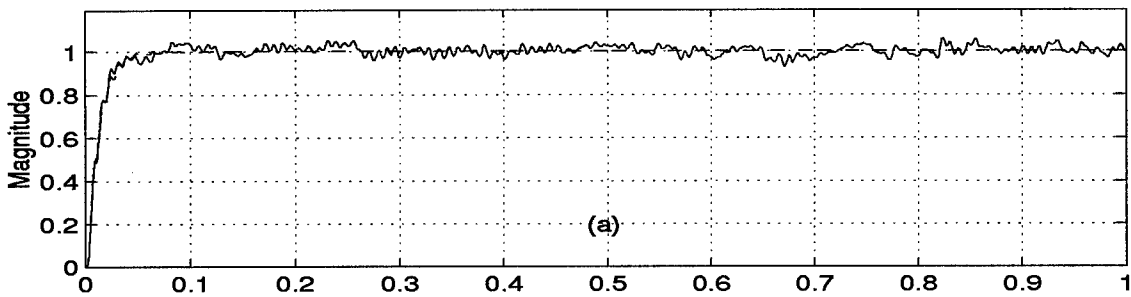


Figure 4.5 Unit Step Response with LVDT Signal to Noise Ratio of 100. (a) High Gain design response (b) QFT design response

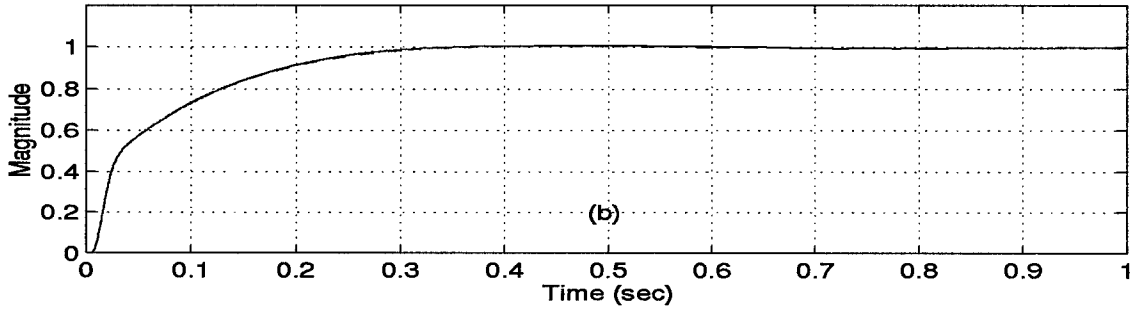
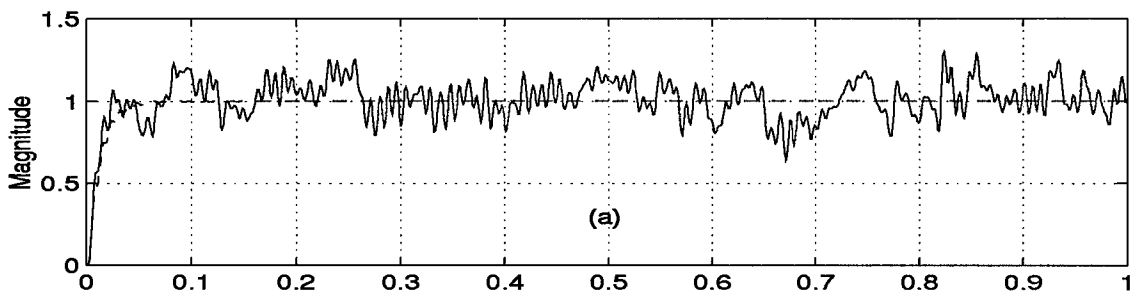


Figure 4.6 Unit Step Response with LVDT Signal to Noise Ratio of 20. (a) High Gain design response (b) QFT design response

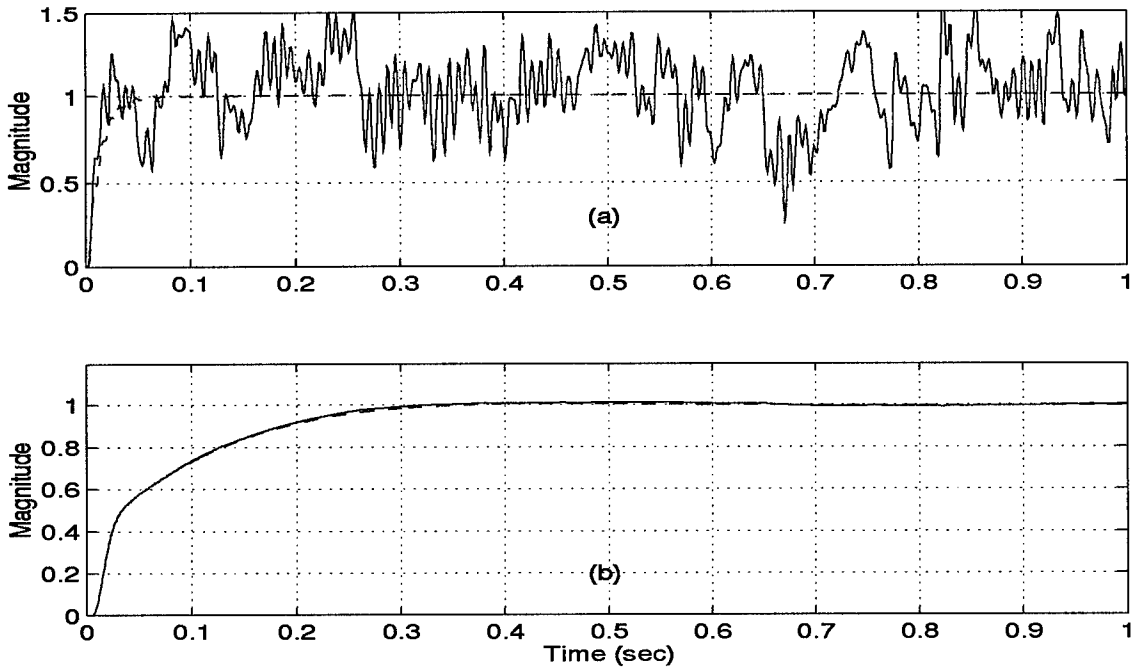


Figure 4.7 Unit Step Response with LVDT Signal to Noise Ratio of 10. (a) High Gain design response (b) QFT design response

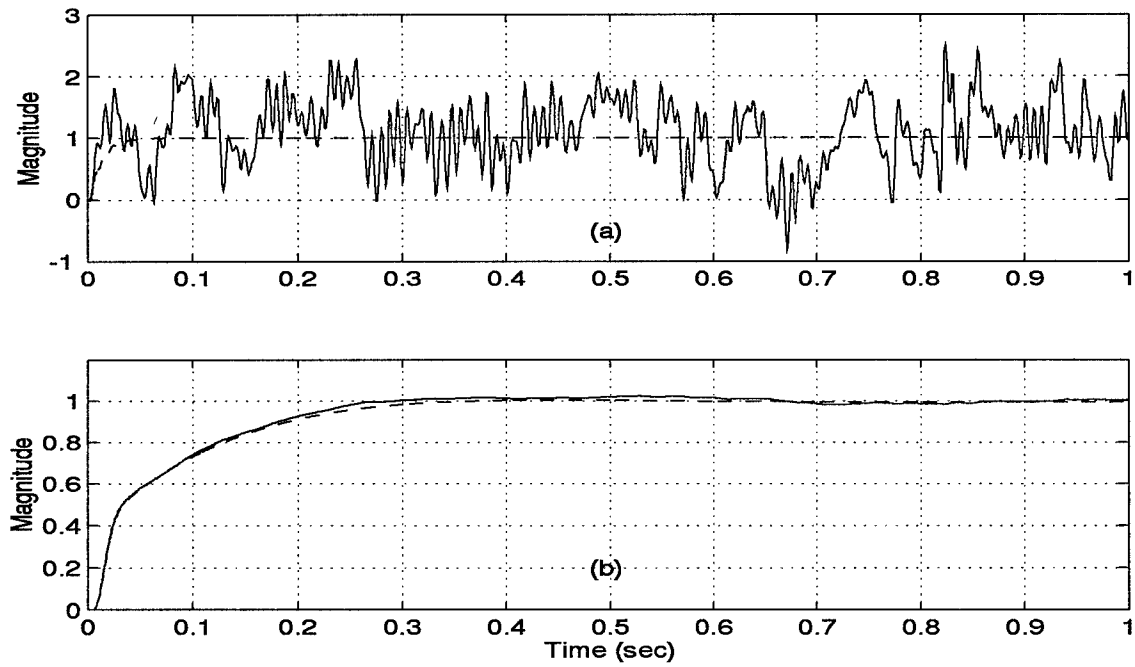


Figure 4.8 Unit Step Response with LVDT Signal to Noise Ratio of 4. (a) High Gain design response (b) QFT design response

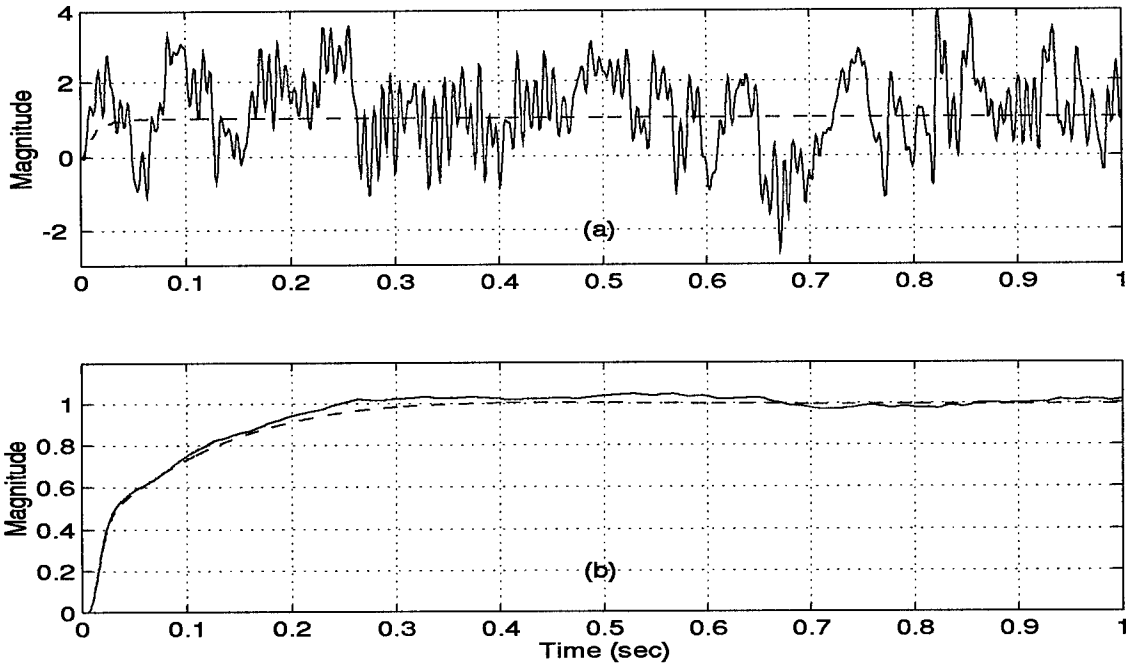


Figure 4.9 Unit Step Response with LVDT Signal to Noise Ratio of 2. (a) High Gain design response (b) QFT design response

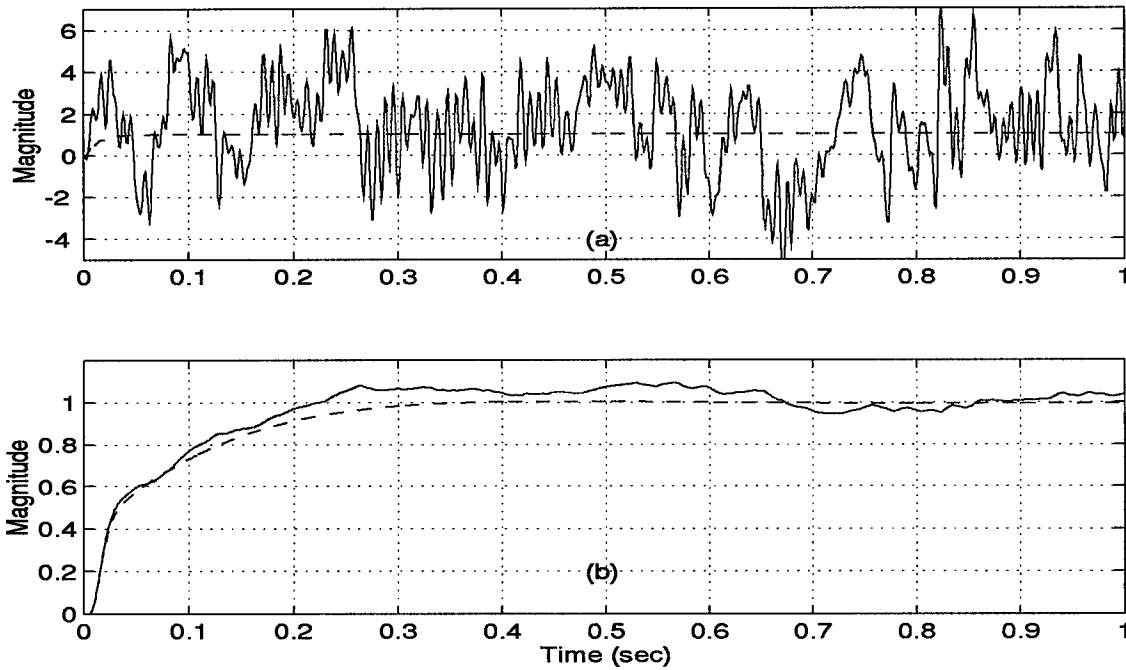


Figure 4.10 Unit Step Response with LVDT Signal to Noise Ratio of 1. (a) High Gain design response (b) QFT design response

SNR	High Gain Design	QFT Design
100	0.0176	0.0004
20	0.0879	0.0022
10	0.1759	0.0045
4	0.4397	0.0112
2	0.8793	0.0224
1	1.7587	0.0448

Table 4.5 Noise Error Function Relative to the Signal to Noise Ratio

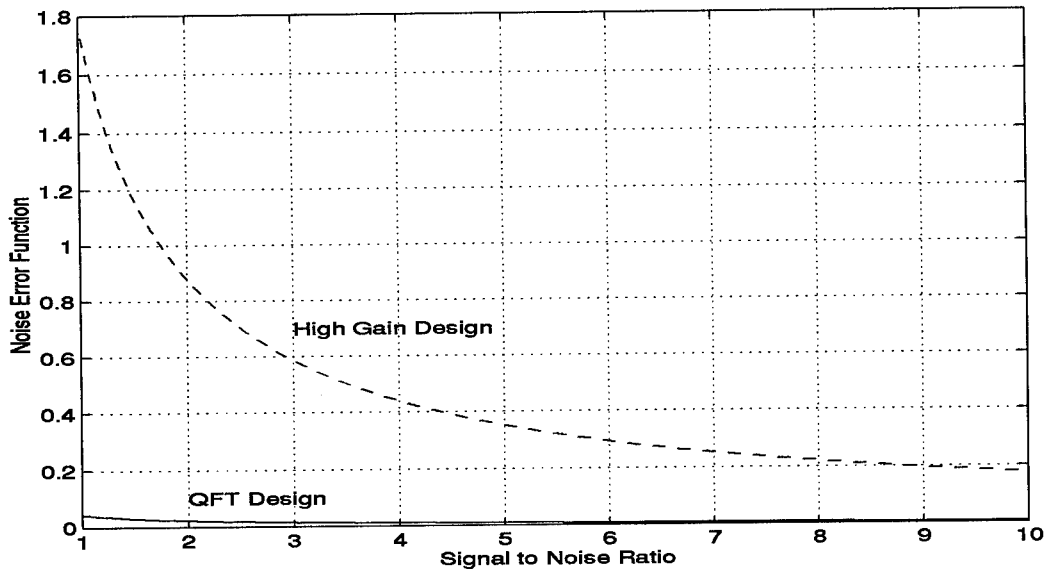


Figure 4.11 Relative Comparison of Noise Error Function due to the Changes in Signal to Noise Ratio

4.4.2 Sensor Bias Error. The QFT design handles sensor bias errors better than that of the high gain design. If the feedback signal is offset from the actual output level due to a sensor bias, control systems will chase after an offset steady state value rather than the commanded value. The ripples seen on the initial rise of output responses in Figs. 4.12(a) and 4.13(a) are the results of the system dynamics not sensor bias. Even with just 1% sensor bias level, the output steady state error of the high gain design, shown in Fig. 4.12(a), is about $\pm 15\%$ while the error for the QFT design, shown in Fig. 4.12(b), is about $\pm 1\%$. The problem worsens in Fig. 4.13, where the

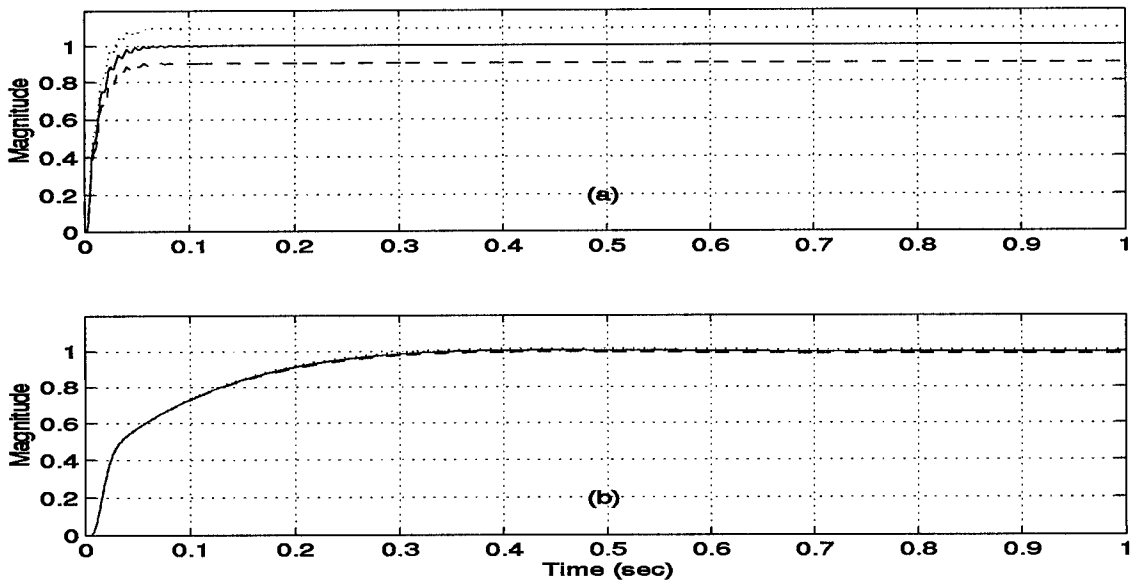


Figure 4.12 Unit Step Response with Sensor Bias Error of $\pm 1\%$

sensor bias error of about $\pm 10\%$ is applied. As seen in Fig. 4.13(b), the QFT design limits the error to about $\pm 10\%$, while the high gain design, as seen in Fig. 4.13(a), amplifies the error to about $\pm 100\%$. While the QFT design limits the output error to the level of the bias, the high gain design amplifies the effect of the bias by 10 to 15 times. Again, the QFT design is better at handling sensor bias than the high gain design.

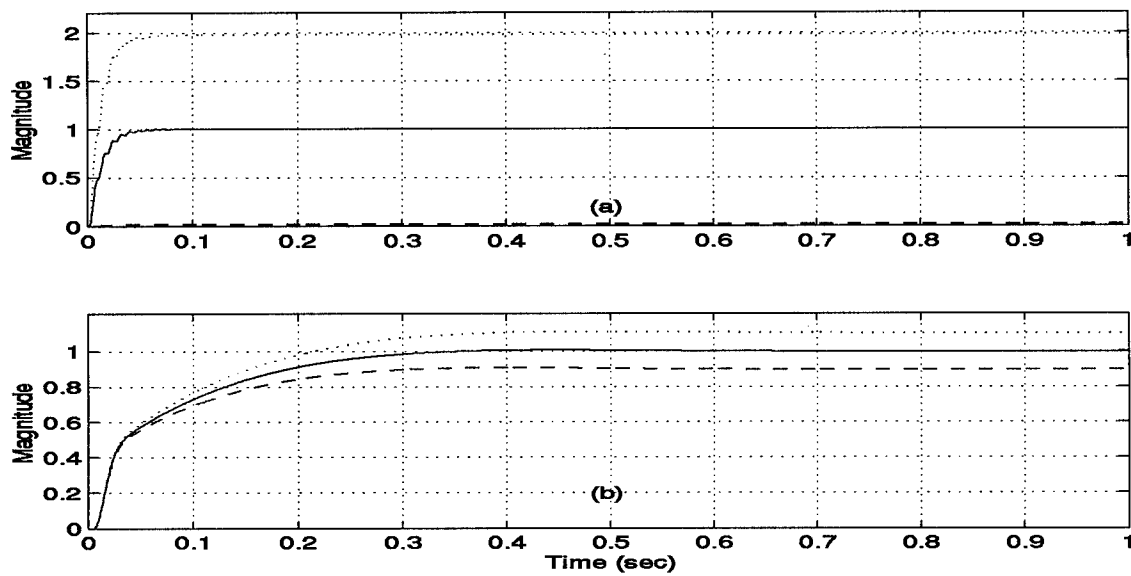


Figure 4.13 Unit Step Response with Sensor Bias Error of $\pm 10\%$

V. Flight Control System Using the EHA model

5.1 Flight Control System - Pitch Channel

The true test of the actuator design is to evaluate the actuator performance as an integral component of a flight control system. The flight control system is designed initially with the commonly used first-order actuator model $\frac{20}{s+20}$ [1]. The results are then compared against the fourth-order F-16 stabilator actuator and EHA models. The fourth-order conventional actuator and EHA models are given by Eqs. (5.1 and 5.2), respectively. The EHA model is for the nominal plant parameters belonging to the heart of the flight envelope. Different parts of the envelope yield slightly different EHA models.

$$\frac{\delta_e}{\delta_{cmd}} = \frac{(20.2)(71.4^2)(144.8)}{(s + 20.2)(s^2 + 2 * 0.736 * 71.4s + 71.4^2)(s + 144.8)} = \frac{N_{act}}{D_{act}} \quad (5.1)$$

$$\frac{\delta_e}{\delta_{cmd}} = \frac{6.8925 * 10^6 (s + 8)(s + 14.5)}{(s + 6.1 \pm j4.3)(s + 200)(s + 199.4 \pm j195.3)} = \frac{N_{act}}{D_{act}} \quad (5.2)$$

The first-order actuator model is frequently used in text book settings to simplify the model. However, the first-order model does not correctly represent the upper bandwidth frequency phase lag of the actual physical system [7]. A fourth-order actuator model, such as Eq. (5.1) which accurately describes the phase characteristics of the actual physical system, should be used to design flight control systems. However, the conventional actuator control systems have undesirable amount of phase lag at the upper end of the bandwidth. Thus, the EHA control system is designed to reduce the high bandwidth frequency phase lag. The reduced phase lag can minimize the chances of actuator rate saturation. The EHA model accurately predicts the physical system and behaves much like a first-order model.

The first-order and fourth-order conventional actuator models and EHA model are inserted in turn for simulations and comparisons. Since the EHA controller is designed for use with the stabilator, the flight control system controls the aircraft pitch by using the stabilator strictly as

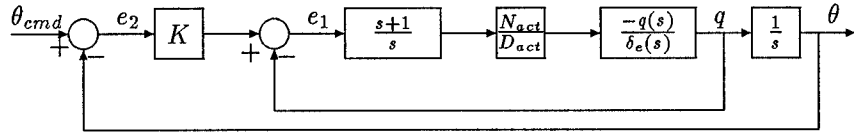


Figure 5.1 A Pitch Control Flight Control System

the elevator. The two basic specifications of the flight control system are the phase margin angle of $\gamma \geq 30^\circ$ and gain margin of $\geq 6dB$. The resulting design structure is shown in Fig. 5.1. The flight control system consists of two loops. The PI controller in the inner loop robustly stabilizes the unstable longitudinal aircraft model. The resulting inner loop is stable and more robust. The outer loop gain element K is used to improve the rise and settling time and decrease the peak overshoot. Both the inner loop and outer loop compensators are designed to maximize the aircraft performance at the nominal flight condition.

Most conventional flight control systems use a set of different controllers through gain scheduling for different parts of the envelope [8]. To simplify the simulations, a single set of inner and outer loop compensators is used for the whole flight envelope. The compensator set consists of a PI controller in the inner loop, and a gain element in the outer loop. The use of a single compensator set results in differing degrees of flight control system performances. The nominal plant is chosen at the heart of the flight envelope, namely the flight condition ac21 (Mach 0.7 and 30,000 ft altitude). Two other flight conditions, ac28 (Mach 0.78 and 50,000 ft) and ac41 (Mach 1.1 and 1,000 ft), are chosen to exercise the actuator in the extreme regions of the flight envelope. The FOMs of the nominal point in the envelope are shown in Table 5.1. As can be seen in Fig. 5.2, the aircraft responds quickly to a given pitch command at the nominal flight region. The frequency

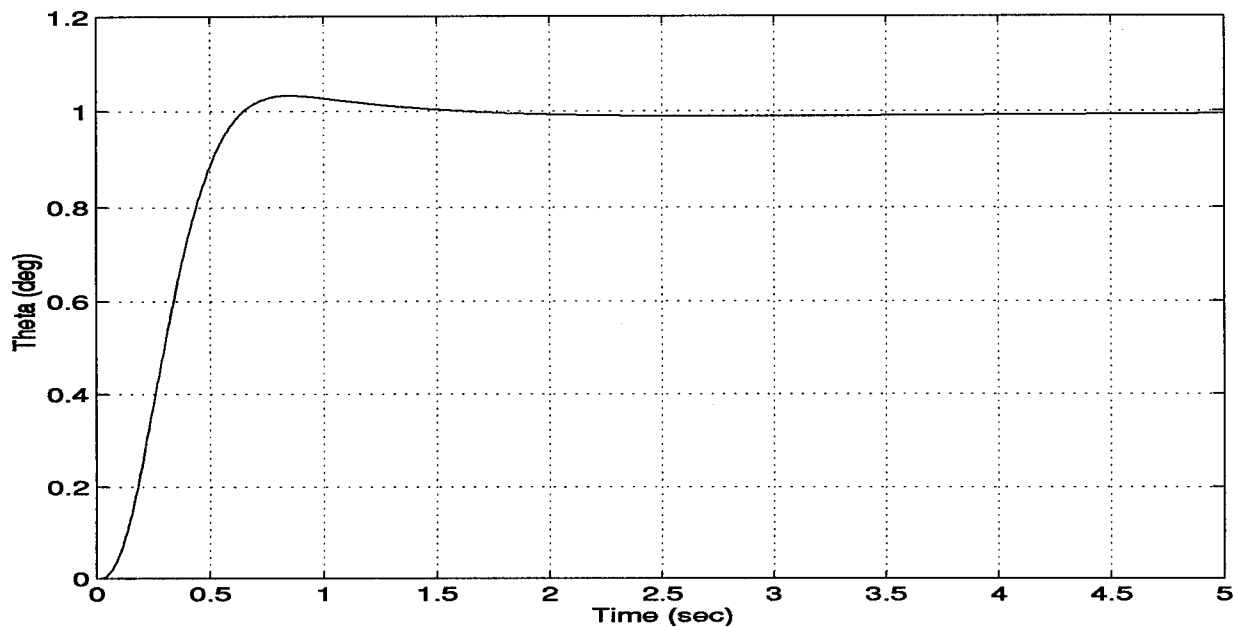


Figure 5.2 Time Domain Simulation of the Pitch Control System with a Simple First-Order Actuator Model and Nominal Plant Parameters

domain responses are shown in Fig. 5.3. As shown in Fig. 5.4, the gain margin and phase margin angle exceed the required specifications.

5.2 Simulations

5.2.1 Time Domain Simulations. The time domain simulations of the flight control system using different actuator models are shown in Figs. 5.5 to 5.7. In those three figures the dotted, dashed, and solid lines correspond to the results for the first-order conventional, the fourth-order conventional, and the EHA models, respectively. Figure 5.5 is the simulation results for the flight condition point ac21. All three actuator models behave similarly and result in slightly underdamped responses. Figure 5.6 is the simulation results for the flight condition point ac28. All three models behave similarly and result in underdamped responses. This is expected since the aircraft longitudinal damping factor and natural frequency change with the airspeed and altitude, changing the levels of oscillation. Figure 5.7 is the simulation results for the flight condition ac41,

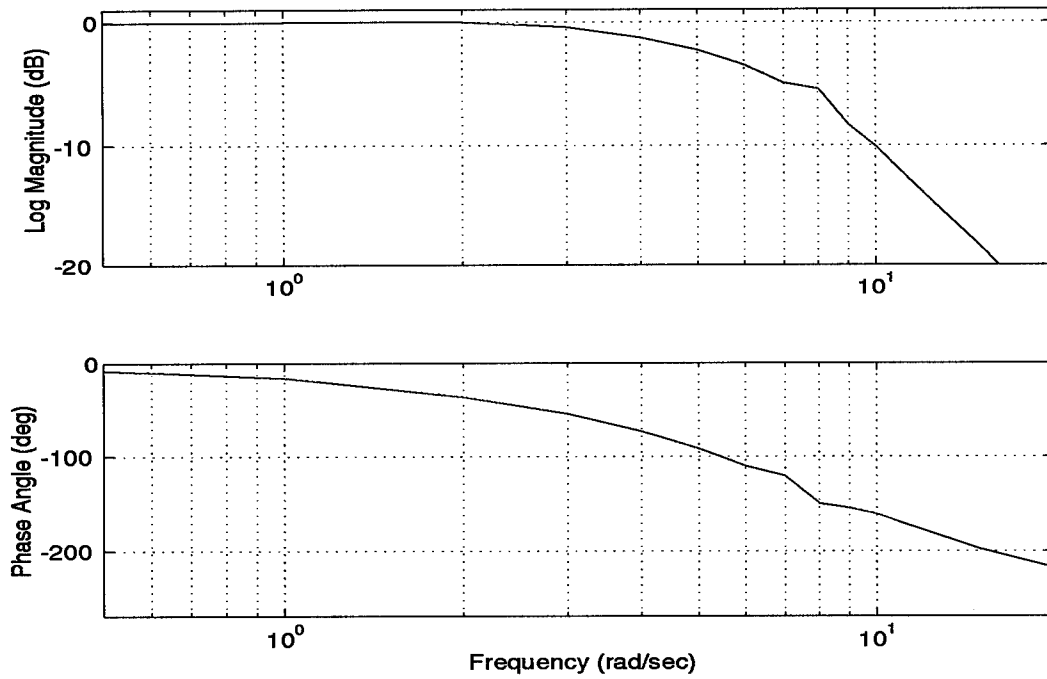


Figure 5.3 Frequency Domain Simulation of the Pitch Control System with a Simple First-Order Actuator Model and Nominal Plant Parameters

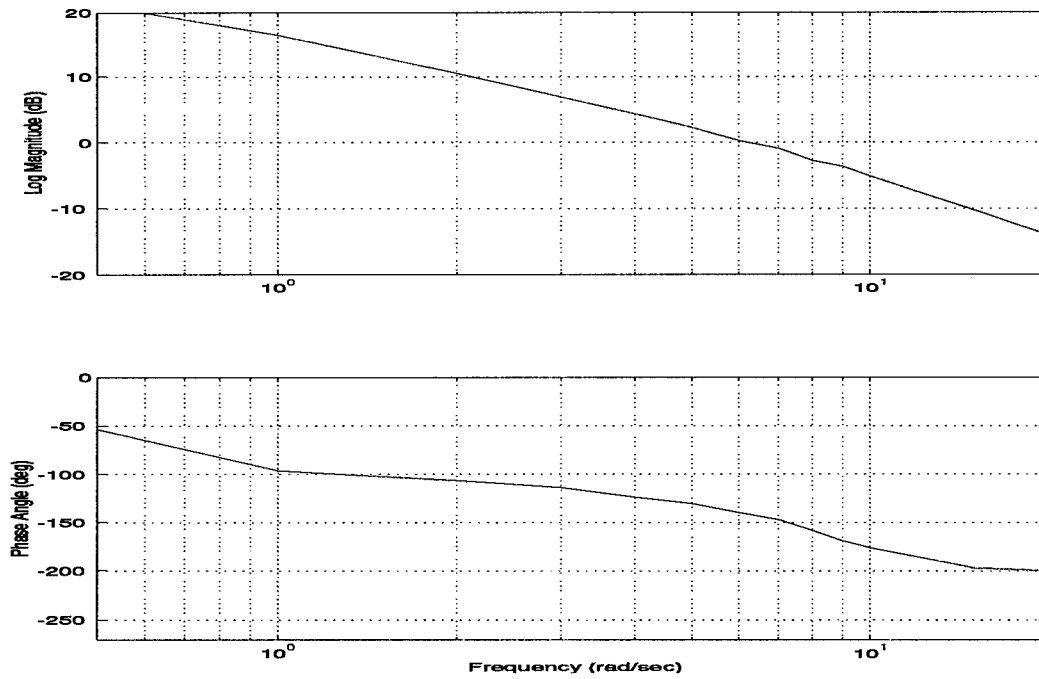


Figure 5.4 The Open Loop Frequency Response - Gain Margin 7.6 dB and Phase Margin Angle 35°

Aero Point	Actuator Type	t_r (sec)	M_p	t_p (sec)	t_s (sec)
ac21	1st Conv.	0.38	1.032	0.85	1.10
	EHA	0.36	1.044	0.75	0.95
	4th Conv.	0.31	1.030	0.68	0.78
ac28	1st Conv.	0.38	1.298	0.97	2.43
	EHA	0.38	1.328	0.96	3.85
	4th Conv.	0.35	1.351	0.93	3.77
ac41	1st Conv.	0.8	1.016	2.34	1.31
	EHA	0.81	1.017	2.32	1.30
	4th Conv.	n/a	n/a	n/a	n/a

Table 5.1 The Pitch Flight Control System Figures Of Merit

a supersonic envelope point. The response between the first-order and EHA models are nearly identical. However, the fourth-order model yields an unstable result. The instability is primarily due to the loop gain. Other supersonic envelope points also yield unstable responses with the fourth-order conventional model, while the responses with the first-order conventional and EHA models are stable. This topic is further explored in Section 5.3.

5.2.2 Frequency Domain Simulations. As mentioned previously, the conventional fourth-order actuator model displays more realistic phase information than the first-order model. The phase lag difference between the first-order and fourth-order models at the high end of the aircraft bandwidth can be as large as 50 degrees [7]. If the first-order model is used to design a flight control system, the phase lag problems can be addressed in one of two ways. The first is to maintain a higher phase margin angle in the design to compensate for the actuator lag. The second is to add enough lead to reduce the actuator lag to an acceptable level. The ultimate solution may be to incorporate little of both. The QFT compensator essentially entails lead, thereby reducing the phase lag in the loop.

Frequency simulations of the pitch control systems are shown in Figs. 5.8 to 5.10. For those three figures the dash-dotted, dashed, and solid lines correspond to the results from the first-order conventional, the fourth-order conventional, and the EHA models, respectively. Figures 5.8, 5.9,

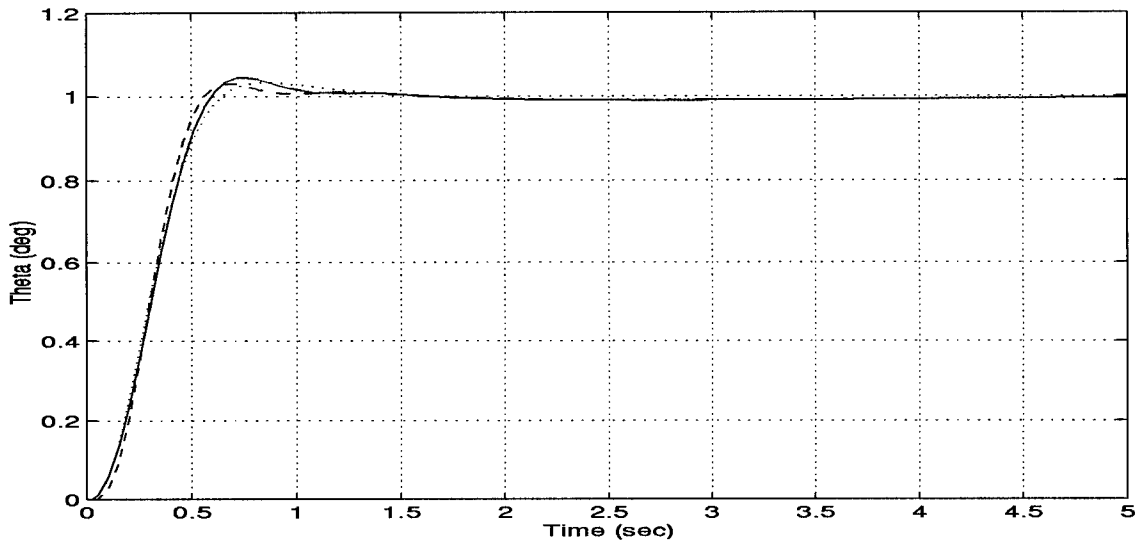


Figure 5.5 Time Domain Simulations of the Pitch Control System at Mach 0.7 and 30,000 ft Altitude. The dotted, dashed, and solid lines correspond to the results from the first-order conventional, the fourth-order conventional, and the EHA models, respectively.

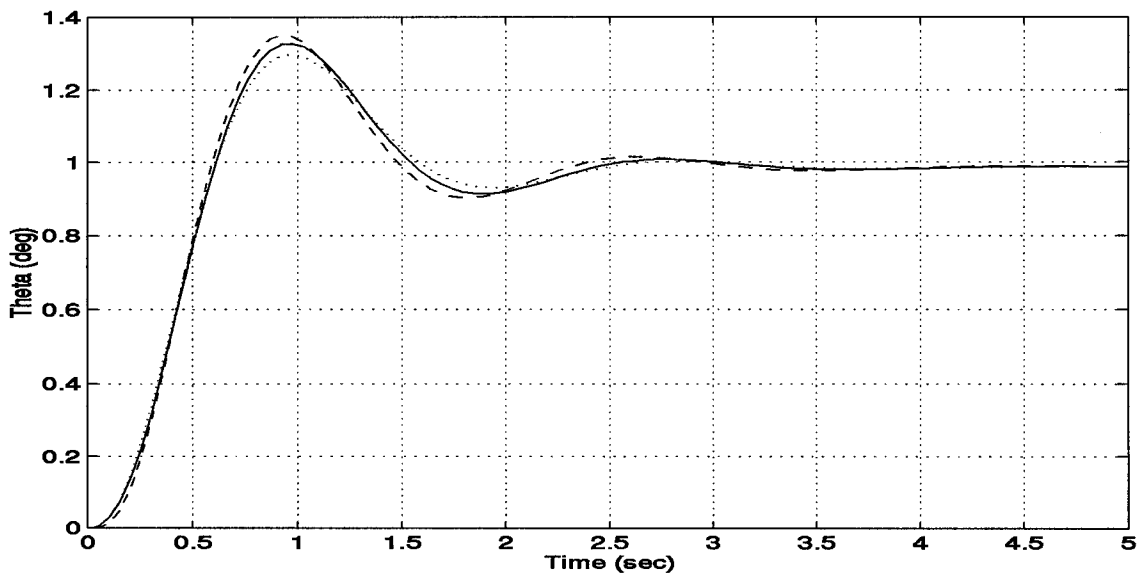


Figure 5.6 Time Domain Simulations of the Pitch Control System at Mach 0.78 and 50,000 ft Altitude. The dotted, dashed, and solid lines correspond to the results from the first-order conventional, the fourth-order conventional, and the EHA models, respectively.

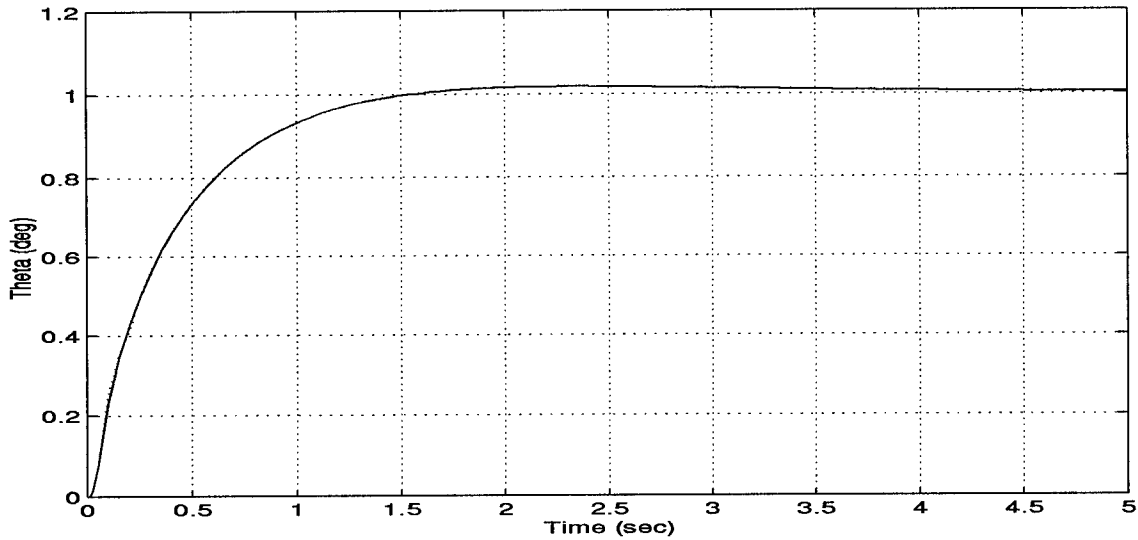


Figure 5.7 Time Domain Simulations of the Pitch Control System at Mach 1.1 and 1,000 ft Altitude. The dotted, dashed, and solid lines correspond to the results from the first-order conventional, the fourth-order conventional, and the EHA models, respectively.

and 5.10 are the simulation results for the flight conditions ac21, ac28, and ac41, respectively. The first-order and EHA models behave in a similar manner, but the fourth-order model exhibits more lag at the high frequency end of the actuator bandwidth. This larger phase lag of the fourth-order actuator model results in an unstable flight control system if the first-order model is used to design the flight control system instead.

The EHA model, designed using the QFT method, offers the second solution to the phase problem. The reduced EHA model is of second-order over fifth-order, in effect the actuator package is designed with some amount of lead already built-in. During the design stage, some lead is added to meet the given frequency domain specifications; specifications which the conventional fourth-order actuator (model) could not meet. Indeed, the conventional fourth-order actuator model suffers from excessive phase lag at high bandwidth frequency. The phase lead is achieved by adding zeros; thereby, reducing the phase lag at the high end of the bandwidth to within specifications. The EHA model fully describes the EHA behavior, yet it meets all frequency and time domain specifications. The main shortfall of using the first-order model is that it does not accurately describe the frequency

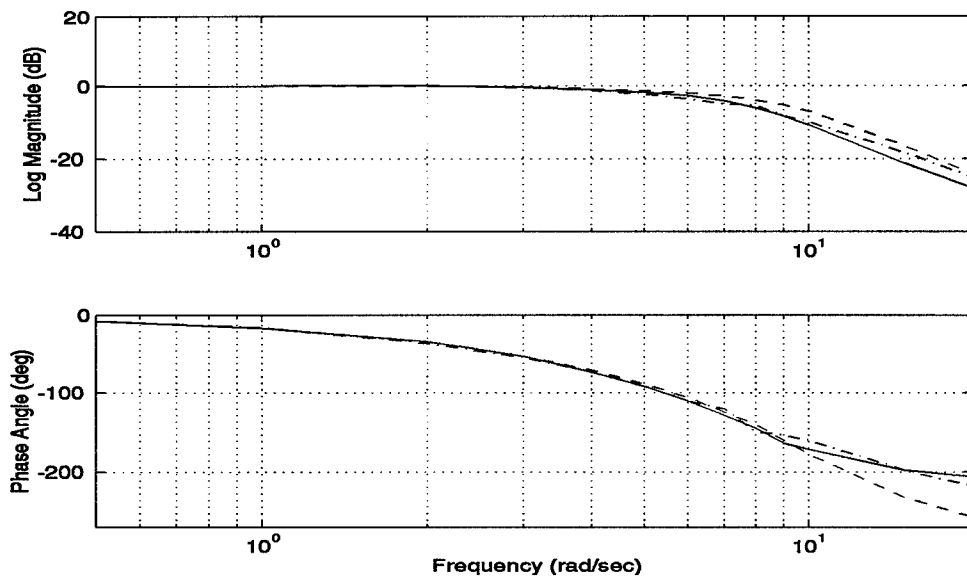


Figure 5.8 Frequency Domain Simulations of the Pitch Control System at Mach 0.7 and 30,000 ft Altitude. The dash-dotted, dashed, and solid lines correspond to the results from the first-order conventional, the fourth-order conventional, and the EHA models, respectively.

domain behavior of the actuator. The EHA model, composed of the actuator and compensator components, behaves like the first-order model, yet fully describes the behavior.

5.3 Instability of the Conventional Actuator

The flight control system in the supersonic region is stable with the first-order conventional actuator and EHA models while unstable with the fourth-order conventional actuator model. The instability is especially puzzling since the aircraft longitudinal models are stable in the supersonic region, but unstable in the subsonic region. In the supersonic region, the aircraft short period poles are a pair of negative complex conjugates. In the subsonic region, one of the poles is positive while the other is negative. Hence, the flight control simulations with the fourth-order conventional actuator model should be stable in the supersonic region and unstable in the subsonic region. However, the opposite is true.

Two possible causes for the supersonic instability are explored. The instability may be caused

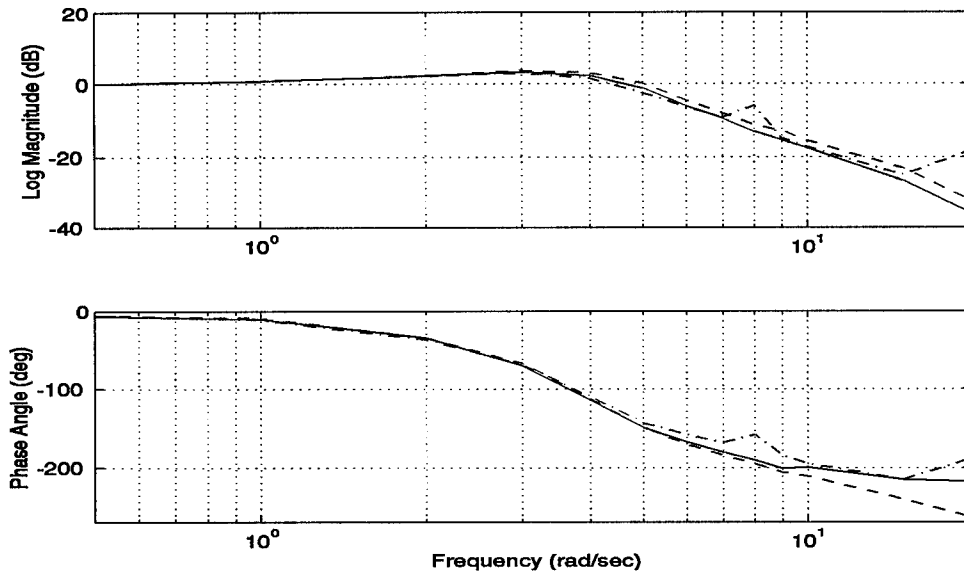


Figure 5.9 Frequency Domain Simulations of the Pitch Control System at Mach 0.78 and 50,000 ft Altitude. The dash-dotted, dashed, and solid lines correspond to the results from the first-order conventional, the fourth-order conventional, and the EHA models, respectively.

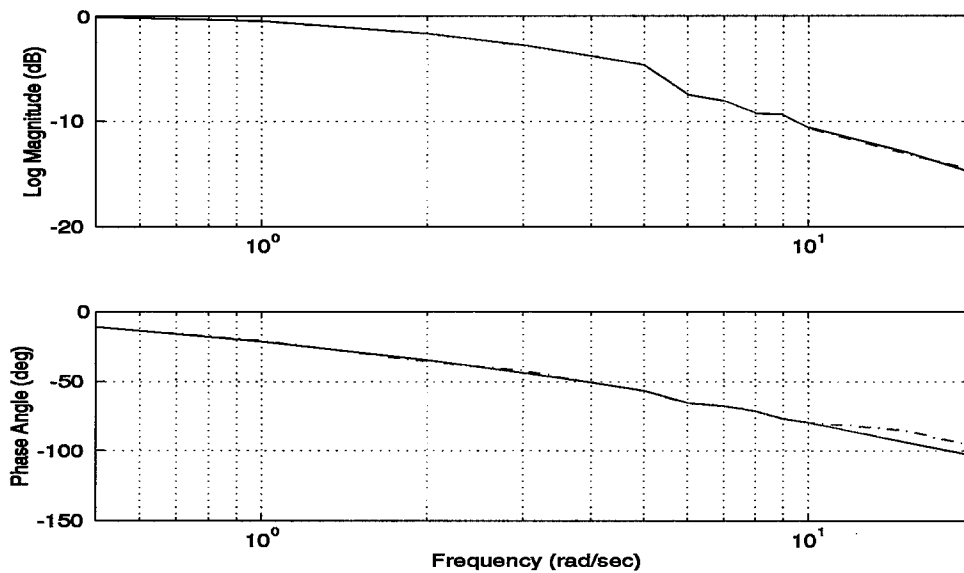


Figure 5.10 Frequency Domain Simulations of the Pitch Control System at Mach 1.1 and 1,000 ft Altitude. The dash-dotted and solid lines correspond to the results from the first-order conventional and the EHA models, respectively.

by excessive lags; the phase lag of the fourth-order model is greater than that of the first-order and EHA models. To test this hypothesis, a slow prefilter, $\frac{1}{s+1}$, is placed in series after the step input. The prefilter did not change the simulation results. The phase lag did not seem to be the dominant cause of the instability.

$$\frac{q}{e2_{ac21}} \frac{4thConv}{=} = \frac{1.2453 * 10^8 (s + 1)(s + 0.6)}{s(s - 0.8)(s + 1.9)(s + 20.2)(s + 52.6 \pm j48.3)(s + 144.8)} \quad (5.3)$$

$$\frac{q}{e2_{ac41}} \frac{4thConv}{=} = \frac{1.1804 * 10^9 (s + 1)(s + 2.6)}{s(s + 2.3 \pm j7.1)(s + 20.2)(s + 52.6 \pm j48.3)(s + 144.8)} \quad (5.4)$$

Equations (5.3 and 5.4) represent the inner open loop transfer functions (OLTF) for two flight conditions, a subsonic condition (ac21) and a supersonic condition (ac41). As can be seen from the poles of the transfer functions, an unstable pole exists in the subsonic OLTF while the supersonic OLTF poles are all stable. However, due to the static loop gains, all the subsonic closed loop poles are stable but two supersonic closed loop poles are unstable. The static loop gain for the flight condition ac21 is 3.29 while for the flight condition ac41 is 3.69. The maximum allowable gain for stability to be maintained is the gain at the point where the dominant root locus branch crosses the imaginary axis from the negative real plane to the positive real plane.

The root locus for Eq. (5.4) is shown in Fig. 5.11. The root locus for Eq. (5.3) is similar to Fig. 5.11. Figure 5.12 shows the root locus for Eq. (5.4) near the origin. For the flight condition ac21, the gain at the imaginary axis crossing is 4.67, above the static loop gain of 3.29 for the transfer function. Hence, the closed loop poles remain stable. For the flight condition ac41, the gain at the imaginary axis crossing is 0.5, well below the static loop gain of 3.69 for the transfer function. The static loop gain of 3.69 results in a pair of unstable closed loop complex conjugate poles. This gain difference is the key in explaining why the flight control system becomes unstable in the supersonic region while it remains stable in the subsonic region.

$$\frac{q}{e2_{ac41}} \frac{EHA}{=} = \frac{5.4065 * 10^8 (s + 1)(s + 3.6)(s + 8)(s + 14.5)}{s(s + 6.1 \pm j4.3)(s + 2.3 \pm j7.1)(s + 200)(s + 199.4 \pm j195.3)} \quad (5.5)$$

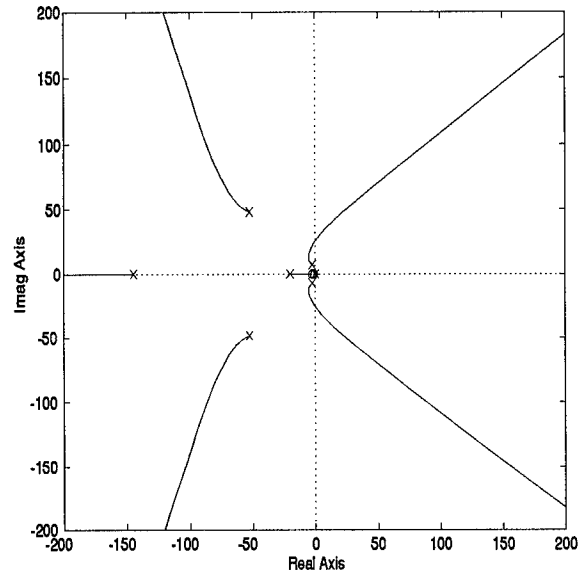


Figure 5.11 The Inner Loop Root Locus with the Fourth-Order Conventional Actuator - Eq. (5.4)

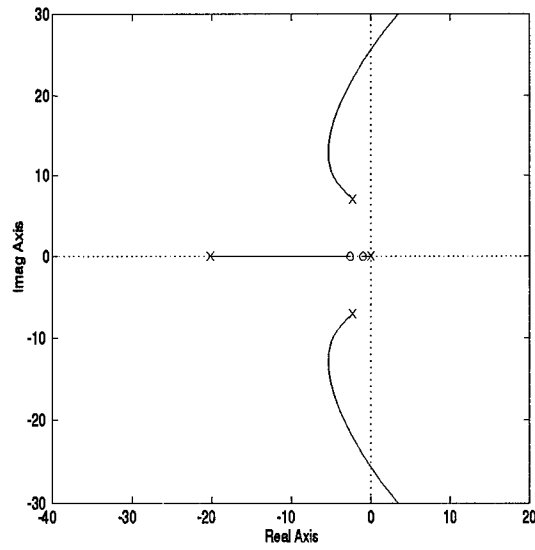


Figure 5.12 The Inner Loop Root Locus with the Fourth-Order Conventional Actuator Near the Origin - Eq. (5.4)

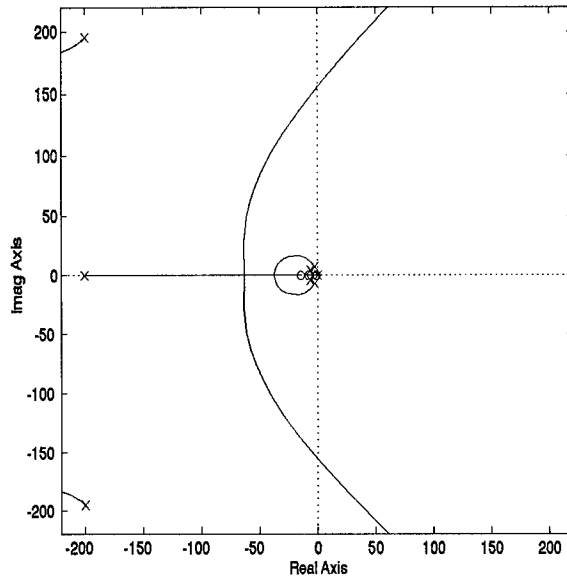


Figure 5.13 The Inner Loop Root Locus with the EHA - Eq. (5.5)

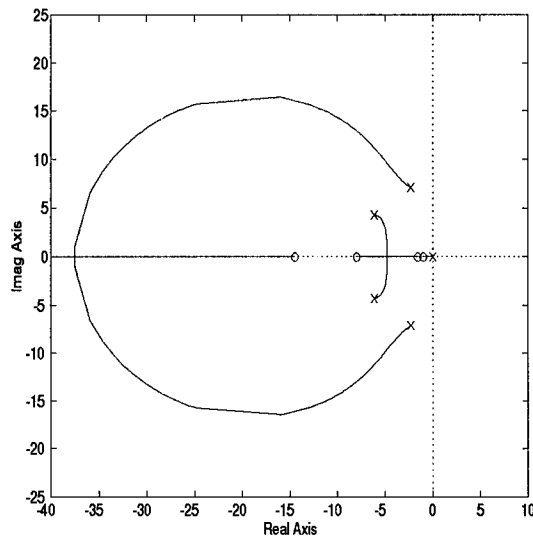


Figure 5.14 The Inner Loop Root Locus with the EHA Near the Origin - Eq. (5.5)

The fourth-order model's gain at the imaginary axis crossing is quite low compared to the other two models'. The flight control system with the EHA model ensures a high degree of stability with a large gain at the imaginary axis crossing of about 55, about hundred times larger than in the fourth-order model. The static loop gain of the EHA model is 7.78, well below the gain at the imaginary axis crossing. Hence for most gain ranges, the EHA model is stable while the fourth-order model is not. The root locus for Eq. (5.5) is shown in Fig. 5.13. Figure 5.14 shows the root locus for Eq. (5.5) near the origin. As can be seen in the figures, the flight control system utilizing the QFT designed EHA is inherently more robust with respect to the gain variations.

VI. Consideration of Frequency Specifications in QFT

6.1 Introduction

In most minimum-phase QFT problems, the stability bounds are used to ensure the phase characteristics of the controller design. However, the stability bounds are inadequate in describing the complete frequency characteristics of the tracking bounds. But there are problems involving only the minimum-phase plants, where the frequency specifications are specifically given and must be met in order to satisfy the design criteria. The frequency specifications may even become the dominant design constraint over the time domain specifications. The frequency specifications are important constraints in the EHA controller design. The current QFT paradigm states that only the magnitude tolerances be satisfied for the minimum-phase plant cases, while both the magnitude and phase tolerances be specified and satisfied for the non-minimum-phase plant cases [3]. The current QFT paradigm also ignores the addition of phase by the prefilter.

Sub-component controller designs, such as actuators in flight control systems, are a class of problems where more complete frequency constraints are desired. The sub-components themselves must be stable. Furthermore, the sub-components must minimize their contribution to the system's phase lag to maintain overall system stability. Hence, the sub-components require more complete frequency specifications in addition to the phase margin angle. Two additional steps to the current QFT design procedure are proposed. First, embed the magnitude and phase constraints in the tracking models. Second, add the phase constraints, in addition to the magnitude constraints, in the prefilter design stage.

6.2 Embedding the Frequency Constraints in Deriving the Tracking Models

The upper and lower tracking bound models must be synthesized to meet the frequency domain specifications as well as the time domain specifications. The relationship between the time and frequency domain responses are tenuous at best. But there are simple well known rules in

controlling the frequency and time domain responses with pole and zero placements. Using these rules, the tracking bound models can be found in most cases to satisfy the frequency and time domain specifications.

In the time domain, the dominant poles are only minimally effected by much faster poles. Also high frequency zeros minimally effect the response of the slower dominant poles. For example, the time response of the control ratio $\frac{25}{s+25}$ is not significantly different than the time response of the control ratio $\frac{100(s+100)}{(s+25)(s+400)}$. The time and frequency domain responses of the two control ratios are shown in Figs. 6.1 and 6.2. The first-order model responses are shown in solid lines, while the complex model responses are shown in dotted lines. As Fig. 6.1 shows, the time responses of two models are quite comparable. The t_r , t_s , and M_p are almost identical between the two models. The effects of the additional zero at -100 and pole at -400 are minimal in the time domain. However, as Fig.6.2 shows, the frequency responses between the two models are quite different. At 200 rad/sec, the phase difference is about 40 degrees and the magnitude difference is about 5 dB. Hence, the dominant poles can be used to establish the desired time domain response, while high frequency poles and zeros can be used to satisfy the desired frequency domain response.

6.3 The Prefilter Phase Constraints

The controllers guarantee the robustness of the output; the prefilters control the input signal tracking. However, the prefilters inject additional phase and attenuation to the system. The current QFT design paradigm, when applied to the minimum-phase systems, only uses the attenuation constraints in the prefilter design. The inclusion of the phase constraints in the prefilter design is proposed. The prefilter magnitude bounds specify the minimum and maximum attenuation values at a given frequency. The prefilter magnitude constraints are defined by

$$Lm\mathcal{F}(j\omega) = LmT_R(j\omega) - LmT(j\omega) \quad (6.1)$$

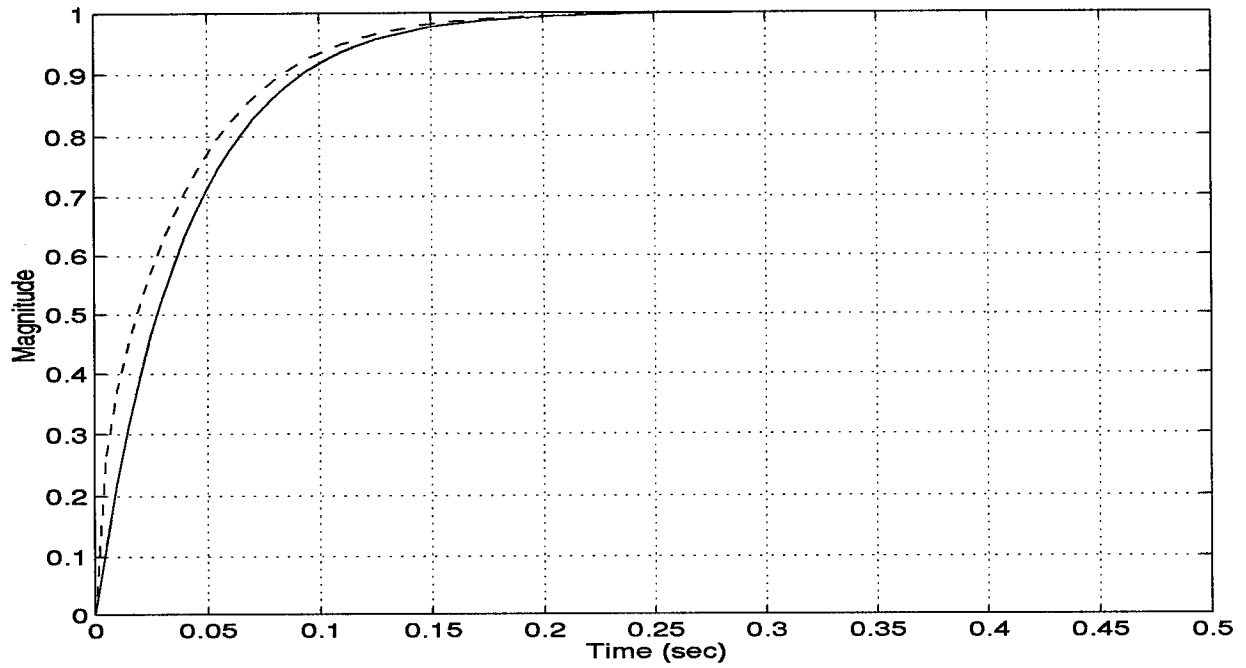


Figure 6.1 Time Domain Responses of Simple First-Order Tracking Model (Solid Line) and Complex Tracking Model (Dashed Line)

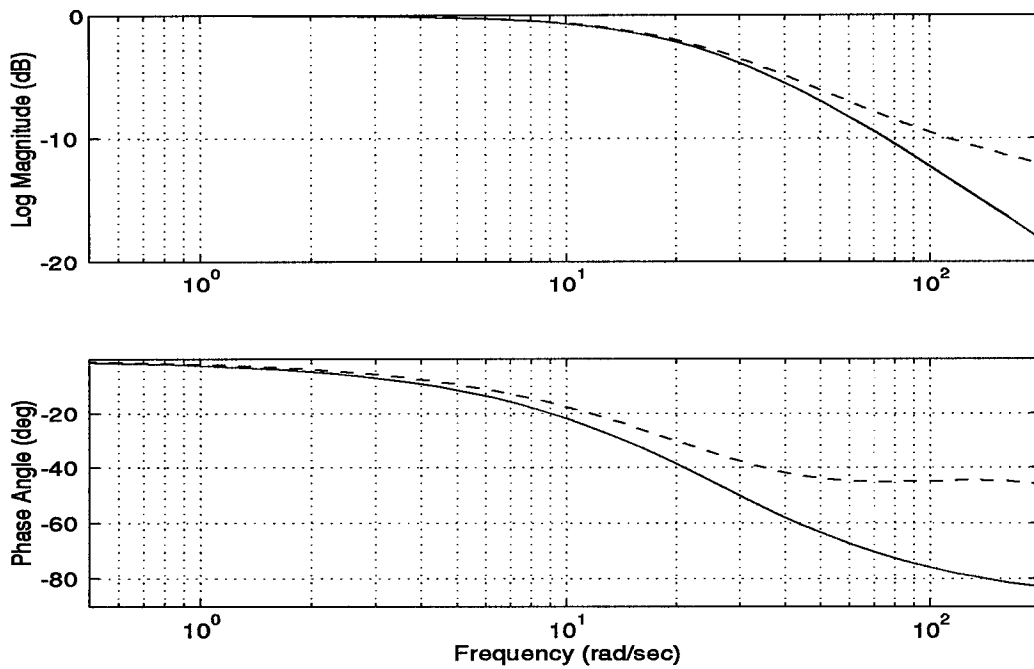


Figure 6.2 Frequency Domain Responses of Simple First-Order Tracking Model (Solid Line) and Complex Tracking Model (Dashed Line)

where T_R are the upper and lower tracking bounds and T is defined as

$$T(j\omega) = \frac{\mathcal{L}(j\omega)}{1 + \mathcal{L}(j\omega)} \quad (6.2)$$

and where $\mathcal{L}(j\omega)$ is the loop transmission. The prefilter phase bounds specify the minimum and maximum phase values at a given frequency. The prefilter phase constraints can similarly be defined by

$$\angle \mathcal{F}(j\omega) = \angle T_R(j\omega) - \angle T(j\omega) \quad (6.3)$$

In Bode magnitude plots, a pole contributes $-20dB/dec$ while a zero contributes $+20dB/dec$ to the system magnitude starting from the corner frequency. However, in Bode phase plots, a pole contributes -90° while a zero contributes $+90^\circ$ to the system phase starting from the decade before the corner frequency to the decade after. The magnitude contribution of the prefilter poles and zeros are immediate at the corner frequency, while the phase contributions are spread out over two decades. Depending on the locations of the prefilter poles and zeros, the prefilter phase contribution within the system bandwidth can vary. High frequency poles and zeros may contribute little or no additional phase within the system bandwidth, while low frequency poles and zeros contribute substantial amounts of phase. Low frequency zeros can be used to reduce the overall system phase.

The prefilter poles and zeros required to satisfy the magnitude constraints may not necessarily satisfy the phase constraints, as shown in Figures 6.3 and 6.4. The minimum-phase plant $\frac{0.98(s+15)}{s(s+15.24)}$ and compensator $\frac{2.8 \cdot 10^6(s+14.5)}{(s+8.5)(s^2+400s+80000)}$ are used for computing both figures. In both figures, the dashed lines denote the constraints, while the solid lines denote the system frequency responses. The frequency response with the prefilter $\frac{(s+3.6)(s+8)(s+277.8)}{(s+3.2)(s+50)(s+50)}$ is shown in Fig. 6.3. As the figure shows, the magnitude constraints are satisfied while the phase constraints are violated.

Designers must find a set of poles and zeros that satisfy both the magnitude and phase constraints within the system bandwidth. To do this, the phase constraints defined in Eq. (6.3), along with the magnitude constraints, must be considered in the prefilter design process. Using both the

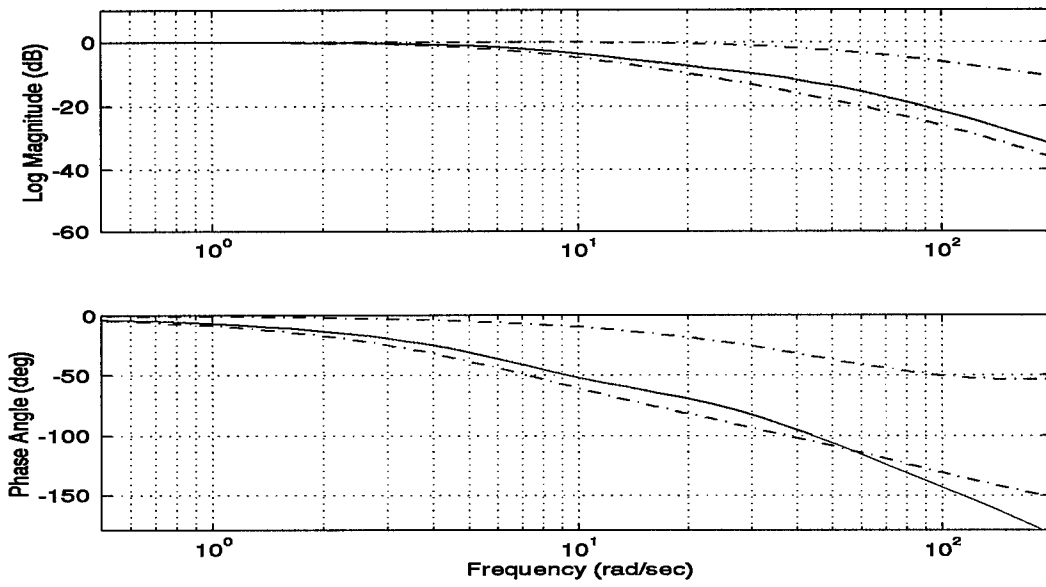


Figure 6.3 A Prefilter Design that Satisfy the Magnitude Constraints but not Phase Constraints

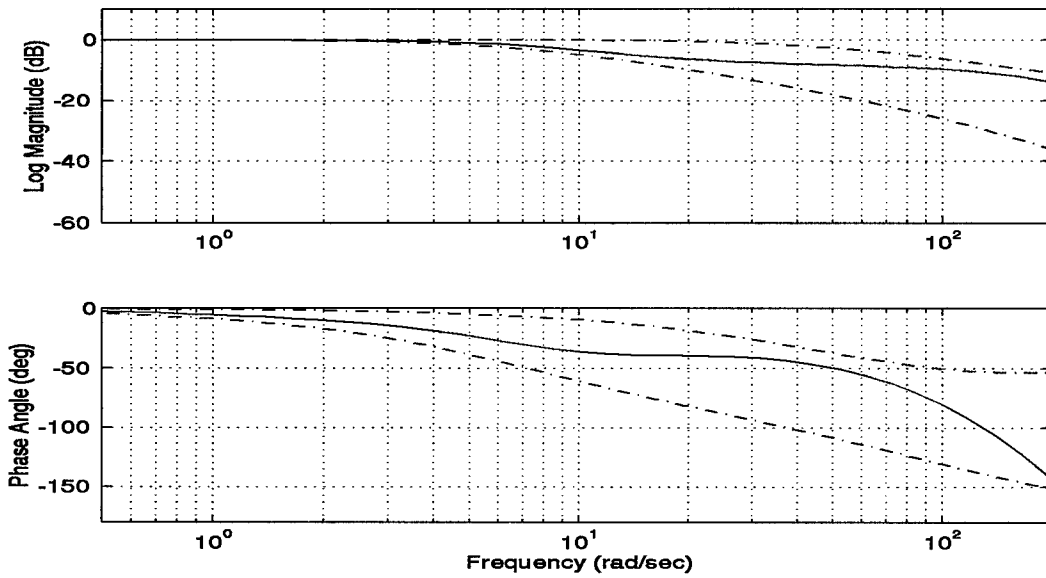


Figure 6.4 A Prefilter Design that Satisfy the Magnitude and Phase Constraints

magnitude and phase constraints in the prefilter design stage, a design that satisfies the magnitude and phase constraints is found. The frequency response with the prefilter $\frac{(s+3.6)(s+8)(s+6666.7)}{(s+3.2)(s+200)(s+300)}$ is shown in Figure 6.4. As the figure shows, both the magnitude constraints and phase constraints are satisfied.

VII. *Conclusions and Recommendations*

7.1 *Conclusions*

The Electro-Hydrostatic Actuator (EHA) offers a higher degree of combat survivability and easier maintainability over the conventional actuators. The main objective of this thesis is to apply the Quantitative Feedback Theory (QFT) in designing a control system for the EHA. The use of QFT establishes a rigorous design procedure and facilitates other EHA control system design in the future. In this thesis effort, the QFT is shown as a viable tool in solving a real-world problem. The QFT controller design process is greatly simplified by the QFT CAD package, which reduces the manual computations to a minimum.

In Chapter 2, a mathematical model of the EHA is derived using a fundamental device modeling technique. A mathematical model that completely describes the EHA dynamics is required to design a control system. The sub-component dynamic models are used to construct the required EHA model, resulting in a complex feedback structure shown in Fig. 2.3.

In Chapter 3, the EHA model in Fig. 2.3 is rearranged using a standard set of block manipulation rules, to form the standard QFT feedback structures shown in Fig. 3.10. The EHA model orders are reduced in each design stages to simplify the design process. However, the full model is used for simulations and analysis. The inner loop controller increases the outer loop robustness, by shrinking the region of uncertainties for the outer loop. The outer loop controller and prefilter design enforce the tracking of commands. The resulting controller and prefilter design comply with the given set of specifications.

In Chapter 4, the sensitivities of the EHA and high gain control system to parameter variations and sensor noise, are analyzed. Variations of the pump displacement parameter D_m are shown to cause the most variations to the output response, in the time domain as well as in the frequency domain. The QFT design is compared against the high gain design for sensor noise handling characteristics. The effects of sensor noise are almost negligible in the QFT control system

response while the effects of sensor noise dominate the high gain control system response. The QFT controller nominally tracks the unit step command even with the signal to noise ratio of 1, while the high gain design fails to track the command.

In Chapter 5, the EHA model used in a simple flight control system is compared against the same flight control system with the first-order and fourth-order conventional hydraulic actuator models. Some lead is added to the EHA control system to meet the given flight control system frequency domain specifications; the specifications which the conventional fourth-order actuator (model) could not meet. The flight control system with the EHA model is more stable with respect to gain variations than the flight control system with fourth-order conventional actuator model. The amount of lag at the upper bandwidth frequency is reduced with the EHA model, which minimizes the chances for actuator rate saturation. The EHA model behaves like the first-order actuator model, yet fully describes the behavior of the actuator.

In Chapter 6, two additional design steps to augment the current QFT design paradigm are proposed. First, embed the magnitude and phase constraints to the tracking models. Second, add the phase constraints in addition to the magnitude constraints in the prefilter design stage. These two steps are necessary in order to design a control system for some minimum-phase problems where the frequency specifications dominate the design constraints over the time domain specifications.

7.2 Recommendations

The following recommendations are made for future research:

- *Study the application of dynamic compensation to conventional hydraulic actuators.* A conventional hydraulic actuator control system designed using QFT can improve the phase characteristics of the actuators, reducing the likelihood of rate saturation. The EHA like frequency response can be achieved from the conventional actuator through dynamic compensation.

- *Devise and implement a gain scheduling scheme* to automatically switch between the QFT controller in the small-signal region and the high gain controller in the large-signal region, viz., a dual mode controller. The high gain ('Bang Bang') design is more efficient in the large-signal region, but suffers from the adverse effects of sensor noise in the small-signal region.
- *Implement the EHA control system design in the EHA prototype hardware.* The EHA hardware was not accessible during this thesis effort. The design achieved in this thesis should be tested on the EHA hardware to make any necessary refinements to the design.
- *Incorporate the phase constraints in the prefilter design* module of the QFT CAD package.

Appendix A. Device Fundamentals

A.1 Motor Fundamentals

If direct current is passed through a conductor, the resulting magnetic field flux loop around the conductor is in the direction determined by the right hand rule. If this conductor is placed perpendicular to a steady magnetic field, the field flux on one side of the conductor is additive while the opposite side field flux is destructive with respect to the steady magnetic field flux. The resulting imbalance generates a force which is orthogonal to the current and the steady magnetic field. In Fig. A.1, current is coming out of the page causing the induced magnetic flux field to rotate in a counterclockwise direction. This is the basic principle of the electrical direct-current (DC) motor operation.

The term *back electromotive force (emf)* refers to the induced voltage in the conductor caused by a conductor motion in the magnetic field [2]. A voltage can be induced in the conductor if the conductor moves in the direction of the force in the magnetic field. This effect tends to counteract the current induced flux; thereby, reducing the strength of the flow field around the conductor and counteracting the rotational motion. The back emf is the cause of electrical damping in motors [2].

The two basic components of DC motors are stator and rotor (armature). The stators generate the steady magnetic flux field, while the armatures (i.e., conductor) generate the current induced

Current i flows through the conductor, out of the page

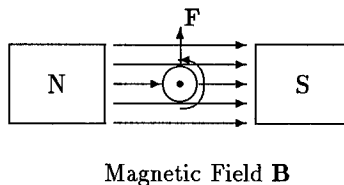


Figure A.1 DC Motor Principle - Top View

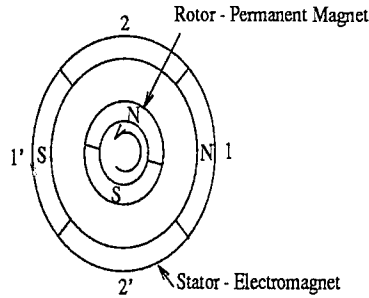


Figure A.2 Brushless DC Motor

magnetic flux and rotate within the field. Conventional DC motors use electromagnets rather than permanent-magnets for the stators. This is accomplished by applying current to the coil windings around the stator. The current is applied to the commutators, rigidly mounted to the rotor, through a pair of brush. The brush maintains contact with the commutator even as the armature itself rotates. The commutators are placed such that the direction of the torque can be maintained. The major disadvantage of the conventional DC motors are excessive wear of components due to the physical contact between the brush and commutator, heat due to friction, and sparks due to electrical arcing. The severity of the problems can be reduced through better designs.

Brushless DC motors use an armature made of permanent-magnets and rely on electrical switching of the current on the stator windings to achieve commutation [2]. The magnetic polarity of the rotor is fixed while the magnetic polarity of the stator is electrically switched to achieve rotation. Brushless DC motors contain multiple sets of diametrically opposed stator segment pairs. The current flow is maintained such that it is always opposite between the stator segment pairs; thus, maintaining the opposite polarity. The commutation is achieved by sequentially applying current to the stator pairs as the armature rotates. In modern brushless DC motors, the commutation occurs electronically through a feedback control system. A microcontroller senses the angular rotor position then commands the appropriate stator to achieve near constant torque levels [2].

However, the torque levels may fluctuate due to the finite physical dimension of the stator and rotor, resulting in torque ripples. The maximum torque is produced when the stator and

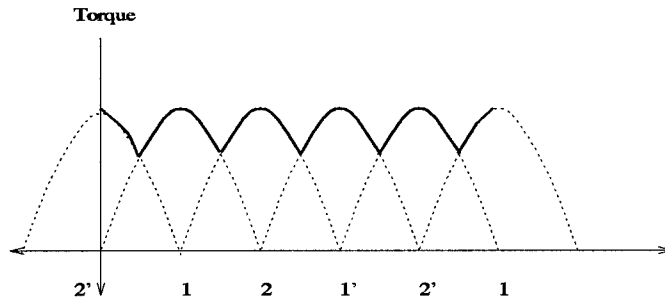


Figure A.3 Torque Ripples

rotor are of opposite polarity. The minimum torque is produced when the stator and rotor are of equal polarity. As can be seen in Fig. A.3, due to this transitioning cycles from the maximum to minimum, the static torque levels are not constant but rippled instead. To be efficient, the motor needs to generate as much torque as possible with given energy, by minimizing the drop in the torque levels as the armature rotates between phases. The motor utilized by the EHA designers consists of 18 slot stators and six pole rotors to minimize the torque ripples [13]. In addition, the permanent-magnet rotor is made from rare earth materials to improve the electromagnetic efficiency of the motor.

A.2 Pump and Fluid Fundamentals

The primary function of the pump is to transfer hydraulic fluid from the reservoir into the actuator chamber. The EHA design utilizes an integrated bi-directional motor/pump assembly [13]. The direction of the motor travel determines both the pump and actuator directions. The pump is a bent axial piston hydraulic pump. As the DC motor begins to rotate, the drive shaft inside the pump rotates as well. This motion in turn causes one of the pump pistons to rise, drawing its chamber with hydraulic fluid from the inlet port. As the rotation continues, the piston begins to descend and pressurizes the fluid. This pressurized fluid is then released into the actuator chamber.

One of the servovalves used in the actuator controls the flow direction, flow rate, and to some extent fluid pressure. The servovalve commands the spool, sometimes referred to as *land*, which

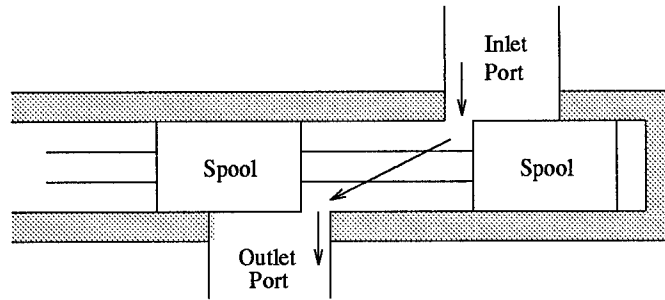


Figure A.4 Principle of Servovalve

either closes or opens the inlet and outlet port to let the fluids flow. If the spools are wider than the ports, then overlapping occurs which results in a dead zone. If the ports are wider than the spools, then underlapping occurs which results in leakage. It is physically not possible to exactly match the spool and port sizes. Dead zones tend to decrease stability and sensitivity in this application. Thus, a more common design is to accept a small amount of leakage instead [5]. The leakage causes small disturbances in the nominal flow rate.

Appendix B. Plant Models

P_{i11}	$= \frac{555.556(s-0.001)(s-1.086)(s+1.536)(s+45.602\pm j777.971)}{(s-0.681\pm j0.029)(s+1.705)(s+4.609)(s+44.666\pm j787.133)}$
P_{i12}	$= \frac{505.051(s-0.001)(s-1.086)(s+1.536)(s+45.602\pm j777.971)}{(s-0.730)(s-0.634)(s+1.714)(s+4.200)(s+44.746\pm j786.304)}$
P_{i13}	$= \frac{617.284(s-0.001)(s-1.086)(s+1.536)(s+45.602\pm j777.971)}{(s-0.681\pm j0.064)(s+1.697)(s+5.103)(s+44.568\pm j788.145)}$
P_{i14}	$= \frac{555.556(s-0.001)(s-1.086)(s+1.536)(s+45.602\pm j777.971)}{(s-0.845)(s-0.490)(s+1.695)(s+4.241)(s+44.840\pm j785.400)}$
P_{i15}	$= \frac{505.051(s-0.001)(s-1.086)(s+1.536)(s+45.602\pm j777.971)}{(s-0.688\pm j0.126)(s+1.709)(s+4.799)(s+44.574\pm j788.044)}$
P_{i16}	$= \frac{617.284(s-0.001)(s-1.086)(s+1.536)(s+45.602\pm j777.971)}{(s-0.799)(s-0.550)(s+1.720)(s+4.620)(s+44.666\pm j787.131)}$
P_{i17}	$= \frac{617.284(s-0.001)(s-1.086)(s+1.536)(s+45.602\pm j777.971)}{(s-0.695\pm j0.169)(s+1.720)(s+4.620)(s+44.666\pm j787.131)}$
P_{i18}	$= \frac{505.051(s-0.001)(s-1.086)(s+1.536)(s+45.602\pm j777.971)}{(s-0.820)(s-0.521)(s+1.692)(s+4.599)(s+44.666\pm j787.135)}$
P_{i19}	$= \frac{555.556(s+0.004)(s+2.315\pm j7.134)(s+45.607\pm j777.517)}{(s+2.057\pm 3.976)(s+2.507\pm 3.627)(s+44.668\pm j786.695)}$
P_{i110}	$= \frac{505.051(s+0.004)(s+2.315\pm j7.134)(s+45.607\pm j777.517)}{(s+2.672\pm 4.757)(s+1.691\pm 3.010)(s+44.749\pm j785.864)}$
P_{i111}	$= \frac{617.284(s+0.004)(s+2.315\pm j7.134)(s+45.607\pm j777.517)}{(s+1.385\pm 4.348)(s+3.423\pm 3.003)(s+44.570\pm j787.709)}$
P_{i112}	$= \frac{555.556(s+0.004)(s+2.315\pm j7.134)(s+45.607\pm j777.517)}{(s+3.811\pm 3.369)(s+0.945\pm 4.151)(s+44.476\pm j788.609)}$
P_{i113}	$= \frac{505.051(s+0.004)(s+2.315\pm j7.134)(s+45.607\pm j777.517)}{(s+3.334\pm 3.508)(s+1.321\pm 4.063)(s+44.576\pm j787.607)}$
P_{i114}	$= \frac{617.284(s+0.004)(s+2.315\pm j7.134)(s+45.607\pm j777.517)}{(s+2.426\pm 4.799)(s+2.046\pm 2.823)(s+44.759\pm j785.781)}$
P_{i115}	$= \frac{617.284(s+0.004)(s+2.315\pm j7.134)(s+45.607\pm j777.517)}{(s+3.440\pm 3.802)(s+1.123\pm 3.899)(s+44.667\pm j786.644)}$
P_{i116}	$= \frac{505.051(s+0.004)(s+2.315\pm j7.134)(s+45.607\pm j777.517)}{(s+2.258\pm 4.819)(s+2.306\pm 2.681)(s+44.667\pm j786.644)}$

Table B.1 Full Set of Inner Loop Plants

P_{i11}	=	$\frac{555.556(s+45.827\pm j777.983)}{(s+4.951)(s+44.666\pm j787.133)}$
P_{i12}	=	$\frac{505.051(s+45.827\pm j777.983)}{(s+4.550)(s+44.747\pm j786.304)}$
P_{i13}	=	$\frac{617.284(s+45.827\pm j777.983)}{(s+5.438)(s+44.568\pm j788.145)}$
P_{i14}	=	$\frac{555.556(s+45.827\pm j777.983)}{(s+4.601)(s+44.840\pm j785.399)}$
P_{i15}	=	$\frac{505.051(s+45.827\pm j777.983)}{(s+5.134)(s+44.574\pm j788.043)}$
P_{i16}	=	$\frac{617.284(s+45.827\pm j777.983)}{(s+4.767)(s+44.757\pm j786.221)}$
P_{i17}	=	$\frac{617.284(s+45.827\pm j777.981)}{(s+4.951)(s+44.666\pm j787.131)}$
P_{i18}	=	$\frac{505.051(s+45.827\pm j777.985)}{(s+4.951)(s+44.666\pm j787.134)}$
P_{i19}	=	$\frac{555.556(s+47.923\pm j777.686)}{(s+9.136)(s+44.664\pm j786.733)}$
P_{i110}	=	$\frac{505.051(s+47.924\pm j777.686)}{(s+8.734)(s+44.745\pm j785.902)}$
P_{i111}	=	$\frac{617.284(s+47.924\pm j777.686)}{(s+9.623)(s+44.566\pm j787.747)}$
P_{i112}	=	$\frac{555.556(s+47.924\pm j777.686)}{(s+9.519)(s+44.472\pm j788.646)}$
P_{i113}	=	$\frac{505.051(s+47.924\pm j777.686)}{(s+9.318)(s+44.572\pm j787.644)}$
P_{i114}	=	$\frac{617.284(s+47.924\pm j777.686)}{(s+8.952)(s+44.756\pm j785.820)}$
P_{i115}	=	$\frac{617.284(s+47.925\pm j777.633)}{(s+9.135)(s+44.664\pm j786.681)}$
P_{i116}	=	$\frac{505.051(s+47.924\pm j777.729)}{(s+9.136)(s+44.663\pm j786.775)}$

Table B.2 Reduced Set of Inner Loop Plants

P_{o11}	=	$\frac{3.96*10^{10}(s+45.827\pm j777.983)(s+15)}{(s+0.001)(s+15.428)(s+894.904)(s+584.316)(s+49.816\pm j790.503)(s+45.602\pm j777.971)}$
P_{o12}	=	$\frac{3.60*10^{10}(s+45.827\pm j777.983)(s+15)}{(s+0.001)(s+15.483)(s+469.743)(s+1011.239)(s+48.908\pm j789.434)(s+45.602\pm j777.971)}$
P_{o13}	=	$\frac{3.60*10^{10}(s+45.827\pm j777.983)(s+15)}{(s+0.001)(s+15.402)(s+740.143\pm j197.691)(s+49.296\pm j787.205)(s+45.602\pm j777.971)}$
P_{o14}	=	$\frac{4.00*10^{10}(s+45.827\pm j777.981)(s+15)}{(s+0.001)(s+15.396)(s+739.745\pm j195.897)(s+49.698\pm j788.217)(s+45.602\pm j777.969)}$
P_{o15}	=	$\frac{3.28*10^{10}(s+45.827\pm j777.985)(s+15)}{(s+0.001)(s+15.491)(s+471.115)(s+1010.445)(s+48.615\pm j788.405)(s+45.602\pm j777.973)}$
P_{o16}	=	$\frac{3.60*10^{10}(s+47.923\pm j777.686)(s+15)}{(s+0.004)(s+15.274)(s+476.100)(s+1009.715)(s+48.686\pm j789.929)(s+45.607\pm j777.517)}$
P_{o17}	=	$\frac{3.60*10^{10}(s+47.924\pm j777.686)(s+15)}{(s+0.004)(s+15.235)(s+742.482\pm j201.752)(s+49.132\pm j787.946)(s+45.607\pm j777.517)}$
P_{o18}	=	$\frac{3.24*10^{10}(s+47.924\pm j777.686)(s+15)}{(s+0.004)(s+15.269)(s+603.175)(s+883.518)(s+48.250\pm j787.010)(s+45.607\pm j777.686)}$
P_{o19}	=	$\frac{4.00*10^{10}(s+47.925\pm j777.633)(s+15)}{(s+0.004)(s+15.228)(s+742.085\pm j200.004)(s+49.607\pm j788.906)(s+45.607\pm j777.464)}$
P_{o110}	=	$\frac{3.28*10^{10}(s+47.923\pm j777.729)(s+15)}{(s+0.003)(s+15.282)(s+477.483)(s+1008.910)(s+48.393\pm j788.944)(s+45.606\pm j777.560)}$

Table B.3 Full Set of Outer Loop Plants

P_{ol1}	$=$	$\frac{0.1208(s+15)}{s(s+15.428)}$
P_{ol2}	$=$	$\frac{0.1213(s+15)}{s(s+15.483)}$
P_{ol3}	$=$	$\frac{0.0987(s+15)}{s(s+15.402)}$
P_{ol4}	$=$	$\frac{0.1096(s+15)}{s(s+15.396)}$
P_{ol5}	$=$	$\frac{0.1103(s+15)}{s(s+15.491)}$
P_{ol6}	$=$	$\frac{0.1198(s+15)}{s(s+15.274)}$
P_{ol7}	$=$	$\frac{0.0977(s+15)}{s(s+15.235)}$
P_{ol8}	$=$	$\frac{0.0980(s+15)}{s(s+15.269)}$
P_{ol9}	$=$	$\frac{0.1086(s+15)}{s(s+15.228)}$
P_{ol10}	$=$	$\frac{0.1089(s+15)}{s(s+15.282)}$

Table B.4 Reduced Set of Outer Loop Plants

Appendix C. QFT CAD Batch Load Matlab M-File

C.1 Background

The QFT CAD package is a powerful design tool that simplifies the computations necessary in applying the QFT [11]. But the QFT CAD package does not provide an easy method for loading a large number of plants. For example, if the number of plant models and plant disturbance models in a given problem is N each, then either $2N$ transfer functions must be manually typed or $2N$ files must be individually loaded. This process takes time since some problems require several hundred plants. The chances for erroneous transfer function entry are also high.

The program *qftcad* is a Matlab M-file that loads the plant and disturbance models, for the Multiple Input and Single Output (MISO) configuration, as a batch process. The program is invoked from the Matlab command line as

$$qftcad(pnum, pden, dnum, dden, fname)$$

where the function argument *pnum* denotes the array of plant model numerator vectors, the function argument *pden* denotes the array of plant model denominator vectors, the function argument *dnum* denotes the array of outside disturbance model numerator vectors, and the function argument *dden* denotes the array of outside disturbance model denominator vectors. The function argument *fname* is the desired output file name.

The program produces a file, designated by the argument *fname*, which contains the '*plants =*' segment of the QFT CAD *qftsave.m* file. The file content is then pasted directly over the '*plants =*' segment of the *qftsave.m* file in the working directory. Since the process is automated, the chances of erroneous entry are eliminated.

The program *qftcad* invokes an another M-file program called *isreal*. This program checks to see if the given argument is a real or imaginary number.

C.2 Listing of the M-file qftcad

```
function flag = qftcad(pnum, pden, dnum, dden, fname)
% Set successful flag to false
    flag = 0;
    if (length(pden(:,1)) == length(dden(:, 1)))
% Set all numbers less than 1e-8 to zero
        for i = 1 : length(pnum(:,1))
            for j = 1 : length(pnum(1,:))
                if (pnum(i,j) < 1e-8)
                    pnum(i,j) = 0;
                end
            end
        end
        for i = 1 : length(pden(:,1))
            for j = 1 : length(pden(1,:))
                if (pden(i,j) < 1e-8)
                    pden(i,j) = 0;
                end
            end
        end
        for i = 1 : length(dnum(:,1))
            for j = 1 : length(dnum(1,:))
                if (dnum(i,j) < 1e-8)
                    dnum(i,j) = 0;
                end
            end
        end
        for i = 1 : length(dden(:,1))
            for j = 1 : length(dden(1,:))
                if (dden(i,j) < 1e-8)
                    dden(i,j) = 0;
                end
            end
        end
% Open File and Initialize
        fid = fopen(fname, 'w');
        fprintf(fid, 'plants = {');
        fclose(fid);
        fid = fopen(fname, 'a');
% Create plants segment of the QFT CAD file
        for index = 1 : length(pnum(:,1))
% The ',' is used to separate between the transfer functions. The '}' is used to close the file
            if (index == length(pnum(:,1)))
                endspec = '}';
            else
                endspec = ',';
            end
% determine system gain
            pnumgain = nonzeros(pnum(index, :));
            pdengain = nonzeros(pden(index, :));
            gain = pnumgain(1)/pdengain(1);
```

```

        fprintf(fid, '{}", {}, {{transferF[s, s, 0]}[%f,{' ,gain);
% Find system poles and zeros
    pnumroots = roots(pnum(index, :));
    pdenroots = roots(pden(index, :));
    if (length(pnumroots) > 0)
% Construct plant zeros
        for lencheck = 1 : length(pnumroots)
            if (lencheck == length(pnumroots))
                plantsep = ', {}, {';
            else
                plantsep = ',';
            end
            if (isreal(pnumroots(lencheck)))
                fprintf(fid, ' %f %s', pnumroots(lencheck), plantsep);
            else
                if (imag(pnumroots(lencheck)) < 0)
                    fprintf(fid, ' %f-%fI %s', real(pnumroots(lencheck)),
                        abs(imag(pnumroots(lencheck))), plantsep);
                else
                    fprintf(fid, ' %f+%fI %s', real(pnumroots(lencheck)),
                        abs(imag(pnumroots(lencheck))), plantsep);
                end
            end
        end
    else
        fprintf(fid, ', {}, {');
    end
% Construct plant poles
    for lencheck = 1 : length(pdenroots)
        if (lencheck == length(pdenroots))
            plantsep = ', {}]]},';
        else
            plantsep = ',';
        end
        if (isreal(pdenroots(lencheck)))
            fprintf(fid, ' %f %s', pdenroots(lencheck), plantsep);
        else
            if (imag(pdenroots(lencheck)) < 0)
                fprintf(fid, ' %f-%fI %s', real(pdenroots(lencheck)),
                    abs(imag(pdenroots(lencheck))), plantsep);
            else
                fprintf(fid, ' %f+%fI %s', real(pdenroots(lencheck)),
                    abs(imag(pdenroots(lencheck))), plantsep);
            end
        end
    end
% determine disturbance gain
    dnumgain = nonzeros(dnum(index, :));
    ddengain = nonzeros(dden(index, :));
    gain = dnumgain(1)/ddengain(1);
    fprintf(fid, '{{transferF[s, s, 0]}[%f,{' ,gain);

```

```

% Find disturbance poles and zeros
    dnumroots = roots(dnum(index, :));
    ddenroots = roots(dden(index, :));
    if (length(dnumroots) > 0)
% Construct disturbance plant zeros
        for lencheck = 1 : length(dnumroots)
            if (lencheck == length(dnumroots))
                plantsep = '}, {}, {';
            else
                plantsep = ',';
            end
            if (isreal(dnumroots(lencheck)))
                fprintf(fid, ' %f %s', dnumroots(lencheck), plantsep);
            else
                if (imag(dnumroots(lencheck)) < 0)
                    fprintf(fid, ' %f-%fI %s', real(dnumroots(lencheck)),
                        abs(imag(dnumroots(lencheck))), plantsep);
                else
                    fprintf(fid, ' %f+%fI %s', real(dnumroots(lencheck)),
                        abs(imag(dnumroots(lencheck))), plantsep);
                end
            end
        end
    end
    else
        fprintf(fid, '}, {}, {');
    end
% Construct disturbance poles
    for lencheck = 1 : (length(ddenroots) - 1)
        if (isreal(ddenroots(lencheck)))
            fprintf(fid, ' %f,', ddenroots(lencheck));
        else
            if (imag(ddenroots(lencheck)) < 0)
                fprintf(fid, ' %f-%fI,', real(ddenroots(lencheck)),
                    abs(imag(ddenroots(lencheck))));
            else
                fprintf(fid, ' %f+%fI,', real(ddenroots(lencheck)),
                    abs(imag(ddenroots(lencheck))));
            end
        end
    end
    lencheck = length(ddenroots);
% The last pole has a slight different syntax than the rest
    if (isreal(ddenroots(lencheck)))
        fprintf(fid, ' %f, {}]]]] %s \n', ddenroots(lencheck), endspec)
    else
        if (imag(ddenroots(lencheck)) < 0)
            fprintf(fid, ' %f-%fI, {}]]]] %s \n', real(ddenroots(lencheck)),
                abs(imag(ddenroots(lencheck))), endspec);
        else
            fprintf(fid, ' %f+%fI, {}]]]] %s \n', real(ddenroots(lencheck)),
                abs(imag(ddenroots(lencheck))), endspec);
        end
    end

```

REPORT DOCUMENTATION PAGE

Form Approved
OMB No. 0704-0188

Public reporting burden for this collection of information is estimated to average 1 hour per response, including the time for reviewing instructions, searching existing data sources, gathering and maintaining the data needed, and completing and reviewing the collection of information. Send comments regarding this burden estimate or any other aspect of this collection of information, including suggestions for reducing this burden, to Washington Headquarters Services, Directorate for Information Operations and Reports, 1215 Jefferson Davis Highway, Suite 1204, Arlington, VA 22202-4302, and to the Office of Management and Budget, Paperwork Reduction Project (0704-0188), Washington, DC 20503.

1. AGENCY USE ONLY (Leave blank)	2. REPORT DATE December 1994	3. REPORT TYPE AND DATES COVERED Master's Thesis	
4. TITLE AND SUBTITLE ELECTRO-HYDROSTATIC ACTUATOR CONTROLLER DESIGN USING QUANTITATIVE FEEDBACK THEORY		5. FUNDING NUMBERS	
6. AUTHOR(S) Ki Ho Kang		8. PERFORMING ORGANIZATION REPORT NUMBER AFIT/GE/ENG/94D-18	
7. PERFORMING ORGANIZATION NAME(S) AND ADDRESS(ES) Air Force Institute of Technology, WPAFB OH 45433-6583		10. SPONSORING / MONITORING AGENCY REPORT NUMBER	
9. SPONSORING / MONITORING AGENCY NAME(S) AND ADDRESS(ES) WL/FIGS Wright-Patterson AFB, OH 45433-7521		11. SUPPLEMENTARY NOTES	
12a. DISTRIBUTION / AVAILABILITY STATEMENT Distribution Unlimited		12b. DISTRIBUTION CODE	
13. ABSTRACT (Maximum 200 words) The Electro-Hydrostatic Actuator (EHA) technology offers a higher degree of combat survivability and easier maintainability of the aircraft flight control system, because all the components necessary to operate the actuator are collocated with the actuator. Quantitative Feedback Theory (QFT) is used to design a control system for the EHA. The impact of parameter variations, sensor noise, and flight conditions are explicitly considered in the design process. The solution utilizes a two loop QFT feedback structure. The inner loop structure stabilizes the motor's angular velocity and decreases the outer loop's uncertainty. The outer loop structure controls the RAM piston's position to track the input command. The resulting design is not only robust with respect to plant parameter variations, but is also insensitive to the effects of sensor noise. The actuator's phase lag is reduced by incorporating phase constraints in the QFT design paradigm. QFT is shown to be a viable tool in solving a real-world problem.			
14. SUBJECT TERMS Quantitative Feedback Theory, QFT, Electro-Hydrostatic Actuator, EHA Actuator, Robust Control, Sensor, Noise		15. NUMBER OF PAGES 110	16. PRICE CODE
17. SECURITY CLASSIFICATION OF REPORT UNCLASSIFIED	18. SECURITY CLASSIFICATION OF THIS PAGE UNCLASSIFIED	19. SECURITY CLASSIFICATION OF ABSTRACT UNCLASSIFIED	20. LIMITATION OF ABSTRACT UL

```
        end
    end
end
fclose(fid);
% Set the success completion flag
flag = 1;
end;
```

C.3 Listing of the M-file isreal

```
function examine = isreal(x)
    if (real(x) == x)
        examine = 1;
    else
        examine = 0;
    end
```

Bibliography

1. Blakelock, John H. *Automatic Control of Aircraft and Missiles*, New York: John Wiley & Sons, Inc., 1991.
2. de Silva, Clarence W. *Control Sensors and Actuators*, Englewood Cliffs: Prentice-Hall, Inc., 1989.
3. D'Azzo, John J. and Houpis, Constantine H. *Linear Control System Analysis and Design - Conventional and Modern*, New York: McGraw-Hill Inc., 1988.
4. Houpis, Constantine and Lamont, Gary *Digital Control Systems - Theory, Hardware, Software*, New York: McGraw-Hill, Inc., 1985.
5. Morse, Allen C. *Electrohydraulic Servomechanism*, New York: McGraw-Hill, Inc., 1963.
6. Nelson, Robert C. *Flight Stability and Automatic Control*, New York: McGraw-Hill, Inc., 1989.
7. Reynolds, Odell R. *Design of a Subsonic Envelope Flight Control System for the VISTA F-16 Using Quantitative Feedback Theory*, MS Degree Thesis, AFIT/GE/ENG/93D-34. School of Engineering, Air Force Institute of Technology (AU), Wright-Patterson AFB OH, December 1993.
8. Pachter, Meir, Class Notes, EENG640 - Automatic Flight Control I, Dec 93.
9. Pachter, Meir, Class Notes, EENG641 - Automatic Flight Control II, Mar 94.
10. Rubin, Orli *The Design of Automatic Control System*, Norwood: Artech House, Inc., 1986.
11. Sating, Richard R. *Development of an Analog MIMO QFT CAD Package*, MS Degree Thesis, AFIT/GE/ENG/92J-04. School of Engineering, Air Force Institute of Technology (AU), Wright-Patterson AFB OH, June 1992.
12. GE Aerospace: *Electrically Powered Actuation Design (EPAD) Preliminary Configuration Review*, Johnson City, 1991.
13. GE Aerospace: *Electrically Powered Actuation Design (EPAD) Critical Configuration Review*, Johnson City, 1992.
14. GE Aerospace: *Interface Control Sheets, Servo Cylinder, Stabilator/Canard*, Johnson City, 1987.
15. MPC Products Corps.: *Horizontal Stabilizer Trim and Flaperon for the F-16*, 1993.
16. WL/FIG: *Electrically Powered Actuation Design (EPAD) Statement of Work*, Wright Patterson AFB, 1991.

Vita

Captain Ki Ho Kang was born 3 January 1966 in Seoul, Korea. He immigrated to the States in 1978, becoming a naturalized U.S. citizen in 1985. He attended Rensselaer Polytechnic Institute with a Four Year Air Force Reserve Officer Training Corps (ROTC) scholarship. Upon graduation from Rensselaer with a degree in the electrical engineering program, he was commissioned as an Air Force officer in 1989.

At McClellan AFB, he served as an A-10/QF-100 systems engineer. He was then reassigned to the 337th Test Squadron, also at McClellan AFB, to become the Developmental Test and Evaluation (DT&E) test director for the A-10 Global Positioning System/Improved Data Modem integration program.

He then transferred to Wright-Patterson AFB to pursue a graduate degree from the Air Force Institute of Technology (AFIT) in Guidance and Control. He was assigned to the Air Force Technology Application Center (AFTAC) at Patrick AFB upon the completion of his Masters of Science in Electrical Engineering (MSEE) degree in December 1994.

Permanent address: 14560 Woodland Ridge Drive
Centreville, VA 22020